A Study of Growth and Doping of cubic Group III Nitride Structures

Dem Department Physik
der Universität Paderborn
zur Erlangung des akademischen Grades eines

Doktors der Naturwissenschaften

vorgelegte

Dissertation

von

Ulrich Köhler

Paderborn, April 2003

Abstract

Current commercially available advanced optoelectronic devices made from group III Nitrides are based on material exhibiting hexagonal crystal structure. Magnesium is in use as p–type dopant, and Silicon as donor element. Quantum structures make use of ternary and quaternary compositional alloys, $Al_xIn_yGa_{1-x-y}N$, where the Aluminum and Indium mole fractions x and y, respectively, allow a precise tailoring of the electronic and structural properties.

Group III Nitrides with cubic crystal symmetry are considered as alternatives because of potentially more favourable material properties. In the course of this thesis work, cubic III Nitrides have been examined in closer detail. Molecular Beam Epitaxy was used to grow GaN and AlN epitaxial films as well as $Al_xGa_{1-x}N$/GaN heterostructures and quantum structures. Furthermore, cubic Aluminum Nitride was grown both on c–GaN and directly on Gallium Arsenide substrates, thus demonstrating the possibility of direct AlN low temperature nucleation.

The first part of this thesis is concerned with the properties of Carbon as an alternative acceptor in cubic Gallium Nitride. To this purpose Carbon doping sources were constructed and calibrated. By means of temperature–dependent luminescence and Hall measurements the thermal activation energy of Carbon was determined as $E_A = 215meV$. Additionally, excitation–dependent photoluminescence revealed the existence of a Carbon–related deep center. The effect of the incorporation of Carbon in c–GaN was calculated. The experimental results were reproduced by assuming a self–compensation of the Carbon acceptor by a Carbon interstitial. This behaviour explains electrical and optical incorporation–dependent trends.

The second part deals with $Al_xGa_{1-x}N$ structures. Electrical measurements revealed p–type conductivity of as–grown samples. $Al_xGa_{1-x}N$/GaN multi quantum wells were grown and characterized optically and structurally. The energetic positions of the optical QW transitions as a function of well width and barrier Aluminum content were successfully modelled using effective mass theory.

Contents

Abstract ii

Table of Contents iii

List of Figures v

List of Tables vii

List of Symbols and Constants viii

1 An Introduction 1

2 Fundamentals 4
- 2.1 GaN, AlN and their Ternaries — A Materials Science View 4
- 2.2 Characterization Techniques 7
  - 2.2.1 Luminescence 7
  - 2.2.2 Electrical Measurements 13
  - 2.2.3 X–ray Diffraction 14
- 2.3 Molecular Beam Epitaxy 15
  - 2.3.1 Gallium Nitride Growth 17
  - 2.3.2 Gallium Nitride Nucleation 18

3 Carbon Doping of GaN **23**
- 3.1 General Considerations 24
- 3.2 Carbon Doping Source 26
- 3.3 Measurements and Results 32
  - 3.3.1 Structural Properties 32
  - 3.3.2 Photoluminescence 35
  - 3.3.3 Electrical Properties 41
- 3.4 Discussion 47

4 AlN and AlGaN based Structures **50**
- 4.1 Cubic AlN 50
  - 4.1.1 Growth of c–AlN 50
  - 4.1.2 Structural Properties of c–AlN 51
  - 4.1.3 Further Characterization 51

4.2 GaN/AlGaN Quantum Structures 52
4.2.1 Modelling Quantum Structures 54
4.2.2 Structural Properties 57
4.2.3 Luminescence 63
4.3 Discussion 69

5 Conclusions **72**

Bibliography **75**

Appendix **86**

A Listing of samples **86**

List of Figures

2.1 Variation of AlGaN gap energy with Aluminum content 6
2.2 Schematic of the Photoluminescence setup 9
2.3 Schematic of the PL apparatus additon 10
2.4 Typical GaN reflection spectrum 11
2.5 Schematic of the Cathodoluminescence setup 12
2.6 Electron beam penetration depths over acceleration voltage 13
2.7 Schematic of the materials research diffractometer 15
2.8 Schematic of an MBE system 16
2.9 Quadrupole mass spectrum over 0–200amu. 17
2.10 Detail of a Quadrupole mass spectrum. 18
2.11 (002) rocking curve widths *vs.* Ga flux and time 19
2.12 (002) rocking curve widths of nucleation processes 20
2.13 PL exciton linewidths for different nucleation processes 21
2.14 Substrate coverage during nucleation 22

3.1 Comparison of acceptor energy trends in III–V semiconductors 25
3.2 Graphite vapour pressure and atom flux 26
3.3 Head of the e^-–*flux* cell 27
3.4 Detailed view of e^-–*flux* cell filament 28
3.5 Total of e^-–*flux* cell 29
3.6 Filament cell before assembly 30
3.7 Filament graphite cell 31
3.8 Carbon flux calibration curve. 32
3.9 Quadrupole Carbon measurements 33
3.10 X–ray scans of a c–GaN:C sample 34
3.11 AFM scans of c–GaN:C samples 35
3.12 PL spectra of c–GaN samples with different Carbon doping 36
3.13 Variation of Carbon–related PL with C flux 37
3.14 Ratio of C–related to near–edge intensity 38
3.15 Photoluminescence spectra taken at different temperatures 39
3.16 Temperature shift of near band edge Photoluminescence 40
3.17 PL intensity of c–GaN:C as function of excitation intensity 41
3.18 Hall data as a function of Carbon incorporation 42
3.19 Self–compensation model and comparison to Hall data 45
3.20 Temperature–dependent Hall data 46
3.21 Carbon incorporation model verified by hole concentration and PL . . . 48

4.1 RHEED image of an AlN sample 51
4.2 (113) reciprocal space map of cubic AlN on c–GaN 52
4.3 GaN/$Al_xGa_{1-x}N$ MQW sample layout 53
4.4 RHEED image of GaN/$Al_xGa_{1-x}N$ MQW sample after growth stop . . 54
4.5 Transmission spectrum of a c–$Al_xGa_{1-x}N$ structure on c-GaN 55
4.6 Critical thickness of cubic $Al_xGa_{1-x}N$ layers on c-GaN 56
4.7 Schematic of the energetics of a GaN/$Al_xGa_{1-x}N$ quantum well 57
4.8 RSM of the (113) reflex of a GaN/$Al_{0.08}Ga_{0.92}N$ MQW sample 58
4.9 RSM of a GaN/AlGaN MQW sample showing no strain 59
4.10 $\omega - 2\theta$ scan of (002) GaN/$Al_{0.24}Ga_{0.76}N$ MQW reflex 60
4.11 TEM image of fivefold GaN quantum well 61
4.12 TEM image of GaN MQWs with atomic resolution 62
4.13 TEM image of GaN multi quantum well 63
4.14 Fluctuation of QW and barrier thickness 64
4.15 Variation of QW and barrier thickness in growth direction 65
4.16 AFM images of MQW sample 66
4.17 Depth–resolved RT CL spectra of 2.5/5nm MQW sample 67
4.18 Ratio of quantum well to $Al_{0.24}Ga_{0.76}N$ bulk luminescence intensity . . 68
4.19 CL spectra of 5x and 20x GaN/$Al_xGa_{1-x}N$ MQW samples 69
4.20 Variation of QW luminescence energy with well width and barrier height 70
4.21 Comparison of QW model with CL peak energies 71

List of Tables

2.1 Summary of published data, calculated for cubic GaN. 5
2.2 Summary of published data, calculated for cubic AlN. 5

3.1 Data of the Carbon acceptor in c–GaN from optical measurements . . . 38
3.2 Electrical data of the Carbon acceptor in c–GaN 46

4.1 Published experimental values of a_0 and E_g for c–AlN 50
4.2 Summary of electrical data for cubic AlN. 51
4.3 Summary of TEM data for 5nm/10nm GaN/$Al_{0.24}Ga_{0.76}N$ MQW structure 62
4.4 CL intensity of GaN/$Al_xGa_{1-x}N$ MQW samples 67

A.1 Sample listing no. 1. 87
A.2 Sample listing no. 2. 88
A.3 Sample listing no. 3. 89
A.4 Sample listing no. 4. 90
A.5 Sample listing no. 5. 91

List of abbrevations

AFM	*Atomic Force Microscope/Microscopy*
BEP	*Beam Equivalent Pressure*
CL	*Cathodoluminescence*
cw	*Continuous Wave*
DFT	*Density Functional Theory*
DOS	*Density of States*
EDX	*Energy Dispersive X–Ray Analysis*
EL	*Electroluminescence*
ELOG	*Epitaxial Lateral Overgrowth*
FWHM	*Full Width at Half Maximum*
HRXRD	*High–Resolution X–Ray Diffraction*
HVPE	*Halide Vapour Phase Epitaxy*
IR	*Infrared*
LD	*Laser Diode*
LDA	*Linear Density Approximation*
LED	*Light Emitting Diode*
LT	*Low Temperature*
MBE	*Molecular Beam Epitaxy*
MOCVD	*Metal–Organic Chemical Vapour Deposition*
MOVPE	*Metal–Organic Vapour Phase Epitaxy*
MQW	*Multi Quantum Well*
PBN	*Pyrolytic Boron Nitride*
PG	*Pyrolytic Graphite*
PL	*Photoluminescence*
PMT	*Photomultiplier Tube*
QMS	*Quadrupole Mass Spectrometer*
QW	*Quantum Well*
rf	*Radio Frequency*
RHEED	*Reflection High Energy Electron Diffraction*
RSM	*Reciprocal Space Map*
RT	*Room Temperature*
SEM	*Scanning Electron Microscope/Microscopy*
SIMS	*Secondary Ion Mass Spectometry*
SL	*Superlattice*
STM	*Scanning Tunneling Microscope/Microscopy*
TEM	*Transmission Electron Microscope/Microscopy*
UHV	*Ultra–High Vacuum*
UV	*Ultraviolet*
VT	*Variable Temperature*
XRD	*X–Ray Diffraction*

List of symbols

a, b	deformation potentials	(eV)
a_0	lattice constant	(Å)
A	area, aperture	(cm^2)
A	atomic weight	(g $mole^{-1}$)
C_{ij}	elastic stiffness tensor	(GPa)
ε	dielectric permittivity	
ϵ_{ij}	stress tensor	
E	energy	(Nm=J)
E_g	band gap energy	(eV)
E_{beam}	electron beam energy	(eV)
E_A	acceptor energy	(eV)
E_D	donor energy	(eV)
E_f	formation energy	(eV)
E_F	Fermi energy	(eV)
f	lattice misfit	
f_i	Phillips ionicity scale	
F_C	Carbon atom flux	(atoms $(cms)^{-1}$)
F_{Ga}	Gallium atom flux	(atoms $(cms)^{-1}$)
h_c	critical film thickness	(nm)
I	Intensity	
L_z	quantum well width	Å
μ	mobility	(cm^2 $(Vs)^{-1}$)
m_e^*	electron effective mass	(kg)
m_h^*	hole effective mass	(kg)
M_{mol}	molar mass	(kg/mole)
n	electron concentration	(cm^{-3})
N_A	acceptor concentration	(cm^{-3})
N_C	conduction band density of states	(cm^{-3})
N_C^{GaAs}	Carbon atom concentration in GaAs host crystal	(cm^{-3})
N_C^{GaN}	Carbon atom concentration in GaN host crystal	(cm^{-3})
N_D	donor concentration	(cm^{-3})
N_{Ga}^{GaAs}	Gallium atom concentration in GaAs host crystal	(cm^{-3})
N_{Ga}^{GaN}	Gallium atom concentration in GaN host crystal	(cm^{-3})
N_V	valence band density of states	(cm^{-3})
ρ	density	(g cm^{-3})
p	hole concentration	(cm^{-3})
R_e	electron penetration depth	(nm)
R_H	Hall constant	(cm^3 $(As)^{-1}$)
R_g	growth rate	
S	entropy	(eV/K)
σ	strain tensor	

T	temperature	(K)
Z	atomic number	

List of constants

a_0^{AlN}	4.38Å	c–AlN lattice constant
a_0^{GaAs}	5.6533Å	GaAs lattice constant
a_0^{GaN}	4.52Å	c–GaN lattice constant
a_0^{MgO}	4.21Å	MgO lattice constant
a_0^{3C-SiC}	4.36Å	3C–SiC lattice constant
a_B	0.52918Å	Bohr radius
amu	$8.8542 \cdot 10^{-27}$kg	atomic mass unit
ε_0	$8.8542 \cdot 10^{-12}$As/(Vm)	dielectric permittivity in vacuum
e	$1.6022 \cdot 10^{-19}$C	elementary charge
e	2.718282	
E_{Ry}	13.6eV	Rydberg energy
h	$6.6262 \cdot 10^{-34}$Js	Planck's constant
$\hbar$	$1.055 \cdot 10^{-34}$Js	Planck's constant divided by 2π
k_B	$1.3807 \cdot 10^{-23}$J/K	
	$8.617 \cdot 10^{-5}$eV/K	Boltzmann's constant
m_e	$9.1092 \cdot 10^{-31}$kg	free electron rest mass
N_{Avo}	$6.022 \cdot 10^{23}$mole^{-1}	Avogadro's number

Chapter 1

An Introduction

or,
Physicists and the Quest for the Holy Grail

Ever since the inception of light emitting semiconductor devices, the replacement of the everyday incandescent bulb lamp has been something akin to the Holy Grail of semiconductor physics. The incandescent lamp of old basically dates its design, which is still visible in the vacuum glass bulb, back to the days of Thomas A. Edison. Although the concept has been much improved, the principal weaknesses remain: glass shatters easily, the filament is made of brittle materials, so that the overall susceptibility to shock is relatively high. Furthermore the radiation is produced thermally (as black body radiation of the filament), so that the vast majority of the radiative energy, approximately 95–98% for ordinary bulb lamps, is emitted in the infrared spectral region which is in most cases unwanted and thus the cause of a rather low efficiency.

Solid state lighting technology however appears to be the perfect replacement: it offers a rugged, simple design without any brittle parts. Moreover, the departure from light generation by means of thermal radiation means that light emission covers only a small fraction of the spectrum. This can of course be turned into an advantage, as it leads to an increase in efficiency, but is also a disadvantage, for example with respect to the generation of white light which inherently covers a greater spectral range.

For a long time however solid state visible lighting has been limited to red, amber and green LEDs (and IR/red laser diodes). Although the Pankove group reported a Gallium Nitride based blue LED thirty years ago this achievement was still hampered by a extremely low efficiency due to the lack of an adequate p–type dopant [1]. Therefore this diode was rather designed as i–n junction.

Only the last decade witnessed an extraordinary increase in Gallium Nitride related research activity culminating in commercially available room temperature *cw* laser diodes [2]. This research activity concerned not only Gallium Nitride, but also the related compound semiconductors Indium Nitride and Aluminum Nitride plus their ternary and even quarternary compounds, eventually covering the spectral range of

2eV—6eV, i.e. the whole visible spectrum and an appreciably large portion of the UV. The emission of UV light enables the use of color conversion using phosphors very similar to the light generation in fluorescence lamps.
The application of III Nitride semiconductors does not stop at light–emitting devices; they are for example equally well–suited as photodetectors or amplifiers with high current densities and large breakdown voltages. This is especially interesting in the case of solar–blind $Al_xGa_{1-x}N$ sensors. The possible future use of the III Nitrides is even more attractive given the mechanical hardness and chemical inertness that make those semiconductor devices seem ideal candidates for devices operating at high temperatures or under otherwise harsh and adverse conditions [3, 4]. Their large piezoelectric coefficients suggest their use as actuators. As opposed to Silicon Carbide, which offers similar properties, Gallium–based Nitrides possess a direct band gap, thus increasing the optical efficiency. In summary, III Nitrides offer all the capacities of being truly optoelectronic materials.

The group III Nitrides are known to have two crystal phases under ambient conditions, wurtzite and cubic. The latter however is found to be the metastable phase, which is the reason why most of the scientific and commercial effort has been devoted to and consequently most progress has been reported for hexagonal phase material. Because of the higher crystal symmetry, cubic III Nitrides are expected to exhibit superior properties, such as smaller carrier scattering coefficients, lower dopant activation energies, and a smaller band gap [5]. Cubic phase III Nitrides can be grown on readily available Gallium Arsenide substrates (or even 3C–SiC). Those substrates can be doped, thus facilitating the electric device layout without the need for mesa etching or similarly difficult technological steps. Furthermore both substrate and epilayer possess the same crystal orientation and can therefore be cleaved easily, opening up a way for the manufacture of edge–emitting lasers without post–processing the laser facets.

For optoelectronic devices, controlled p–type doping is essential. The use of Magnesium, although widely applied, presents several drawbacks: the room temperature hole concentration usually reported lies in the middle $10^{17}cm^{-3}$. In MOCVD growth, Mg forms a complex with hydrogen, necessitating an extra thermal treatment. In MBE growth, Magnesium is extremely volatile, causing memory effects in the system. Moreover, it substitutes Gallium, so that the growth process procedes under Nitrogen-rich conditions, which are disadvantageous for the growth of high–quality epilayers. Carbon however, as will be shown in this work, is an acceptor when substituting Nitrogen and therefore readily incorporated under favourable Gallium-rich growth conditions. It does not cause any unwanted side effects in the MBE growth, and possesses a lower activation energy [6].

Advanced semiconductor devices make use of $Al_xGa_{1-x}N$ layers or quantum well structures, which may serve several purposes.
Firstly, layered structures of the $Al_xGa_{1-x}N/Al_yGa_{1-y}N$ type can act classically as (multi) QW structures or superlattices [2]. In this way, the layers are the optoelectronic active structures, either for generating or detecting light. The large band gap even makes it possbile to build sensor devices which are insensitive to ambient light, as mentioned above. Secondly, because of their different indices of refraction, $Al_xGa_{1-x}N/$ $Al_yGa_{1-y}N$ heterostructures may be used as light guiding elements of optoelectronic

devices, e.g. as Bragg reflectors that may be grown *in situ* [7, 8]. Thirdly, it has been shown that the variation of the chemical environment because of partial Gallium and Aluminum sublattices — evident in the varying position of valence and conduction band — increases the doping efficiency [9]. Lastly, in analogy to the case of GaAs–based devices, it might be possible to reduce the defect density by means of stacking several (dozen) $Al_xGa_{1-x}N/Al_yGa_{1-y}N$ layers [10].

Cubic QW structures grown in [100]direction do not exhibit spontaneous and piezo-electric polarization which result in a strong quantum–confined Stark effect, which in turn deteriorates QW efficiency severely because of the spatial separation of the hole and electron wave functions [11, 12].

This thesis is organized as follows:
Chapter 2 gives a general overview of the known material properties of c–GaN and c–AlN, along with a short discussion. It also contains a description of the principal experimental methods used in the course of this work, i.e., MBE setup and characterization by means of Photoluminescence and Cathodoluminescence as well as X–ray diffraction. Additionally the growth process itself and the influence and optimization of the nucleation are discussed.
Aspects of doping cubic Gallium Nitride using Carbon are delt with in chapter 3. This covers the commissioning and characterization of the Carbon sources and the optical and electrical characterization of the GaN:C films. The results are discussed using a model of Carbon incorporation onto N lattice sites, interstitials and Dicarbon complexes.
Cubic Aluminum Nitride films and $GaN/Al_xGa_{1-x}N$ multi quantum well structures are treated in chapter 4. The structural properties are revealed through X–ray and TEM measurements. GaN quantized states are modelled in effective mass theory, showing good agreement with the experimental values from CL measurements.
The results are summarized in chapter 5.

The nomenclature which has been used throughout this thesis is explained on the preceding pages viii through xi. This comprises abbrevations, usually in capital letters, on pages viii and following, symbols listed on pages ix f., and physical constants found on page xi. Therefore, in any case of uncertainty the reader is kindly referred to this chapter.

Chapter 2

Fundamentals

The successful demonstration of GaN devices — and their subsequent commercialization — have of course found their due reflection in a vast number of publications. To name but a few, references [2, 4, 7, 13] represent monographs and review articles on that subject matter.

2.1 GaN, AlN and their Ternaries — A Materials Science View

While the theoretical modelling of the most important physical properties seems rather straightforward from an experimentalist's point of view — while supplying reliable experimental data to the theoretical physicist in turn appears as an equally easy task —, a short survey of the available literature paints a quite different picture.

From the beginning, almost as much effort has been put devoted to the theoretical modelling of the III–Nitrides as to the experimental determination of their physical properties. Min *et al.* [14] and Yeh *et al.* [15] reported calulations of Gallium Nitride properties. The former concluded that the band gap was direct at $E_g = 3.0eV$, while the cohesive energy per unit cell was determined as $E = 0.6 \cdot E_{Ry} = 8.16eV$ per unit cell, with a difference of only $20meV$ between the cubic and wurtzite phases. Yeh *et al.* find a similar energetic difference between both phases of $18.4meV/atom$ and $9.9meV/atom$ for AlN and GaN, respectively, favouring the hexagonal phase. Hexagonal phase would be the stable modification at ambient conditions according to Muñoz *et al.* with a direct band gap of $E_g = 3.5eV$ [16]. Tables 2.1 and 2.2 offer a quick glance at several calculated values that are to be found in the literature for cubic III Nitrides.

Most references agree in estimating the Gallium–Nitride bond energy to be around $E_{cohesive} \approx 10eV$, thus exceeding for example the Gallium Arsenide value by a factor of 1.5 [28]. This may in part explain the extreme mechanical hardness and chemical inertness observed with group III–Nitrides, as compared e.g. to other III–V compound semiconductors. However, this may also be connected to the relatively high ionicity of the III–Nitrides. As has already been reported by Phillips and Van Vechten [29, 30, 31], AlN and GaN can be described as having an ionicity of $f_i = 0.449$ and $f_i = 0.5$, respectively, compared to the GaAs value $f_i = 0.31$. This is mainly due to the influence

E_g (eV)	2.77	2.23			3.1		1.28		3.8		
a_0 (Å)	4.48	4.46	4.46	4.46			4.59		4.56		4.36
$E_{cohesive}$ (eV)	5.02	6.8		10.8			8.25				
E_{W-ZB} (meV)							11.6				9.88
E_{phonon} (cm^{-1})			580			558					
a (eV)		-7.4	-6.4			-1.62					
C_{11} (GPa)			282	296		285		399		293	
C_{12} (GPa)			159	154		161		173		159	
C_{44} (GPa)			142	206		149		161		155	
B (GPa)	199	184		201		202	190	249			
ϵ		4.78			5.2						
references	[17]	[18]	[19]	[20]	[21]	[22]	[23]	[24]	[26]	[27]	[15]

Table 2.1: Summary of published data, calculated for cubic GaN.

E_g (eV)	4.52	3.39		4.9		4.13		5.2		
a_0 (Å)	4.35	4.37	4.32	4.35		4.394		4.36		4.36
$E_{cohesive}$ (eV)	6.4	11.15				11.36				
E_{W-ZB} (meV)						41.6				18.4
E_{phonon} (cm^{-1})			680		680					
a (eV)		-9.0	-0.38		-1.44					
C_{11} (GPa)			298		313		429.9		304	
C_{12} (GPa)			164		168		187.1		160	
C_{44} (GPa)			187		192		173.1		193	
B (GPa)	209	215			216	191	268.1			
ϵ		3.9		4.84						
references	[17]	[18]	[19]	[21]	[22]	[23]	[24]	[26]	[27]	[15]

Table 2.2: Summary of published data, calculated for cubic AlN.

of the Nitrogen atoms [32]. Furthermore, this high ionicity seems to be the cause (or rather the symptom?) of the most obvious structural difference between III–Nitrides and other III–V compounds: the equilibrium phase is a hexagonal crystal lattice, not a cubic one. Moreover, for high pressures the equilibrium phase is predicted to change to rock salt [33, 34, 35].
Nonetheless, the energetic difference between the cubic and hexagonal modifications of GaN and AlN is generally estimated to be small compared to the total bond energy (less than a half percent according to Stampfl *et al.* [23], not discernible in the figures of references [33, 34, 35]).

Considering the fact that the gap energies listed above in tables 2.1 and 2.2 vary rather widely and sometimes do not seem to bear any resemblance to actually measured data — Stampfl *et al.* even calculate the room temperature Indium Nitride gap $E_g < 0$ [23] — it appears at least debatable to what degree the other materials data should be trusted. Unfortunately, this variation seems to be rather a fundamental problem of the

chosen calculus — a density functional method, using linear density approximation, which solely considers effective one–particle eigenvalues. DFT band gaps are known to underestimate e.g. optically determined values by as much as 30–100%. Understandably, the accuracy of those numerical calculation schemes is critically dependent on the precise boundary conditions chosen for each individual case.
Rubio *et al.* [21, 25] rely instead on the quasiparticle approach outlined in Hedin [36] and Hybertsen *et al.* [37, 38]. The quasiparticle approach carried out in he so–called *GW approximation* expands the electron self–energy operator in a Green's function G and a dynamical screened interaction W. Since W uses the static dielectric matrix ϵ as input, the GW approach utilizes LDA results only as start parameters. Of course, such calculations are much more demanding with respect to computational efforts. Bechstedt *et al.* demonstrated the successful application of this approach to III–Nitrides [39].

Throughout this discussion similarities have been emphasized. However, as different authors point out, cubic Aluminum Nitride exhibits an indirect band gap [17, 21]. It is noted that in cubic GaN the lowest transition occurs from the Γ_{15}^{V} band to the Γ_{1}^{C} band, whereas in c–AlN the X_{1}^{C} band is lower than the Γ_{1}^{C} band. The variation of both direct and indirect transitions is shown in figure 2.1 where the respective bands involved were assumed to change their position linearly with Aluminum content x [17].

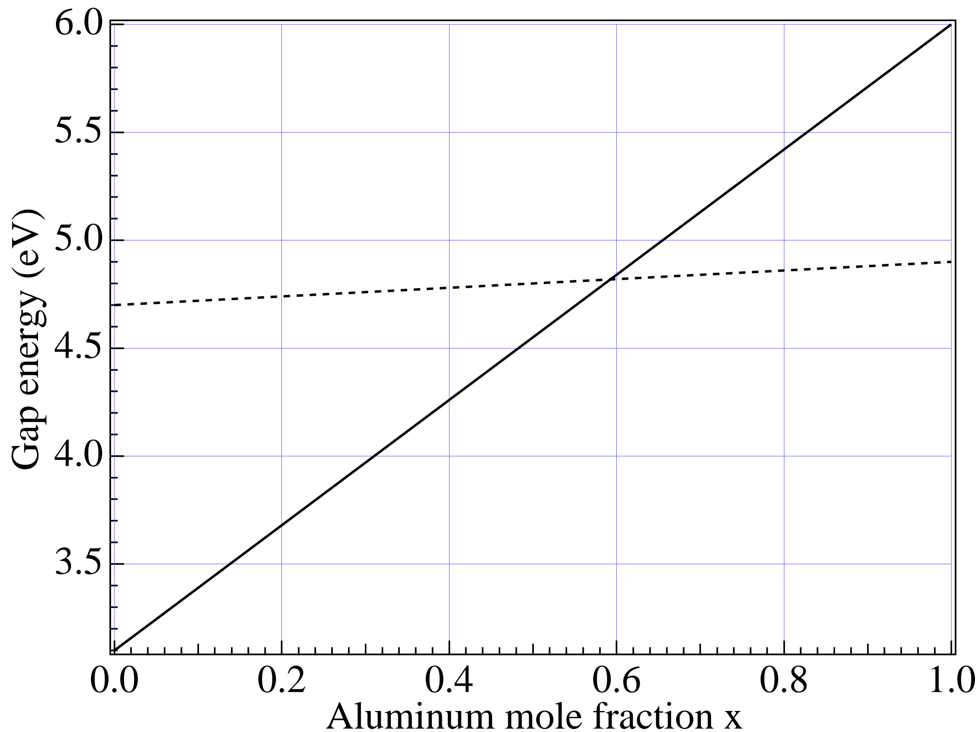

Figure 2.1: Linear variation of transitions $\mathbf{\Gamma_{15}^{V}}$– $\mathbf{\Gamma_{1}^{C}}$ (through line) and $\mathbf{\Gamma_{15}^{V}}$– $\mathbf{X_{1}^{C}}$ (dashed line), as discussed in the text.

Obviously the Γ_1^C band changes from c–GaN to c–AlN in agreement with observations made for hexagonal phase material. The difference lies in the behaviour of the X_1^C band which in the cubic structure is composed of an s–like state at the anion site and a p–like state at the cation. Both are relatively insensitive to changes at the cation site, so the band stays roughly at the same energy [25]. The resulting crossover from direct to indirect gap would occur at $x = 0.53$, which is in excellent agreement with references [17, 40].

2.2 Characterization Techniques

2.2.1 Luminescence

Generally speaking, luminescence refers to the emission of visible radiation. In the present context, this will also include near–UV and near–IR light. Luminescence is caused by the radiative recombination of excess carriers. Customarily, different types of luminescence are distinguished with respect to the kind of carrier excitation used:

- *Photoluminescence* — excitation of carriers by means of light irradiation
- *Cathodoluminescence* — cathode rays (i.e., electrons) as source of carrier excitation
- *Electroluminescence* — carrier injection through an externally applied electric field

All luminescence techniques mentioned above readily yield information about optical properties of the respective sample, however also, although somewhat more intrinsicately, structural information as well. A detailed treatment of luminescence spectroscopy can be found elsewhere [41, 42, 43].
In semiconductors of high purity, i.e., *intrinsic* semiconductors, *band to band transitions* (e, h) and *free exciton transitions* (X) are typically observed. Excitons are formed through Coulomb interaction between an electron and a hole and can be described with a hydrogenic model. Indeed, in high–quality semiconductors, several excited states can be observed experimentally. The intensity and width of the exciton luminescence transition allow a quick estimate of the relative sample quality. The Coulomb interaction lowers the exciton energy by the exciton binding energy E_X:

$$E = E_g - E_X. \tag{2.1}$$

The exciton binding energy can be calculated based on the effective mass theory:

$$E_X = \frac{E_{Ry}}{\epsilon^2} \cdot \left(\frac{1}{m_e^*} + \frac{1}{m_h^*} \right)^{-1}, \tag{2.2}$$

where the effective masses of the electron and hole are defined by the band dispersion:

$$m_e^* = \hbar^2 \cdot \left(\frac{d^2 E}{dk^2} \right)^{-1}. \tag{2.3}$$

In the case of defects, the excitons can further lower their energy by means of localizing to a (neutral or ionized) donor (acceptor):

$$E = E_g - E_X - E_{B,X}. \tag{2.4}$$

It was empirically found that the localization energy $E_{B,X}$ roughly equals 1/10 of the activation energy of the involved defect (Hayne's rule [44, 45]).
The introduction of impurities in a semiconductor causes the formation of related impurity levels, separated from the valence band (conduction band) by the acceptor (donor) binding energy E_A (E_D). Likewise, the acceptor binding energy can be calculated in a similar way to relation (2.2):

$$E_A = \frac{E_{Ry}}{\epsilon^2} \cdot m_h^*. \tag{2.5}$$

Given these considerations, the band to band transition transforms in the most general case into the *donor–acceptor pair transition* (D^0, A^0), and the luminescence transition energy

$$E = E_g - (E_A + E_D) + \frac{1}{2} \cdot k_B \cdot T. \tag{2.6}$$

The superscript 0 stands for neutral impurities, and the factor $\frac{1}{2} \cdot k_B \cdot T$ results from the thermal distribution of free carriers in the respective bands. At higher temperatures such that $E_A \approx k_B \cdot T$ not only the impurity band but also the valence/conduction bands are populated, causing *free to bound transitions* (D^0, h) or (e, A^0) to occur.
Furthermore the energetic position of the radiative transitions can be influenced by interactions with the crystal lattice. Of course this is most important for indirect semiconductors that require momentum transfer for radiative transitions, which is of lesser interest in the case of the direct semiconductor Gallium Nitride. By means of energy emission phonons are created and a ladder of additional spectral lines can be observed, the so–called phonon replica. Their intensity decreases with increasing energy difference from the original transition (*zero phonon line*) because of the decrease in energy transfer rate. The phonon replicas are evenly spaced at $E_{phonon} = \hbar \cdot \omega_{phonon}$, so that the nth phonon line is characterized by the energy

$$E(n) = E_{zpl} - n \cdot E_{phonon}. \tag{2.7}$$

In cubic GaN the phonon energies have been determined as [46]

$E_{LO} = 92meV$	longitudinal optical phonon
$E_{TO} = 69meV$	transverse optical phonon

Photoluminescence System

The setup used for PL measurements is shown schematically in figure 2.2. The luminescence was excited by means of a *Kimmons cw* HeCd laser. The $\lambda = 325nm \equiv 3.815eV$ line was singled from laser plasma lines with a Fabry–Perot interference filter. The output power, measured after the filter, totalled $\approx 3mW$. The laser light was focussed onto a spot of approximately 150μm diameter, yielding a power density of about $2.5Wcm^{-2}$.

The excitation intensity could be varied over four orders of magnitude using appropriate UV density filters. The luminescent light was collected with an exit lens and dispersed in a Spex 270M monochromator with a 1200 lines grating and 27cm focal length. The detection system consisted of a photomultiplier tube and a photon counting system (*Hamamatsu* C3866 Photon Counting Unit and *Hewlett–Packard* HP 53132A Universal Counter), controlled through a Macintosh–based LabVIEW program. The spectral resolution of this system was $\Delta\lambda = 0.2nm \equiv \Delta E = 1.5meV$ at $\lambda = 400nm \equiv 3.1eV$.

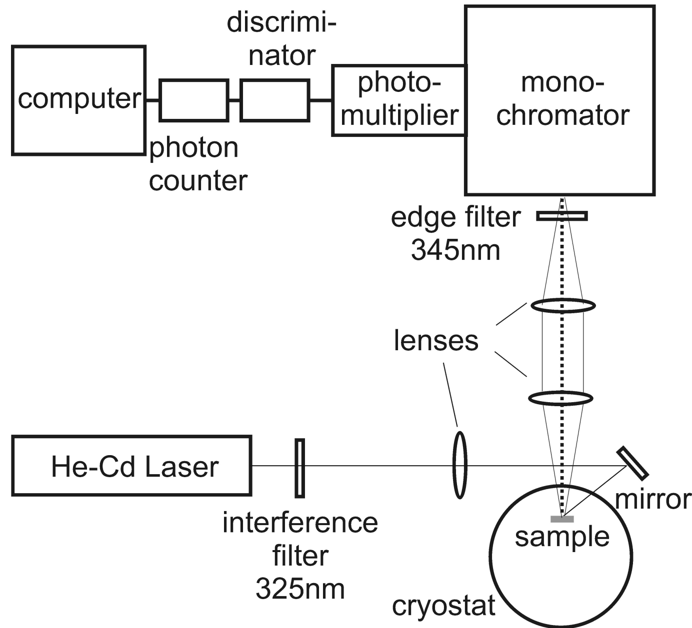

Figure 2.2: Schematic of the Photoluminescence setup.

The samples were mounted in a home–built liquid Helium bath–flow cryostat that allowed measurements at sample temperatures between $T = 2K$ and $T = 300K$ [47]. A *LakeShore* 330 Autotuning Temperature Controller in conjunction with a AlGaAs temperature diode and a heating transistor were used to adjust the sample temperature during measurements.

Reflection and Transmission Measurements

In the course of this work, the aforementioned PL system was extended such that samples could easily be measured in transmission as well as in reflection, without infringing on the PL setup. Figure 2.3 depicts the additions:

The white light of a Halogen lamp was coupled into the optical path between the cryostat and the monochromator by means of an Aluminum high–reflection mirror. In this operational mode, either transmission measurements or calibration runs could be conducted through a specially constructed sample holder inserted between the monochromator and the PMT. Furthermore, the white light could first be directed to the sample under almost normal incidence (2 to 3 degrees off), and the reflected light

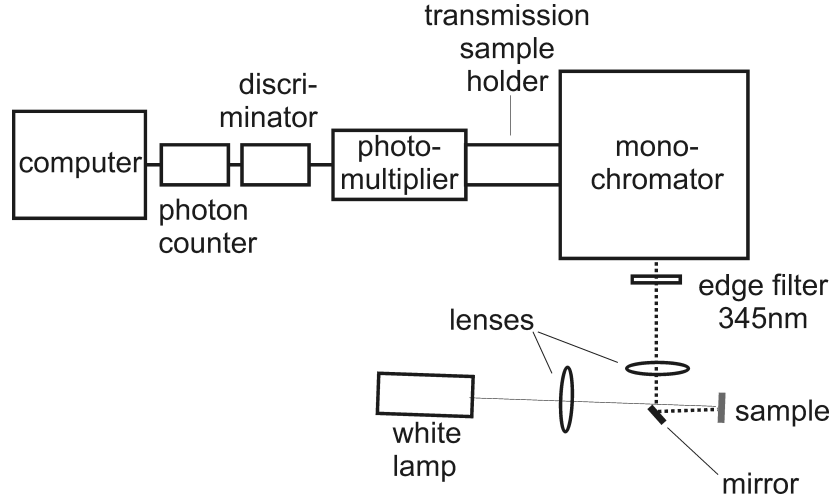

Figure 2.3: Schematic of the Photoluminescence extension for transmission and reflection measurements.

would be coupled into the optical path. Reverting to normal photoluminescence mode merely involved the removal of the coupling mirror.

In this extension setup, regardless of using either transmission or reflection mode the measured intensity is given by

$$I(\lambda) = I_0(\lambda) \cdot IRF(\lambda) \cdot R_{sample}(\lambda), \tag{2.8}$$

where I is the measured spectrum, $I_0 \cdot IRF$ describes the Halogen lamp spectral distribution as changed by the total instrument response function, and R_{sample} is the actual sample response. Clearly, R_{sample} is the quantity of interest, to be calculated as

$$R_{sample}(\lambda) = \frac{I(\lambda)}{I_0(\lambda) \cdot IRF(\lambda)}. \tag{2.9}$$

For two neighbouring interference extremal points λ_1, λ_2 given by $R_{sample}(\lambda)$ (see equation (2.9)) it is possible to calculate the layer thickness for a system air–layer–substrate, where the refractive indices increase in this order, via

$$d = \frac{\lambda_1 \cdot \lambda_2}{2 \cdot \left(\lambda_2 \cdot \sqrt{n_1^2 - sin^2\alpha} - \lambda_1 \cdot \sqrt{n_2^2 - sin^2\alpha}\right)}, \tag{2.10}$$

where n_1, n_2 are the layer indices of refraction at wavelengths λ_1, λ_2 at an angle of incidence α [48, 49]. Of course, for vanishing α this expression reduces to

$$d = \frac{1}{2 \cdot \left(\frac{n_1}{\lambda_1} - \frac{n_2}{\lambda_2}\right)}. \tag{2.11}$$

The refractive indices of cubic Gallium Nitride and InGaN were reported in the literature [50, 51, 52]. Diagram 2.4 shows on the left a typical reflection spectrum $I(\lambda)$ (circles), together with the product of Halogen lamp intensity and instrument response function, $I_0(\lambda) \cdot IRF(\lambda)$. The right ordinate depicts the normalized GaN sample reflectivity.

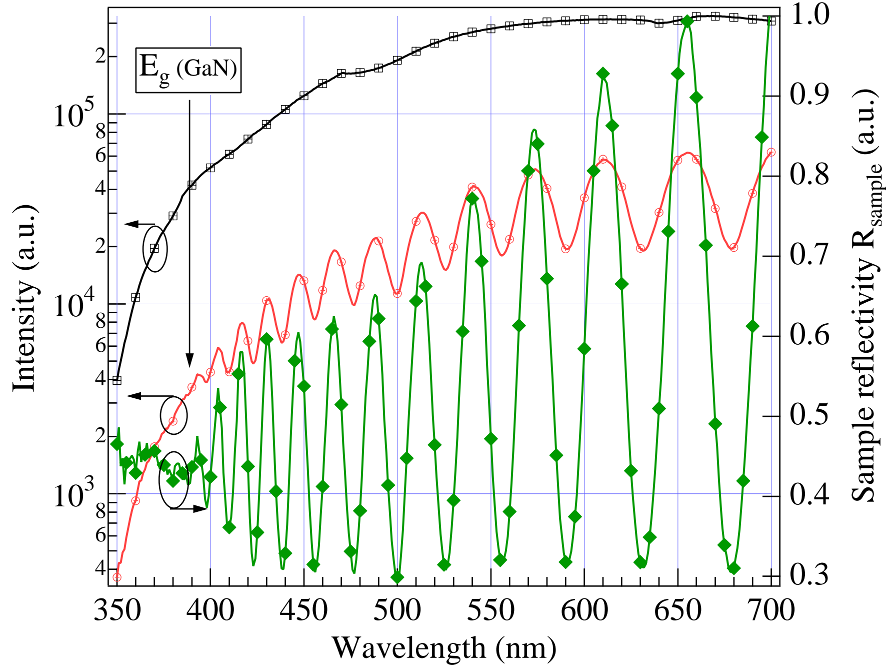

Figure 2.4: Typical GaN reflection spectrum. The left ordinate depicts as squares the instrument response and — shown as circles — the intensity reflected off the GaN sample. The right ordinate shows the resulting sample reflectivity.

Cathodoluminescence System

The Cathodoluminescence apparatus is discussed in greater detail in reference [53]. The general setup is pictured in figure 2.5. Samples were mounted in a *Zeiss* DM950 SEM. An *Oxford* CF301 CL sample stage allowed measurements between $T = 70K$ and room temperature. The luminescence light was collected with an elliptic mirror and focussed on a R457 PMT (for panchromatic CL imaging, sensitivity range 160–850nm) or onto a UV optical fiber connected to a 50cm Spex monochromator. Again, the light was detected with a 1P28 PMT (185–650nm range) and a *Hamamatsu* Photon Counting Unit controlled by a PC and LabVIEW system.

Varying the excitation energy through changing the electron beam acceleration voltage results in different electron penetration depths R_e. The penetration depth can be approximated (in μm) using the Kanaya–Okayama model [54]

$$R_e = \frac{0.0276 \cdot A}{\rho \cdot Z^{0.889}} \cdot E_{beam}^{1.67}. \tag{2.12}$$

The atomic weight is given in units of g/mole and the material density in g/cm^3, while $E_{beam} = e \cdot U_{acceleration}$ is in units of kV. With a focussed electron beam the excitation volume can be approximated by a sphere with diameter R_e. Defocussing the electron beam to beam diameters much larger than R_e however results in an excitation 'cylinder' of height R_e. As a consequence, a change in acceleration voltage directly translates to a change in excitation volume — that is, the differences in spectral features when only

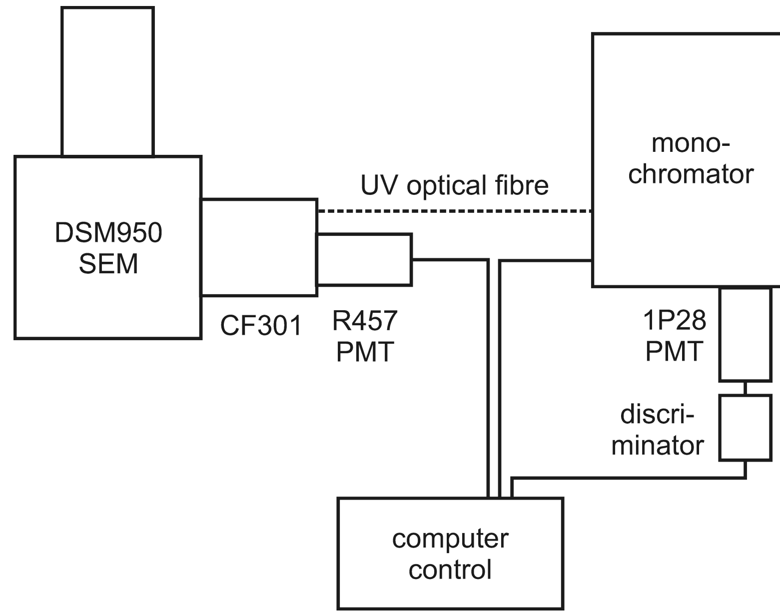

Figure 2.5: Schematic of the Cathodoluminescence setup.

V was changed necessarily have their origin in the additional volume [55]. This feature allows precise control over the characterization of heterostructures.

The optical properties of the $Al_xGa_{1-x}N$ samples, which will be discussed later in chapter 4.2, were determined by Cathodoluminescence spectroscopy. This was mainly done in order to avoid cutting off higher–energy contributions e.g. from hexagonal phase material ($E_g(h-AlN) \approx 6eV$). Moreover, the CL setup possesses a higher UV sensitivity and does not suffer from limitations in excitation energy (HeCd laser at $\lambda = 325nm$) compared to the PL apparatus (see also page 26 in reference [56]).
The electron beam penetration depth R_e can be calculated as shown before using equation (2.12); figure 2.6 visualizes the results for various Aluminum contents x. The materials constants of eqn. (2.12) were assumed to vary according to a Vegard type law [57], i.e., the Aluminum mole fraction x of an $Al_xGa_{1-x}N$ layer changes the quantities linearly

$$A = 41 + (1-x) \cdot 43, \quad (2.13)$$

$$Z = 20 + (1-x) \cdot 18, \quad (2.14)$$

$$\rho = 3.24 + (1-x) \cdot 2.8 \quad (2.15)$$

in their respective units.

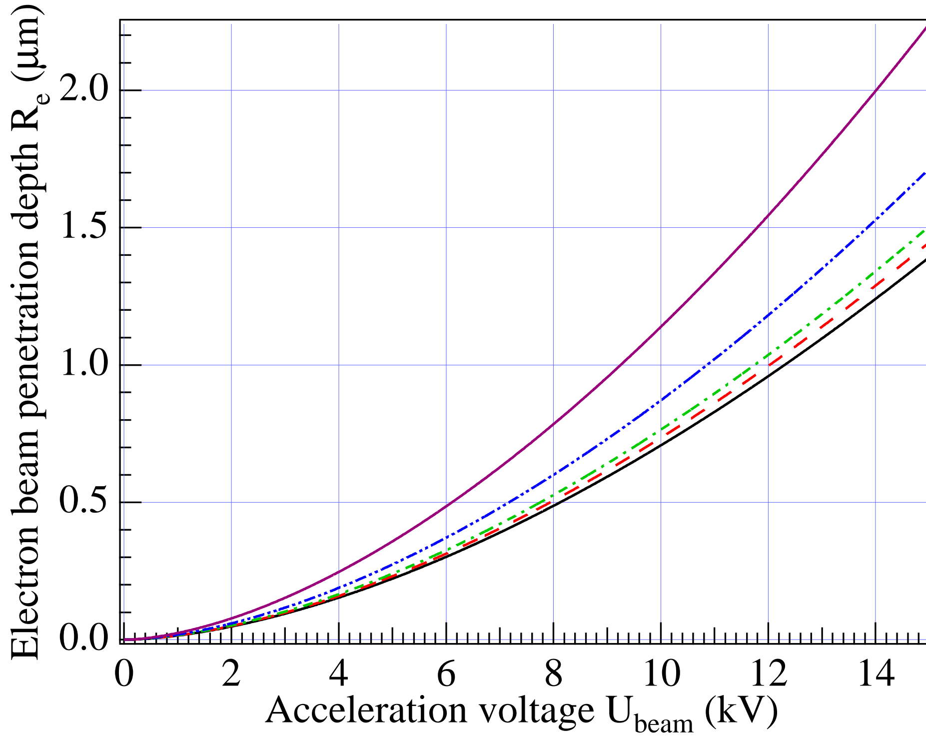

Figure 2.6: Electron beam penetration depths as function of acceleration voltage for different Aluminum mole fractions x=1, 0.5, 0.2, 0.1, 0, ordered from top to bottom.

2.2.2 Electrical Measurements

Electrical measurements are of course very important for the characterization of *opto-electronic* semiconductors.

An ideal semiconductor, free of defects, is characterized by the simplest form of charge neutrality condition, $n = p$. [1] Therefore the total density of free carriers at finite temperatures is given by

$$n_i^2 = n \cdot p = N_V \cdot N_C \cdot \exp\left(-\frac{E_g}{k_B \cdot T}\right). \tag{2.16}$$

Taking the argument to an extrinsic semiconductor, i.e., a semiconductor with e.g. one species of donors, the charge neutrality changes because of the necessary accommodation of ionized donors N_D^+

$$\begin{aligned} n &= N_D^+ \\ &= N_D \cdot \left[1 + g \cdot \exp\left(\frac{E_F - E_D}{k_B \cdot T}\right)\right]^{-1}. \end{aligned} \tag{2.17}$$

[1]This paragraph can be, due to the rather introductory nature of this chapter, only an extremely abridged version of what can be found essentially in any basic textbook on semiconductors, for example in references [58] and [59].

The factor g describes the donor ground state degeneracy, i.e., it allows for the electron spin state.
In the even more general case of a semiconductor containing donor and acceptor species, the neutrality condition changes to

$$n = N_D^+ - N_A^-. \tag{2.18}$$

For this work, electrical measurements are identical with Hall effect measurements. Similar to the above mentioned basic semiconductor statistics, treatments of the Hall effect abound. The Hall voltage

$$U_H = -\frac{1}{n \cdot e} \cdot \frac{I \cdot B}{d}, \tag{2.19}$$

where n carriers of charge e flow with an external current I under the influence of a magnetic field B through a semiconductor slab of thickness d. Defining the *Hall constant* $R_H = -(n \cdot e)^{-1}$, equation (2.19) can be written as

$$R_H = \frac{U_H \cdot d}{I \cdot B}. \tag{2.20}$$

Conventionally a negative sign of R_H means n–type and a positive sign p–type conductivity.

Electrical measurements were conducted on $(5mm)^2$ pieces in van der Pauw geometry [60]. Due to well–known contact problems, the contacts were of Indium–on–Gold type on the extreme corners of the samples, and were annealed for 30 minutes at $T = 400°C$ under a Nitrogen atmosphere. For variable–temperature measurements the sample temperature could be varied between 77K and 420K. A magnetic field of 0.8T was applied. More details are noted in ref. [60].

2.2.3 X–ray Diffraction

X–ray diffraction is, because of the short wavelengths used, especially useful for the investigation of structural properties on an atomic level [61]. In this case, a *Philips* X'Pert materials research diffractometer was used with a Copper anode emitting K_{α_1} radiation at a wavelength $\lambda = 1.54$Å. The X–ray tube is equipped with a line fine focus, which, together with the hybrid monochromator, guarantees a high intensity at low beam divergence of only 47 arc sec. The hybrid monochromator consists of a graded parabolic mirror that parallelizes the X–rays, and a (220) channel–cut Germanium crystal. This Ge monochromator removes K_{α_2} radiation through 4 internal reflections. The samples are mounted onto an Euler cradle that allows independent changes of the angle of incidence ω, diffraction angle 2θ, rotation around the surface normal ϕ and around the incident axis Ψ as well as linear motion in all three directions. Measurements with a 1/16° receiving slit (3 arc min resolution) in front of the proportional counter detector are called 'double axis', while high resolution (20arc sec) measurements were conducted with a second Germanium(220) crystal in front of the detector ('triple axis' configuration). A schematic of the diffractometer can be seen in figure 2.7.

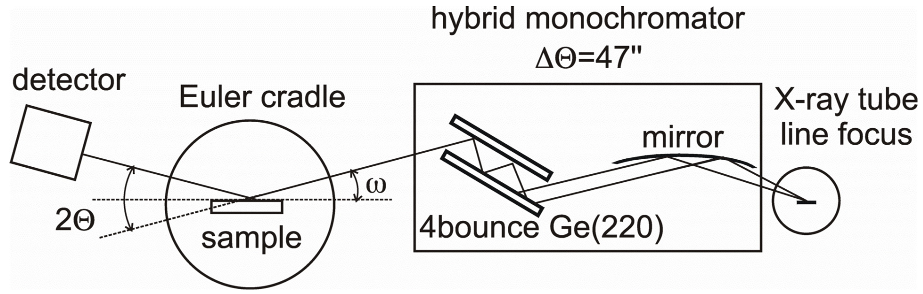

Figure 2.7: Schematic of the materials research diffractometer.

For a single–crystal the diffraction of X–rays is described by the Bragg condition:

$$\lambda = 2 \cdot d_{hkl} \cdot \sin(\theta). \tag{2.21}$$

The triplet (hkl) denotes the Miller indices, and d_{hkl} the spacing of the respective lattice planes. For the case of cubic crystal symmetry and a lattice constant a_0, the lattice spacing is given by

$$d_{hkl} = \frac{a_0}{\sqrt{h^2 + k^2 + l^2}}. \tag{2.22}$$

So–called '$\omega - 2\theta$' scans are measurements where the angular rotational speed of the detector is twice as high as the angular speed of the sample (ω). $\omega - 2\theta$ scans through symmetric reciprocal lattice points, i.e., reflections from lattice planes parallel to the sample surface, gives information exclusively with respect to vertically aligned properties. In contrast, asymmetric $\omega - 2\theta$ scans yield convoluted information about both parallel and perpendicular crystal parameters. The so–called 'rocking curve' (also RC or 'ω') is a scan with the detector at a fixed angular position, while only the sample moves (rocks), changing the incidence angle ω. Obviously, in close proximity to the reflex in question both $\omega - 2\theta$ and ω are perpendicular with respect to each other, allowing an estimate of the total width of the reflex.

2.3 Molecular Beam Epitaxy

In the light of the many publications concerning Molecular Beam Epitaxy, MBE and ultra–high vacuum techniques, dealing with MBE at great lengths probably comes close to beating a dead horse [62, 63, 64, 65, 66]. However a few points certainly have to be noted, especially with respect to the focus of this thesis.

In Molecular Beam Epitaxy, single atoms are mostly produced through thermal evaporation of elements from crucibles, making the use of precursors unnecessary. The shape of the cells causes a highly directional collimated beam which is characterized by the atom flux F or the beam equivalent pressure BEP. Through the reaction of the single atoms on the substrate — complex since it comprises adsorption, desorption, chemisorption and surface migration processes &c. — the epitaxial film is formed. The properties of this film are, assuming steady state growth conditions, determined by substrate temperature and atom fluxes, the so–called MBE window. Usually the

atom fluxes are controlled via the respective BEPs as measured with the beam flux Bayard–Alpert ion gauge, and via cell temperatures.

MBE as a materials growth technique uses the fact that in UHV the particle mean free paths are larger than the system dimensions. This makes it possible to use ultra–pure materials sources, while the evaporated atoms simply cannot collide before hitting the sample surface. At the same time, the extremely low background pressure (on the order of $p \approx 10^{-10} mbar$) means that only few impurity atoms are incorporated during growth. Furthermore, shutters enable the instantaneous blocking of molecular beams, thus allowing interface control virtually on an atomic level. Likewise, *in situ* real–time control of the crystal growth front is possible using RHEED, ellipsometry or reflectometry [67, 68, 69, 70, 71, 72]. Moreover, since MBE is inherently a non–equilibrium growth technique, it is possible to grow alloys or material phases that are unstable under customary production conditions.

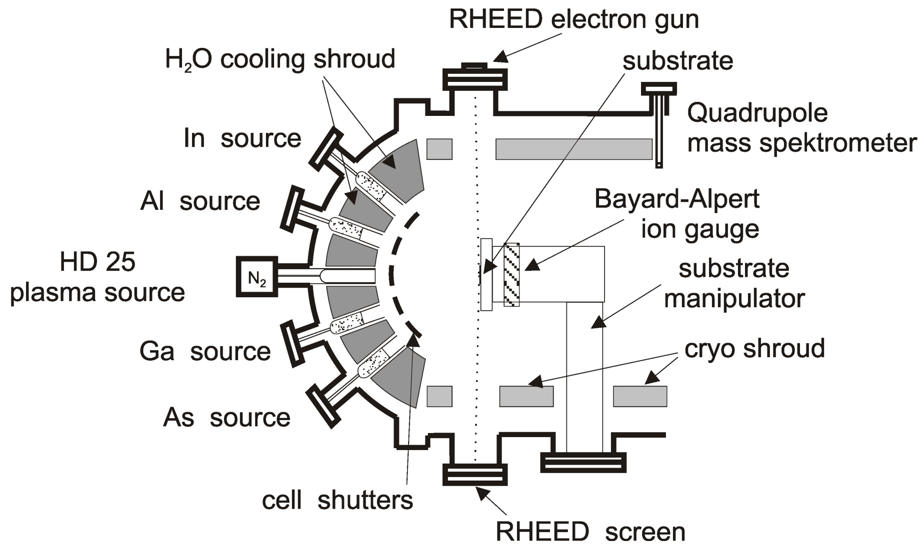

Figure 2.8: Schematic of an MBE system.

The principal layout of a conventional MBE system is shown in figure 2.8. In the case of this work, a commercial *Riber* MBE 32 system is used. Six effusion cells are mounted such that their axes converge on the center of the substrate in growth position. Additionally, an *Oxford Applied Research* HD25 rf plasma source is available for delivering activated Nitrogen. The substrate azimuth can be continuously rotated throughout in order to increase the layer uniformity.
The effusion cells are standard ABN135 cells and controlled by *Eurotherm* temperature controllers. During normal use, the cell temperature T is the control parameter. It is connected to the molecular flux through the well–known Knudsen formula [64]

$$\frac{F}{A} = \frac{N_{Avo} \cdot p}{\sqrt{2 \cdot \pi \cdot M_{mol} \cdot k_B \cdot T}}. \tag{2.23}$$

Here, p equals the beam equivalent pressure, F the atom flux and A the cell aperure. Samples are introduced through a second, transfer, chamber, so the vacuum of the

actual MBE vessel stays at UHV at all times. During growth experiments, a cryoshroud with liquid Nitrogen decreases the rest gas level by a further order of magnitude.

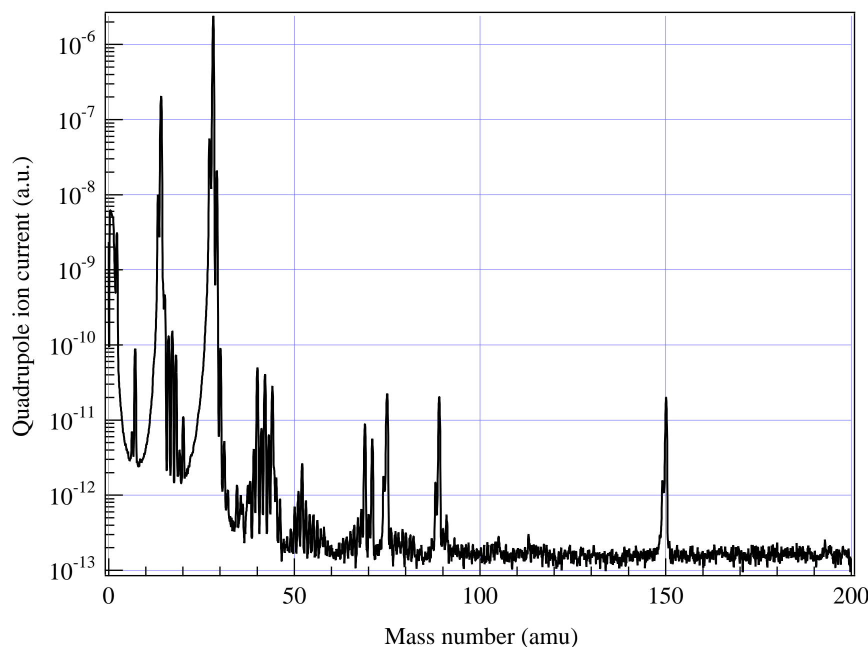

Figure 2.9: Typical quadrupole mass spectrum, covering the whole range up to 200amu.

The rest gas level was monitored by means of a Quadrupole mass spectrometer. The QMS in question was equipped to monitor species up to an atomic mass of 200amu. A typical spectrum recorded with operating Nitrogen cryoshroud is shown in diagram 2.9, while figure 2.10 details a section. Typical feature of a QM spectrum is the water disintegration chain at 18→17→16amu caused by the loss of a Hydrogen atom upon ionization. Furthermore, the peaks at 75amu and 150amu, respectively, denote relatively large amounts of Arsenic in the growth chamber. This is, however, well–known for As–equipped systems. Unfortunately, the position of the QMS did not allow the direct measurement of atom beam fluxes (beam equivalent pressure), however in this way the spectra represent the true background.

2.3.1 Gallium Nitride Growth

As mentioned before, the hexagonal phase is the equilibrium phase of Gallium Nitride, albeit with only a small energy difference. Nonetheless, successful growth of cubic GaN has been reported by several groups. One factor to be considered seriously in this regard is the choice of substrate. The feasibility of a variety of cubic substrates has been demonstrated, such as MgO [73], 3C–SiC [74, 75, 76], Si [77], and GaAs [78]. With these different materials, however, cost, quality and availability need to be factored in. Obviously, from a crystallographic point of view, 3C–SiC would be the obviously next best choice apart from c–GaN homoepitaxy because of the small lattice

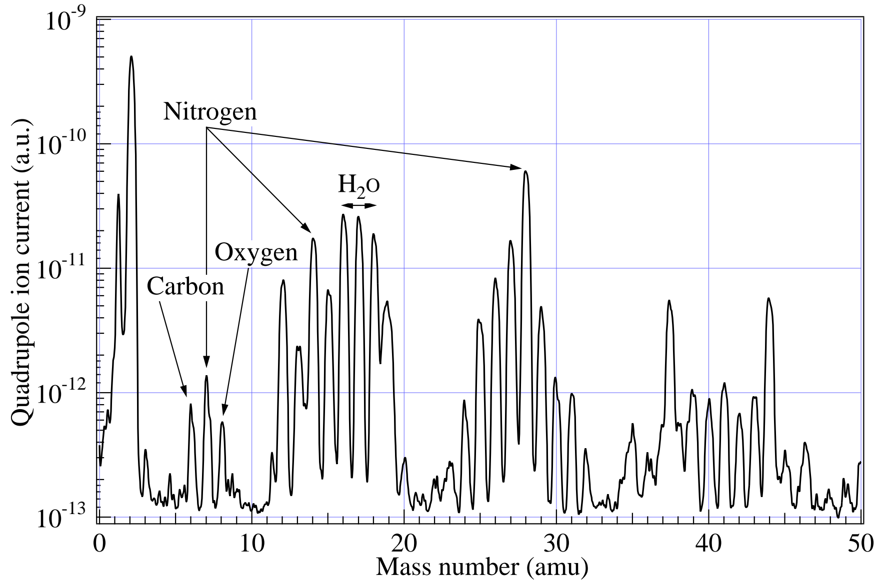

Figure 2.10: Section of a quadrupole mass spectrum.

misfit f of about 3.7% (see equation (2.24) and reference [79]) compared to MgO [80] with $f = 7.4\%$ or GaAs [79] at $f = 20.0\%$:

$$f = \frac{a_{0,sub} - a_{0,layer}}{a_{0,sub}}. \tag{2.24}$$

Unfortunately, this is also a question of substrate availability. The misfit of 20% between GaN and readily available cheap and well–known GaAs is rather large. Still, epitaxial growth could be demonstrated by MBE as well as MOVPE. The growth of GaN layers by MBE has been discussed in reference [62]. It has been argued that the unexpectedly well–proceeding growth process of c–GaN on highly mismatched GaAs substrates is due to a *magical mismatch* 5:4 [81], i.e., 5 GaN lattice constants fit on 4 GaAs lattice constants. Yet GaN epitaxial layers require the growth of a low–temperature buffer layer [82].

2.3.2 Gallium Nitride Nucleation

It has been shown that the inital growth of GaN is of tremendous importance in order to obtain high–quality, high–phase purity cubic GaN epilayers [75, 78, 83, 84]. In order to improve the overall qualities of the GaN layers grown in the course of this work, the influence of the nucleation and the subsequent transition to the regular growth process was studied.

For the purpose of this study, nucleation layers were deposited where the parameters nucleation time, incident Ga flux, substrate temperature T_S and the transition to normal growth were varied one at a time, keeping all others constant. After growing the low–temperature nucleation layer and ramping the conditions to growth, GaN epitaxial layers were grown under conditions reported before [62], while greatest care was taken to ensure the reproduceability of the actual epilayer growth.

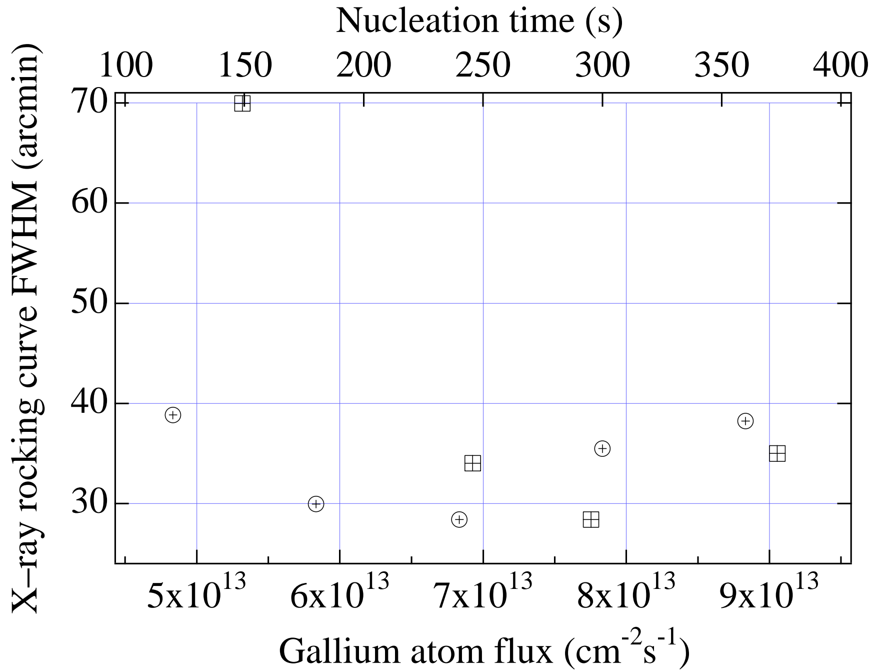

Figure 2.11: X–ray rocking curve FWHM of cubic (002) reflection for GaN epilayers of 600nm thickness. Results represent two series of experiments with varying Gallium fluxes and nucleation times, respectively. Circles denote the evolution of RC half–width over nucleation time (top abscissa), while squares show the variation with Ga flux (bottom abscissa).

Diagram 2.11 showcases two of these series of experiments. The only parameter that was varied was (a) the Ga flux during nucleation — squares in the diagram, bottom axis as abscissa — while holding constant all other parameters, especially substrate temperature and nucleation time, and (b) the nucleation time — denoted by circles, top axis as abscissa —, respectively. For each sample the substrate temperature was calibrated through observation of the transitions between different GaAs surface reconstructions, i.e. the growth phase diagram [85]. For the experiments detailed here, the substrate temperature during nucleation was $T_{sub} = 600°C$. The Gallium fluxes were likewise calibrated through GaAs specular spot RHEED oscillations [64]. The flux of active Nitrogen was determined as $f_N = 1.4 \cdot 10^{14} cm^{-2} s^{-1}$. The transition to normal growth conditions was done at a constant temperature ramp, and all samples were grown to a nominal thickness of 600nm. Post growth characterization utilized photoluminescence, AFM and X–ray measurements. FWHM values of the rocking curves of symmetric (002) reflexes of cubic Gallium Nitride were obtained by fitting the experimental data. Diagram 2.11, representing a minimum X–ray FWHM of 28 arc minutes, is clear proof that through careful design of the nucleation process it is possible to achieve a degree of perfection comparable to or even excelling the published results that use much more complex processes such as ELOG or substrate patterning [86, 87].

Since both series show the same optimum with respect to the structural perfection of the epilayer, it appears tempting to make a closer comparison. This is demonstrated in

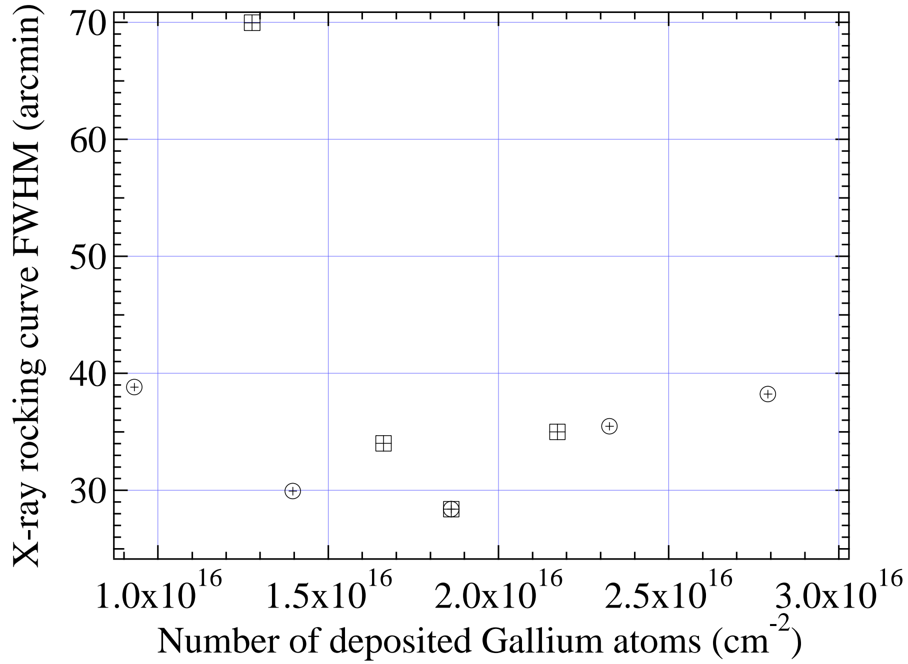

Figure 2.12: X–ray rocking curve FWHM of cubic (002) reflection for samples with different nucleation processes; circles for time–varying and squares for flux–varying experiments, substrate temperature T=600°C.

figure 2.12, where the rocking curve FWHMs of fig. 2.11 are shown as a function of the total number of Gallium atoms adsorbed on the surface during nucleation. Again, the circles mark the results from the time–variation series and squares denote experiments with Gallium flux variation. The calculation of the total number of deposited Gallium atoms,

$$total\,number = F_{Ga} \cdot t_{Nuc}, \tag{2.25}$$

of course implies a sticking coefficient of Gallium on GaAs of unity. At the relatively low working temperatures of $T_{sub} = 600°C$ this is however a reasonably safe assumption. The optimum Gallium coverage therefore can be given as $\theta = 1.85 \cdot 10^{16} cm^{-2}$, corresponding to a nucleation layer thickness of 19 monolayers, or $d = 43$Å. Moreover the X–ray results are supported by photoluminescence measurements which give a minimum of exciton linewidths for corresponding Gallium coverages, as demonstrated in figure 2.13. Furthermore, the experiments detailed above demonstrate that optimum nucleation conditions demand a Nitrogen:Gallium ratio of 2, i.e., a slight Nitrogen excess (different from the normal epilayer growth conditions).

This result is at first glance surprising, since it actually implies that the single most paradigm of nucleation theory is invalid. This universally acknowledged model describes the necessity of achieving a high supersaturation in order to form a high nucleation density. This high density of stable nuclei is typically achieved via (a) low temperatures, thereby reducing re–evaporation from the surface and lowering the adatom mobility on the surface, and (b) through high atom fluxes.

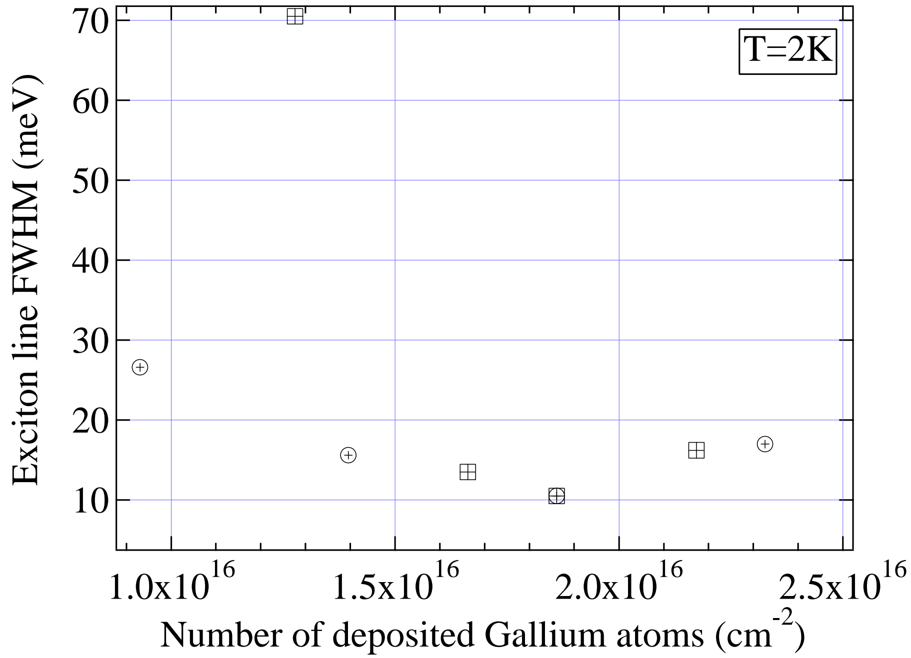

Figure 2.13: Linewidths of c–GaN exciton transitions for samples with different nucleation processes; symbols bear the same meanings as in the preceeding figure.

Condition (a) is easily met by growing the nucleation layer at low temperatures. The apparent puzzle of how (b) fits into the picture presented so far is, however, easily solved when comparing the different steps. Classical nucleation theory is typically concerned with only fractional coverages, i.e., less than one monolayer deposited. As can be seen in figure 2.14, this situation is reached very fast, within the first five to ten seconds. In this respect it is especially important to notice that the fractional coverages of 1/13, 1/9 and 1/4 indicated in the graph correspond to adatom distances of $3a_0$, $3/\sqrt{2}\,a_0$, and $\sqrt{2}a_0$, respectively. It stands to reason that the process of the formation of the nuclei happens so fast that — within sensible limits of course — no dependence on the respective Gallium flux can be observed. Moreover it is important to notice that during the formation of the first GaN monolayer — provided this proceeds in a two–dimensional way — only GaAs lattice sites are available. Due to the larger unit mesh of GaAs compared to GaN, and therefore lower atom density — $2/a_0^2 = 6.258 \cdot 10^{14} cm^{-2}$ for GaAs compared with $2/a_0^2 = 9.789 \cdot 10^{14} cm^{-2}$ (GaN) — , similar coverages would be completed faster at a constant atom flux. This is demonstrated in fig. 2.14, where the lower curve (with diamonds) denotes the coverage of a GaAs surface, while the upper curve (circles) corresponds to the coverage of GaN. Trampert *et al.* demonstrate with the help of TEM images that three-dimensional islands form already at 0.5 monolayers coverage [81]. Therefore, the aforementioned progression from GaAs to GaN does indeed happen very quickly. This supports the aforementioned observation that the total nucleation layer thickness is important for the GaN quality, and that the initial flux is of lesser influence. At the end of the low–temperature GaN nucleation process a continuous GaN layer has formed, which contains the structural

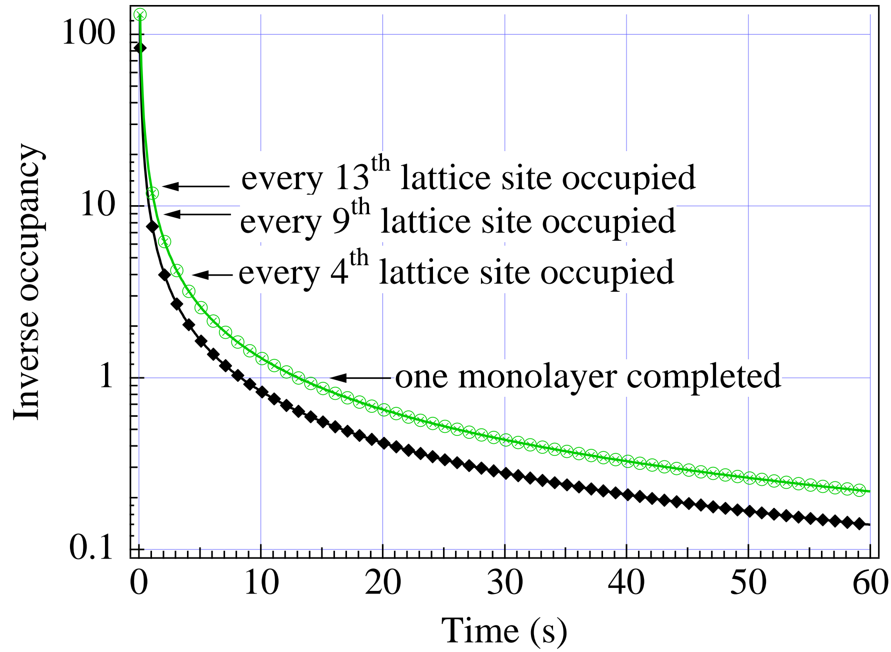

Figure 2.14: Coverage of a GaAs (diamonds) and a GaN (circles) surfaces with a flux of $\mathrm{F_{Ga}} = 7.5 \cdot 10^{16}\mathrm{atoms\,cm^{-2}s^{-1}}$.

defects due to the accommodation of the large difference in lattice constants. The nucleation layer needs to be transformed to a flat two–dimensional GaN growth front; otherwise surface roughness exposes GaN(111) planes onto which hexagonal phase GaN will nucleate [75]. This transformation proceeds during the increase of the substrate temperature from T_{Nuc} to $T_{growth} = 720°C$ [62].

Chapter 3

Carbon Doping of GaN

In the past decades, controlled p–type doping of GaN has been the largest obstacle on the way to functioning optoelectronic devices. The use of Magnesium paved the way to commercial success, making reproducible doping levels and profiles possible. However, although Magnesium by far is the acceptor of choice, it presents a number of problems. First of all, Mg has a high activation energy in GaN (and even higher in AlGaN), so only 5 percent of the incorporated Magnesium acceptors are electically active at room temperature [88]. This leads to reported hole concentrations usually in the low to mid $10^{17} cm^{-3}$ range. Further, Magnesium displays a tendency for self–compensation [89]. During MOCVD growth Mg forms a stable chemical bond with excess Hydrogen (from the metalorganic precursors). In order to obtain electrically active acceptors, this bond has to be broken requiring an additional technological step.
In MBE growth of cubic Gallium Nitride, phase purity and overall structural quality demand Ga rich growth processes (see, for example, reference [90] and references therein). Magnesium as an acceptor however substitutes Gallium, therefore in terms of promoting Mg incorporation it appears advantageous to implement a growth process employing Nitrogen excess, which is contrary to the aforementioned conditions.

Several methods of Gallium Nitride Carbon doping have been reported in the literature so far [91] — [98]. By far and large, most are concerned with the utilization of Carbon tetrachloride, CCl_4, in MOVPE growth. Abernathy *et al.* and Armitage *et al.* claim a negative side effect on GaN growth properties due to the presence of Chlorine radicals and the subsequent formation of $GaCl_3$, i.e. a reactive etching of the epitaxial layer [91, 92]. Armitage *et al.* overcome this problem by simply increasing the gallium flux until Ga rich growth conditions are reached again. It is however not easily clear why the possible formation of $GaCl_3$ should impede GaN growth so drastically, since it acts as Ga source material in high–rate HVPE growth. Neither reference, however, reports successful growth of actual p–type GaN layers; they mainly report high–resistivity semi–insulating epilayers. This is in fact indicative of the incorporation of Carbon acceptors and thus of a concomitant compensation of the background electrons, as nominally undoped GaN layers usually exhibit n–type conductivity. The same results were reported by Birkle *et al.*, who used MBE growth and Carbon evaporation from a graphite filament [97].

3.1 General Considerations

Because of the importance of Magnesium for GaN doping, the theoretical work concerning the doping of GaN has largely focussed on hexagonal phase material and the properties of Magnesium. However, because of the high degree of commonality between the two phases — second nearest neighbour distances are equal, differences arise only for third nearest neighbours — in principle it should be possible to apply results for hexagonal material to cubic GaN. This mutual correspondence manifests itself already in very similar band structures (see references [15, 18, 19, 21, 22, 23, 27, 99] and the preceding chapter), band gaps, elastic properties and last but not least reaction kinetics.

In agreement with the above–mentioned observation of a rather considerable disagreement between the results of theoretical calculations concerning correct band gaps, a literature search yields a wide variation of defect activation energies, both between different material phases and within the same phase (as can be seen in tables 2.1 and 2.2).

Bogusławski *et al.* calculate the activation energy of the Nitrogen substituent Carbon as $E_A = 0.2eV$ [101, 102]. The formation energy of this C_N varies between $E_f = 1.1eV$ for Ga rich growth conditions and $E_f = 2.8eV$ for Nitrogen rich growth. Wright finds a Carbon activation energy of $0.2eV$ as well [103]. While both note that the energies in cubic material should not differ much from their calculated hexagonal values — following the argument outlined above —, Mireles *et al.* find a remarkable difference of about 100meV [6]. According to Mireles *et al.*, C_N in cubic GaN possesses an $E_A = 147meV$ as compared to $E_A = 241meV$ for h–GaN. Again, this may well be caused by the different computational methods applied by the different authors.

In this regard it might be interesting to look at chemical trends between different III–V semiconductors concerning their respective acceptors. Figure 3.1 delineates the acceptor energies of Cadmium, Zink, Magnesium, and Carbon for both Gallium Arsenide and Gallium Phosphide (abscissa). Comparing those energies with their respective values in Gallium Nitride (ordinate), it is noteworthy that the rather well–known Cd, Zn and Mg lie on a straight line for both semiconductors. If Carbon could be assumed to follow this trend, it should be expected to possess an acceptor activation energy of 215meV.

On the other hand words of caution are needed against an overly strong reliance on chemical similarities. As argued in greater detail by Schubert, group IV elements such as Carbon and Silicon are inherently amphoteric defects in group III— group V compound semiconductors, i.e., they may act as donors or acceptors, depending on the occupation of cation or anion lattice sites [58]. This was confirmed by theoretical considerations by Bogusławski *et al.*, who discussed the susceptibility of wide–gap semiconductors in general to self–compensation, and the energetics of Carbon in GaN and AlN [101, 104]. However, so far Silicon is known in Gallium Nitride exclusively as donor (substituting Gallium), and Carbon on Nitrogen sites as an acceptor. It is beyond the scope of this work to determine the difference in occupancy mechanisms between GaAs and GaN; however it may be speculated that this again is due to the extremely high degree of ionicity found in III–Nitrides as compared to other III–V

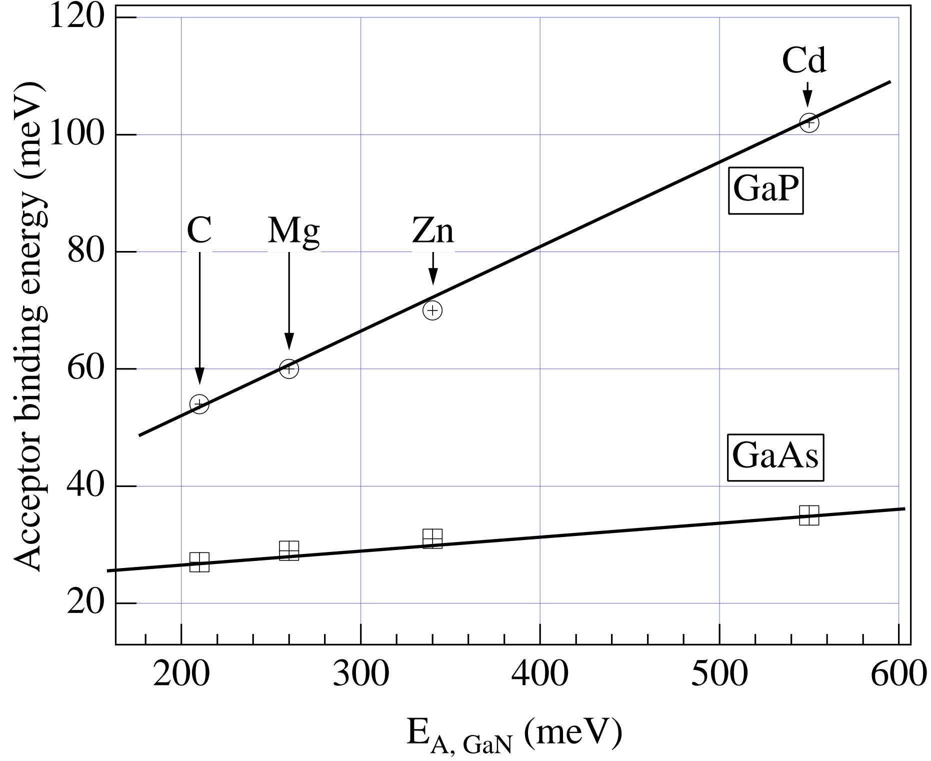

Figure 3.1: Comparison of chemical trends in III–V semiconductors GaAs, GaP and GaN with regard to the respective acceptor binding energies.

compound semiconductors.

For a very basic approximation of the dopant incorporation it might suffice to compare the covalent radii of the different constituents. Carbon possesses a tetrahedral covalent radius of 0.77Å, which equals almost that of Nitrogen at 0.7Å[105]. On the other hand, Magnesium has a covalent radius of 1.4Å, which exceeds even that of Gallium (1.26Å). Therefore a tendency for Carbon incorporation on a Nitrogen lattice site might be expected.

Because of the high activation energy of $E_A = 215meV$, only about 5% of the Carbon acceptors are electrically active at room temperature (see also reference [9]). This follows easily when considering the hole concentration p of a non–compensated semiconductor,

$$p = \sqrt{\frac{N_A \cdot N_V}{\beta}} \cdot \exp\left(\frac{E_A}{2 \cdot k_B \cdot T}\right). \quad (3.1)$$

Here N_A denotes the (Carbon) acceptor concentration, E_A the acceptor activation energy, k_B the Boltzmann constant and T the temperature, respectively, while β is the valence band degeneracy factor, and the valence band density of states

$$N_V = \frac{2}{\hbar^3} \cdot \left(\frac{m_h * \cdot k_B \cdot T}{2 \cdot \pi}\right)^{3/2}. \quad (3.2)$$

3.2 Carbon Doping Source

Because of the high activation energy of the Carbon acceptor in Gallium Nitride, a comparatively high Carbon incorporation has to be achieved. This necessitates relatively high Carbon fluxes considering that it is only a doping element, which together with the extremely low vapour pressure demands a high temperature of the evaporant material. This is immediately obvious from the vapour phase diagram as a function of temperature, as shown in figure 3.2 [106]. It is only at temperatures in excess of 2000 Kelvin that measurable Carbon quantities can be expected. The flux rates shown on the right of the diagram 3.2 are provided for a comparison with the fluxes used in later diagrams. They were calculated from the Knudsen formula (2.23) with $M_{mol} = 12g/mole$ as Carbon molar weight, and all other symbols having their usual meaning.

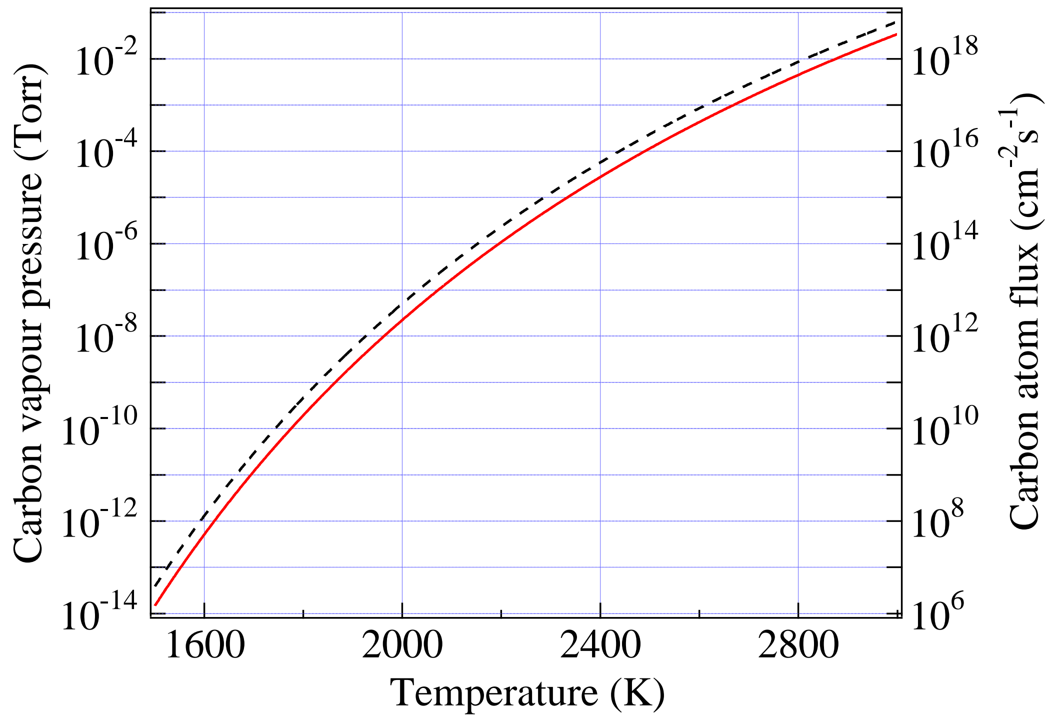

Figure 3.2: Vapour pressure of graphite, after Landolt/Börnstein (left), and resulting atom flux (right, dashed line).

Source Description

For the relatively well–established C doping of MBE grown Gallium Arsenide based structures, evaporation from a graphite filament is very common [107] — [112], although other Carbon sources were also utilized, e.g. plasma–cracked Carbon tetrabromide CBr_4 [113, 114] or an electron beam source [115, 116].

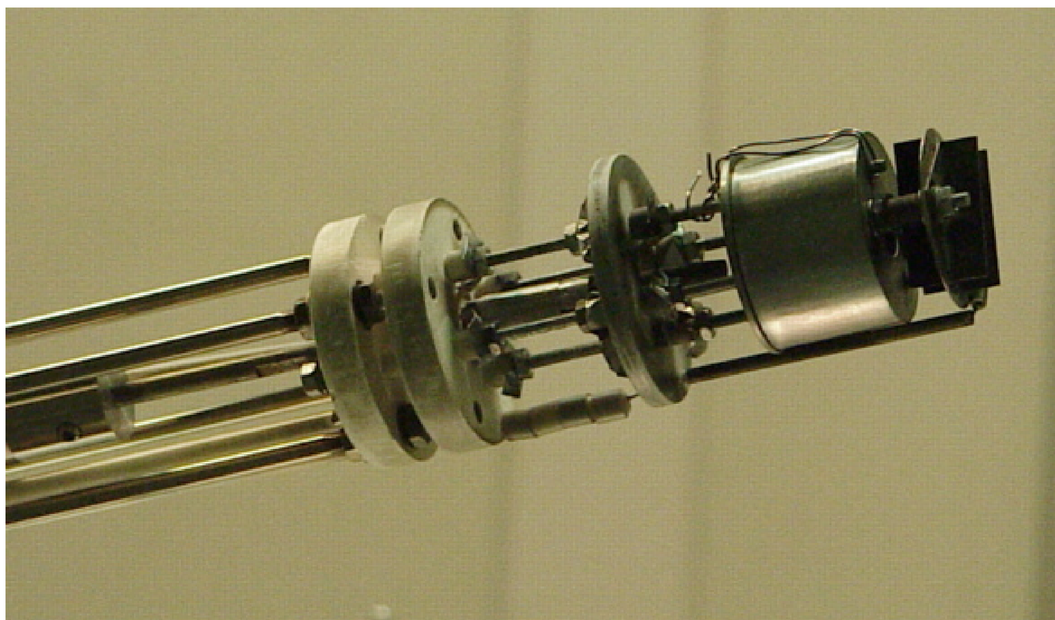

Figure 3.3: Head of the e^-–*flux* cell.

The Carbon doping cell that was used for the doping experiments discussed in this work is originally based on an e^-–*flux* cell made by *tectra GmbH*, Frankfurt (Main), using electron beam heating. During the course of this work greater efforts had to be devoted to the adaptation of this cell to the rather demanding GaN MBE environment. These efforts included ruggedizing and partially replacing the cell structure. This cell is shown in figures 3.3, 3.4 and 3.5, and referred to in the following as *e–beam* or *e–flux* source. A graphite rod of 4 mm diameter is placed on high positive potential of about $U = 1 - 2\ kV$ with respect to a Tungsten filament. Evaporation took place in a Tantalum enclosure (see figure 3.3) furnished with an aperture system in order to produce a directed beam of Carbon atoms. The evaporation conditions were reproducibly determined by the acceleration voltage and the emission current I_e between filament and graphite rod.

Because of the shortcomings of the e–flux source, a second Carbon evaporation source was developed during the course of this work, in the following called *filament cell*. It is based on the aforementioned thermal evaporation from a graphite filament. The pyrolytic graphite filament, as shown in fig. 3.6, is cut from a solid PG block. The tantalum foil around the top of the cell serves as a thermal radiation shield and, additionally, acts as an aperture, limiting the solid evaporation angle. Figures 3.6 and 3.7 show the filament cell. Since the evaporation conditions remain fairly stable, the filament current (approximately 50 Amperes) is the primary means of flux control during growth. Additionally, a type C thermocouple can be used, but the Eurotherm temperature controllers possess only a limited operating range up to $2400°C$.

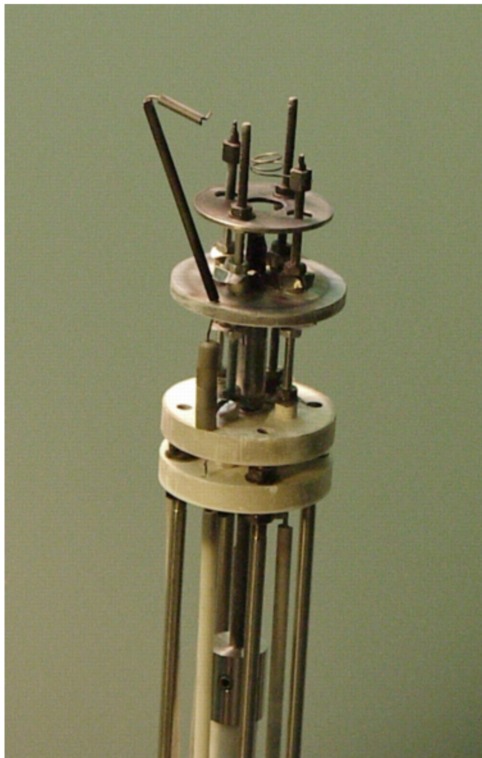

Figure 3.4: Detail of the e^{-}–*flux* cell: view of filament and graphite rod.

Source Calibration and Characterization

Similarly to the usual quantification process of measuring the atom flux of a Knudsen cell via RHEED specular spot intensity oscillations as discussed e.g. in references [64, 68], the Carbon flux was determined by doping the well–known GaAs. Carbon acts in Gallium Arsenide as a shallow donor with $E_A = 6meV$ when substituting Gallium atoms, and as a shallow acceptor of $E_A = 27meV$ when incorporated on an Arsenic lattice site [79]. However, the formation of C_{As} during MBE is greatly favoured, as evidenced by the p–type conductivity of the GaAs:C films. Because of the relatively low activation energy, all Carbon acceptors are ionized at room temperature. This means that RT Hall measurements of GaAs:C epitaxial films of known thickness, grown on semi–insulating GaAs substrates, provide an accurate measure of the Carbon incorporation rate. A similar method was used by Birkle *et al.* [97]. The Gallium Arsenide films were grown under RHEED control at a stable (2x4) reconstruction indicative of favourable As stabilized growth conditions, resulting in optimum quality. The growth rates were determined using RHEED oscillations to $\approx 300nm/h$. All GaAs films were grown to 1000 nm thickness.

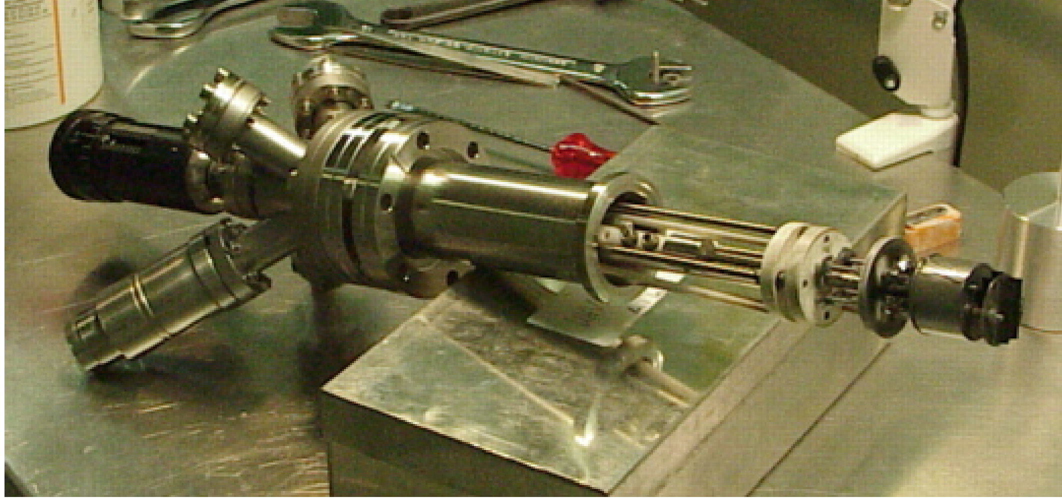

Figure 3.5: Total of e^-–*flux* cell.

The calibration method discussed here relies on three basic assumptions, however:

- The sticking coefficient of Carbon on the growth surface of GaAs, as well as the sticking coefficient on GaN, is unity, or at least both are equal.
- Incorporation as an acceptor in GaAs occurs via non–metal substitution, much like GaN doping; however GaAs is grown using a group V overpressure rather than a metal overpressure as is the case with GaN. This should have no consequences though.
- The Carbon–related defects in GaN and GaAs act exclusively as single–valenced donors and acceptors, respectively.

Because of the inherently amphoteric nature of Carbon in III–V compounds it seems natural to assume at least partial compensation. On page 60 of reference [117], a diagram can be found which details various hole mobility values in GaAs as a function of different compensation ratios N_I/p. For moderate C doping levels the formation of multiple donors in terms of e.g. split interstitials ([112, 118, 119, 120, 121]) or Carbon complexes can be excluded with a reasonable degree of safety. Therefore it is possible to calculate the Carbon concentration in the GaAs:C film for a known compensation ratio from the measured hole concentration p, since the ionized impurity concentration $N_I = N_A + N_D$, i.e., the total number of incorporated Carbon impurities

$$N_C^{GaAs} = N_I = p \cdot N_{compensation}. \tag{3.3}$$

Given the fact that GaAs growth proceeds under As rich conditions, the growth process is Gallium limited and RHEED intensity oscillations yield a ready measure of the Ga atom flux (see e.g. [62, 64]). Therefore, the ratio of Carbon flux and Gallium flux determine the C density:

$$\frac{F_C}{F_{Ga}} = \frac{N_C^{GaAs}}{N_{Ga}^{GaAs}}, \tag{3.4}$$

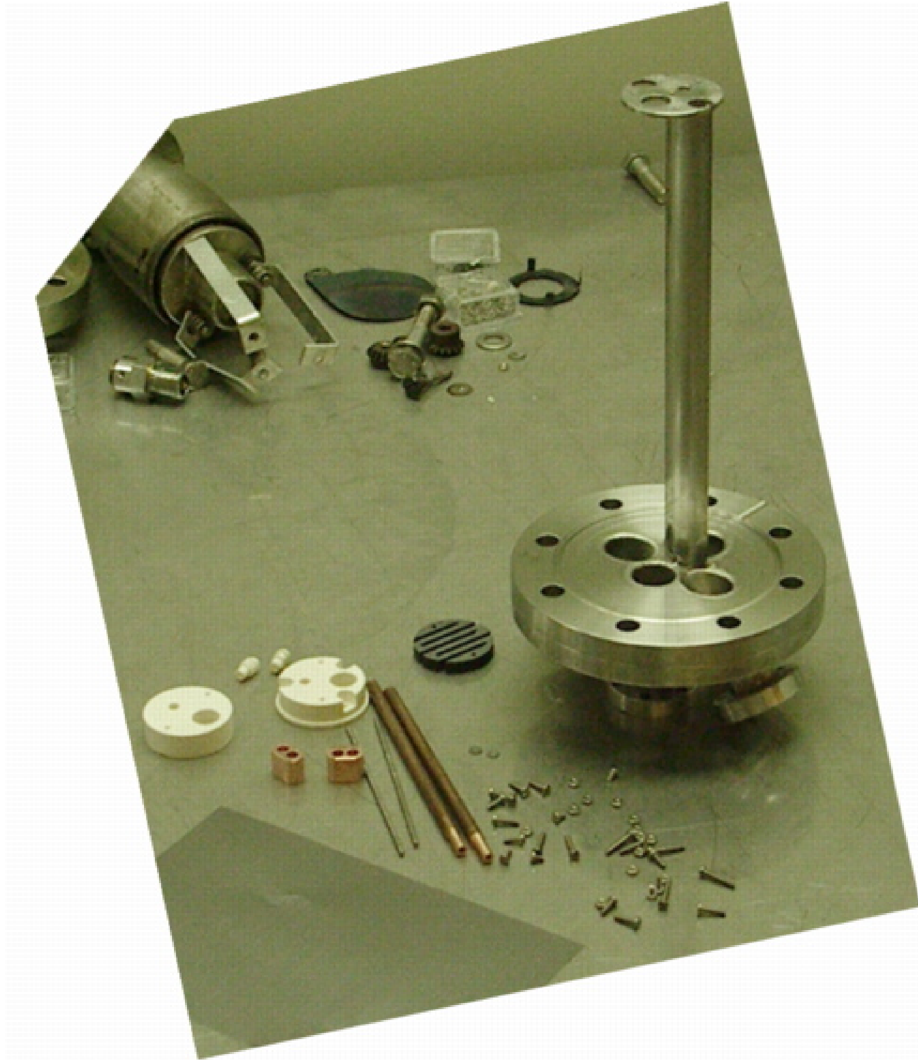

Figure 3.6: Parts of the thermal evaporation cell, before assembly.

which can be reformulated to give the C flux as a function of the known parameters:

$$F_C = F_{Ga} \cdot \frac{N_C^{GaAs}}{N_{Ga}^{GaAs}} = p \cdot N_{comp} \cdot \frac{F_{Ga}}{N_{Ga}^{GaAs}}. \tag{3.5}$$

Here, $N_{Ga}^{GaAs} = \frac{4}{a_0^3} = 2.214 \cdot 10^{22} cm^{-3}$.

Additionally, it is instructive to consider the background doping. Nominally undoped GaAs samples exhibited p–type conductivity with a RT hole concentration of about $p = 2 - 5 \cdot 10^{15} cm^{-3}$ and a mobility $\mu > 400 cm^2/(Vs)$. Therefore the background doping was considered to be equivalent to a Carbon flux $F_C = 4.5 \cdot 10^7 cm^{-2} s^{-1}$. Graph 3.8 presents the resulting calibration curve for Carbon.

A quadrupole mass spectrometer was used for additional characterization of the Carbon doping material. The mass spectra clearly showed that no Carbon dioxide emission or formation took place. Diagram 3.9 shows the relative intensities of peaks

Figure 3.7: Graphite cell with evaporation from resistively heated graphite filament.

6amu (squares) and 12amu (dots) as a function of Carbon flux.

First, both masses exhibit a constant intensity ratio independent of source power. This is clear evidence that the nature of the evaporated species does not change with the power applied, i.e., there is no transition from Carbon atoms to dimers (or even larger aggregates).

Second, since the experimental points are shown in the temporal order in which they were actually measured — with a settling time of 30 minutes per point — it can be concluded that Carbon shows only a neglectable memory effect on the MBE system. This marks an outstanding advantage of using an elemental Carbon source over other Carbon sources, or Magnesium as dopant, respectively. Similar results have been published for GaAs growth [122].

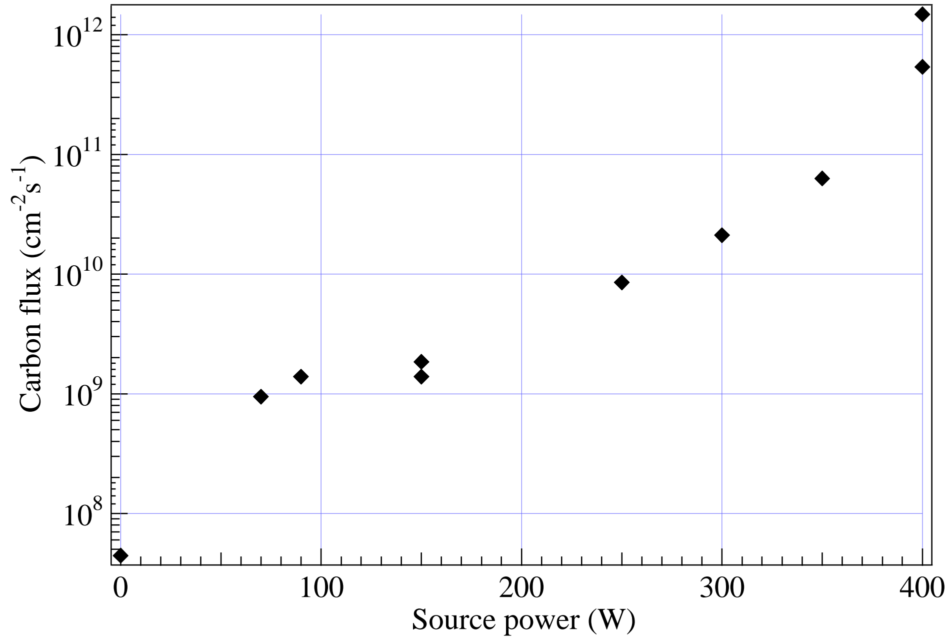

Figure 3.8: Carbon flux calibration curve as discussed in the text.

3.3 Measurements and Results

The measurements presented in the following were performed on Carbon doped GaN epilayers grown as noted before and detailed elsewhere in the literature [82]. Except where noted otherwise, the film thickness totalled 1μm. GaN layer thicknesses were calculated from thin film interference fringes measured in reflection, under almost normal incidence [123]. The GaN index of refraction, as published in reference [50], was used. The procedure and an example spectrum are shown in detail in chapter 2.2.1 and figure 2.4. The GaAs substrate was semi–insulating and therefore did not contribute to electrical measurements. Photoluminescence measurements likewise were dominated by GaN:C bulk properties, because the GaN layer thickness exceeded the penetration depth of the 325nm HeCd laser.

The accuracy of the Carbon flux calibration method, as outlined in the preceding section, was confirmed independently by means of SIMS measurements. A maximum Carbon concentration of $N_C = 2 \cdot 10^{20} cm^{-3}$ could be detected [124].

3.3.1 Structural Properties

X–ray Characterization

As X–ray studies probe the samples' structural properties, $\omega - 2\theta$ scans and rocking curves yield insight into the degree of twist or mosaicity present [125]. It is instructive to note that both $\omega - 2\theta$ and ω scans — examples are shown in fig. 3.10 — display FWHM values of 8 arc min and 23 arc min, respectively. These values are quite comparable to values reported in the literature for cubic phase material, and for undoped c–GaN

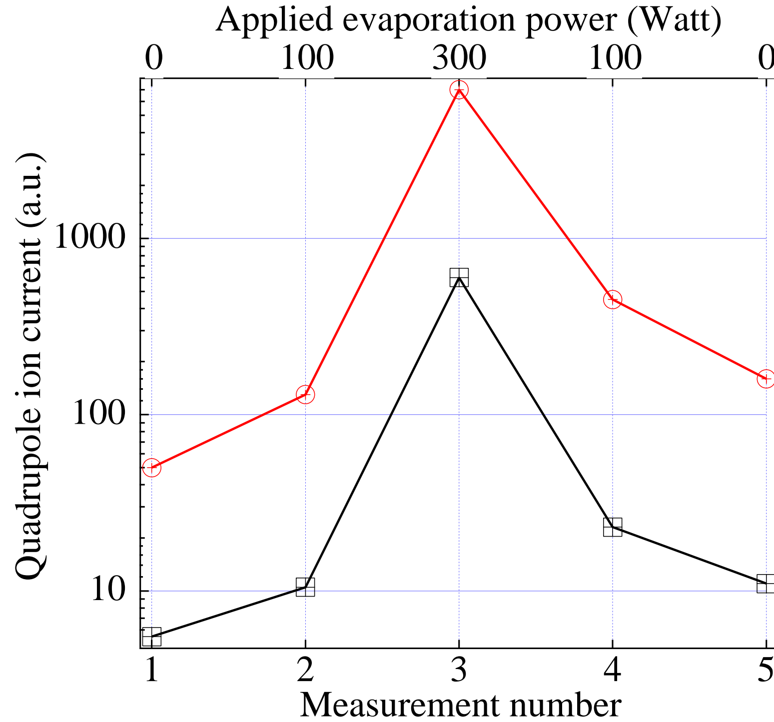

Figure 3.9: Quadrupole mass spectrometry measurement of relative Carbon count rates as a function of evaporation rate. Dots and squares denote 12 and 6 amu counts, respectively.

films of similar thicknesses grown in the Paderborn group.

At first glance this is not very surprising, taking into account only X–ray specific considerations. Carbon substitutes Nitrogen, and both atoms differ electronically only by one electron. X–rays however are sensitive to electron densities, therefore basically no contrast between doped an undoped material should be expected.

Taking the argument even further, it can be inferred that Carbon does not induce or promote the formation of defects which might show up in X–ray rocking curves, or perhaps degrade the phase purity, since these X–ray scans do not show any noticeable changes. That is a remarkable difference from the behaviour of Magnesium as reported elsewhere [126, 127].

AFM Results

In the same vein, measurements of the surface topology do not show any influence of the presence of Carbon on the GaN growth front. It can be seen from figure 3.11 that on larger scales ($(100\mu\text{m})^2$) as well as on smaller scales of $(10\mu\text{m})^2$ the surface structure remains basically unchanged with respect to undoped GaN samples. The surface roughnesses, measured to rms=8.4 nm, is comparable to earlier results [62, 63]. Therefore it appears possible to conclude that Carbon does not act for example as an antisurfactant, roughening the surface by means of reducing the adatom surface

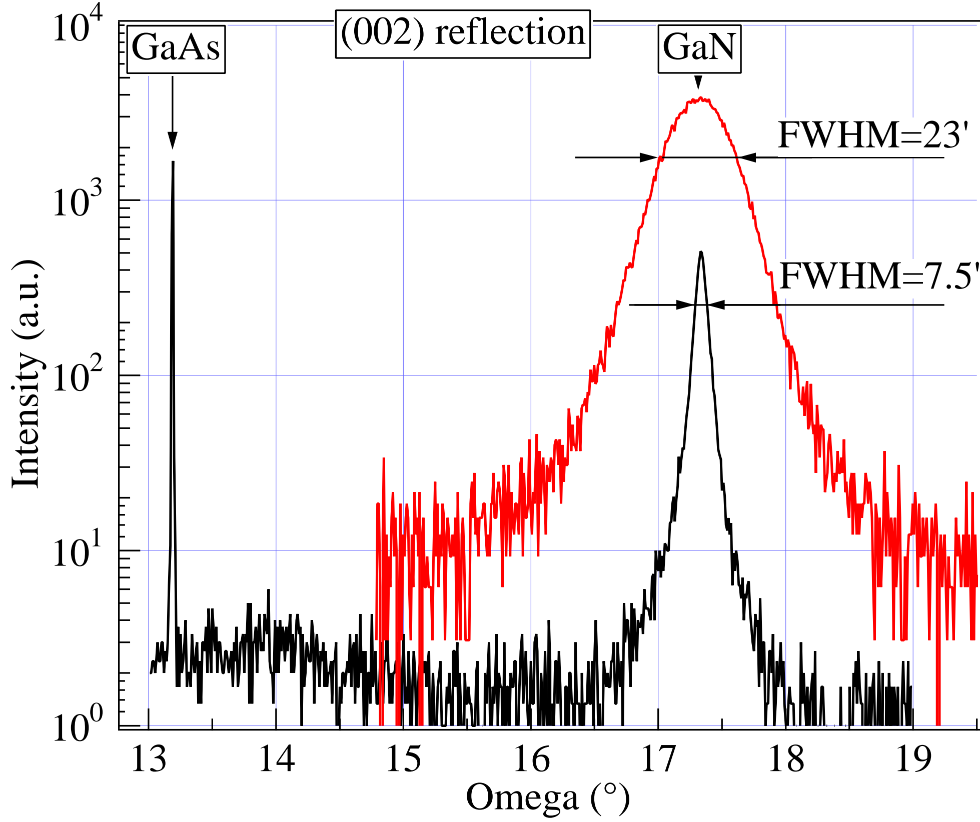

Figure 3.10: $\omega - 2\theta$ and ω (upper curve) scans of the (002) reflex of a Carbon doped c–GaN sample, with 650nm sample thickness.

mobility or surface kinetics in general, or otherwise influencing the growth process.

Carbon Incorporation

In analogy to equation (3.4), the amount of Carbon incorporation into Gallium Nitride can be calculated via

$$\frac{F_C}{F_{Ga}} = \frac{N_C^{GaN}}{N_{Ga}^{GaN}}, \tag{3.6}$$

since GaN growth proceeds in a controlled stoichiometric manner. $N_{Ga}^{GaN} = \frac{4}{a_0^3} = 4.332 \cdot 10^{22} cm^{-3}$, and the Ga flux $F_{Ga} \approx 1.5 \cdot 10^{14} cm^{-2} s^{-1}$. The Gallium flux needs to be corrected with respect to the Ga sticking coefficient, which was determined as $s_{Ga} = 0.5$ at the GaN growth temperature [63]. In cooperation with Justus Liebig University Gießen SIMS measurements were conducted in order to determine the absolute Carbon content. The measurements showed a Carbon concentration of $N_C \approx 2 \cdot 10^{20} cm^{-3}$ for a Carbon flux $F_C = 1 \cdot 10^{12} cm^{-2} s^{-1}$ [124, 128, 129]. This is in excellent agreement with the aforementioned relation (3.6).

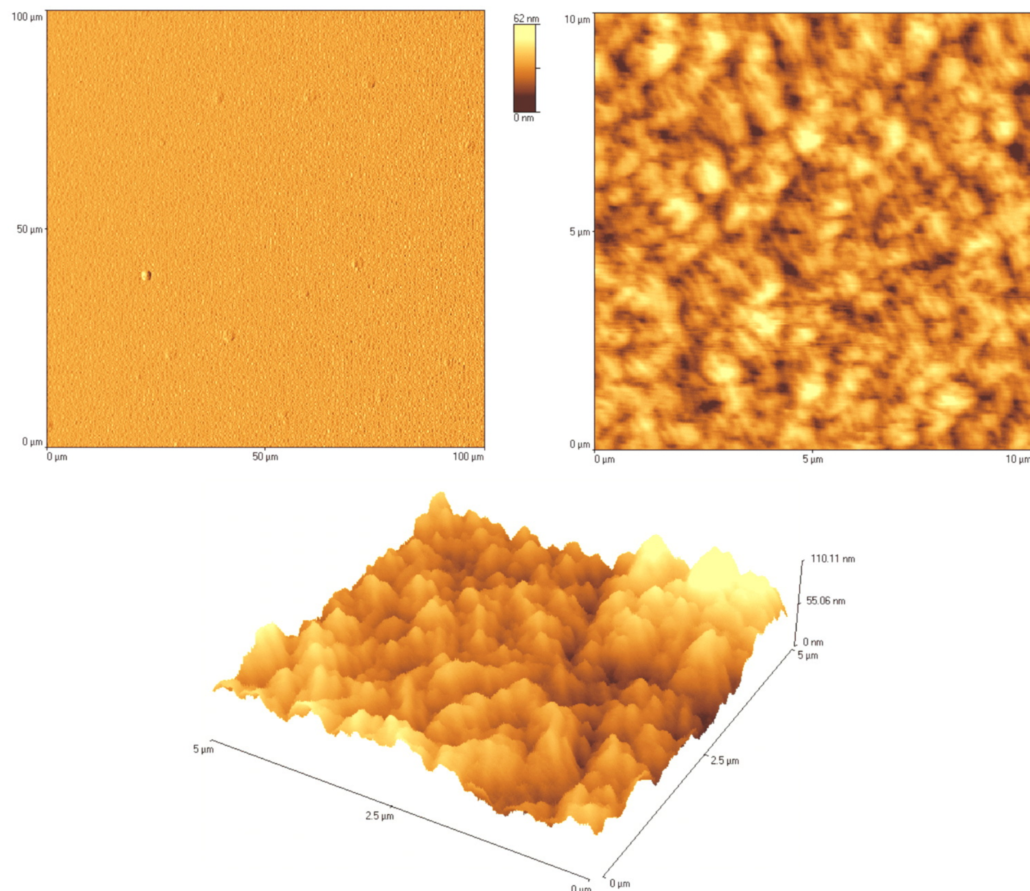

Figure 3.11: Representation of AFM images recorded on lateral scales of $(100\mu\text{m})^2$, $(10\mu\text{m})^2$, and $(5\mu\text{m})^2$ (threedimensional image), respectively.

3.3.2 Photoluminescence

Influence of Carbon Flux

As can readily be seen in figure 3.12, the incorporation of Carbon into c–GaN manifests itself in a profound change of the optical properties. It is apparent that the two different features which will be discussed in the following point to vastly different processes. In undoped GaN, the most promiment low–temperature PL features are the band edge luminescence, in this case the bound exciton luminescence (X) at $E = 3.27eV$ and the donor–acceptor pair transition (D^0, A^0) at $E = 3.16eV$ [130].

With increasing Carbon flux during GaN growth, an additional line evolves around $E = 3.08eV$. At the highest fluxes demonstrated here, $F_C = 4 \cdot 10^{11} cm^{-2} s^{-1}$, a deep luminescence centered around $E = 2eV$ evolves. This orange luminescence is the optical footprint of Carbon–related centers which act as bypasses of the near edge luminescence, effectively quenching all band edge luminescence for those high Carbon fluxes. Due to Fabry–Perot thin film interference fringes it was not possible to positively conclude whether the deep luminescence consists of one extremely broad emission or rather several different recombination paths. At even higher Carbon concentrations

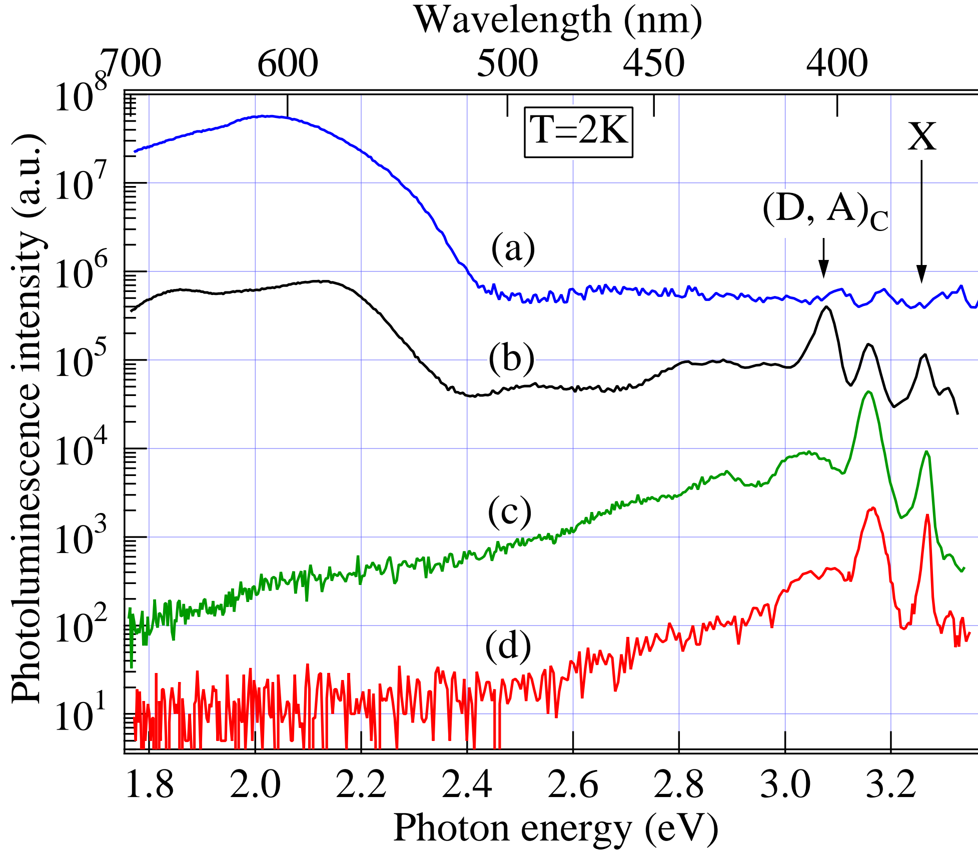

Figure 3.12: Photoluminescence spectra, taken at $T = 2K$, of c–GaN samples doped with Carbon; (a) $F_C = 4 \cdot 10^{11} cm^{-2}s^{-1}$, (b) $F_C = 8 \cdot 10^{10} cm^{-2}s^{-1}$, (c) $F_C = 5 \cdot 10^{8} cm^{-2}s^{-1}$, (d) nominally undoped. The spectra are offset to each other for reasons of better clarity.

of about $N_C \approx 2 \cdot 10^{20} cm^{-3}$ no PL can be detected at all. For moderate Carbon incorporations, exemplified by spectrum (b) of figure 3.12, an additional line evolves near the gap, eventually dominating the near band edge luminescence. A more detailed analysis of this peak shows that it actually consists of two distinct lines separated by 28meV. The variation of the Carbon–related near band edge luminescence as a function of Carbon incorporation is depicted in figure 3.13, where the integrated intensity of the $3.08eV$ luminescence is plotted as a function of Carbon flux. On the other hand, however, it can be seen (cf. fig. 3.14) that despite the overall quenching of the near–edge luminescence the Carbon related line still gains in relative intensity, compared to the exciton and (D^0, A^0) transitions. As will be discussed later, this is an indication that even at those high Carbon fluxes Carbon is still incorporated as an electrically active acceptor, i.e., on a Nitrogen lattice site.

In conclusion it can be inferrred that the Carbon–related defect causing the orange luminescence is at the same time both responsible for the quenching of the near–edge PL *and* unrelated to the C_N acceptor.

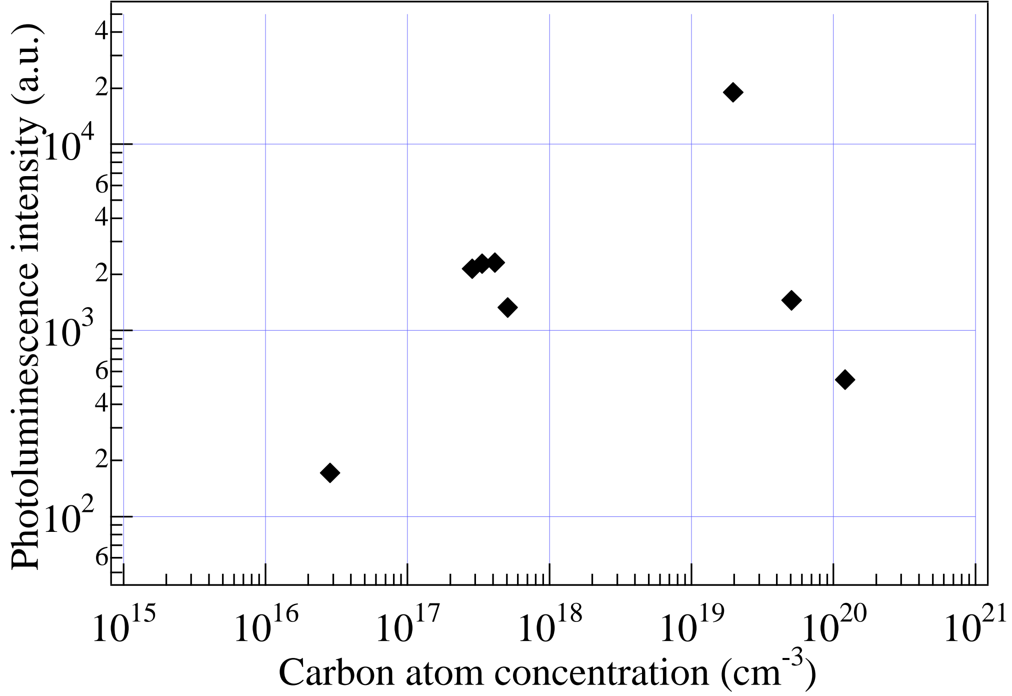

Figure 3.13: Integrated intensity of Carbon–related near–edge photoluminescence of c–GaN layers, taken at T = 2K.

Temperature Dependent Measurements

Figure 3.15 shows an overview of the evolution of the c–GaN:C photoluminescence as a function of temperature. The sample in question was grown with a Carbon flux of $F_C = 1.5 \cdot 10^9 cm^{-2} s^{-1}$.
As already mentioned in the preceding paragraph, the C_N related PL transition is actually composed of two separate lines, which are especially emphasized in the graph. Those lines were fitted with two Gaussians. Upon increasing the temperature above $T = 120°C$, the lower–energy contribution cannot be observed.

The temperature–induced shift of the respective energetic positions, plus the change of the exciton transition energy, is shown in diagram 3.16. The dashed curve denotes the variation of the band gap,

$$E_g = E_0 - \alpha \cdot \frac{T^2}{T + \beta}, \tag{3.7}$$

as given in reference [131]. Here, $E_0 = 3.302eV$, $\alpha = 0.0006697eV/K$, and the Debye temperature $\beta = 600K$. The exciton binding energy could be estimated from the data points (circles); the second line follows the relation $E(T) = E_g(T) - E_B$. The fit yielded $E_B = 19meV$, and a localization energy $E_{B,X} = 15meV$ at $T = 2K$. The third line from top is a fit to the band–acceptor transition $(e, A^0)_C$, given by

$$E = E_g - E_A + \frac{1}{2} \cdot k_B \cdot T. \tag{3.8}$$

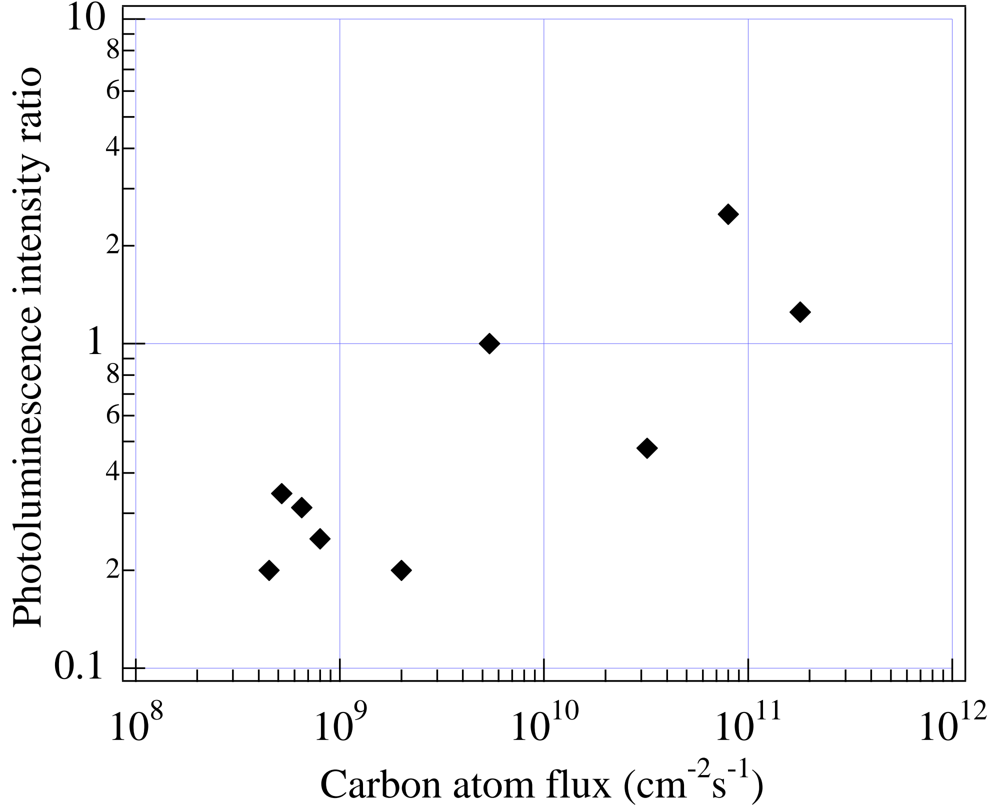

Figure 3.14: Ratio of Carbon–related integrated PL intensity to near–edge Photoluminescence of c–GaN layers doped with different Carbon concentrations, recorded at T = 2K.

Likewise, the donor–acceptor pair transition $(D^0, A^0)_C$ is fitted by

$$E = E_g - (E_A + E_D) + \frac{1}{2} \cdot k_B \cdot T. \qquad (3.9)$$

The agreement between fit and data points is excellent, lending confidence to the values shown in table 3.1.

E_B (exciton)	19meV
E_A (C_N)	215meV
E_D	28meV

Table 3.1: Summary of electrical data for the Carbon acceptor in c–GaN.

The donor energy of 28meV is the same as the one also observed in other, undoped, samples [130]. Most likely it can be attributed to Indium or Oxygen; however, Silicon is another possible candidate. The acceptor activation energy of 215meV is 15meV less than the corresponding value of the Magnesium acceptor in c–GaN [132], and also below the experimentally determined value in h–GaN [88].

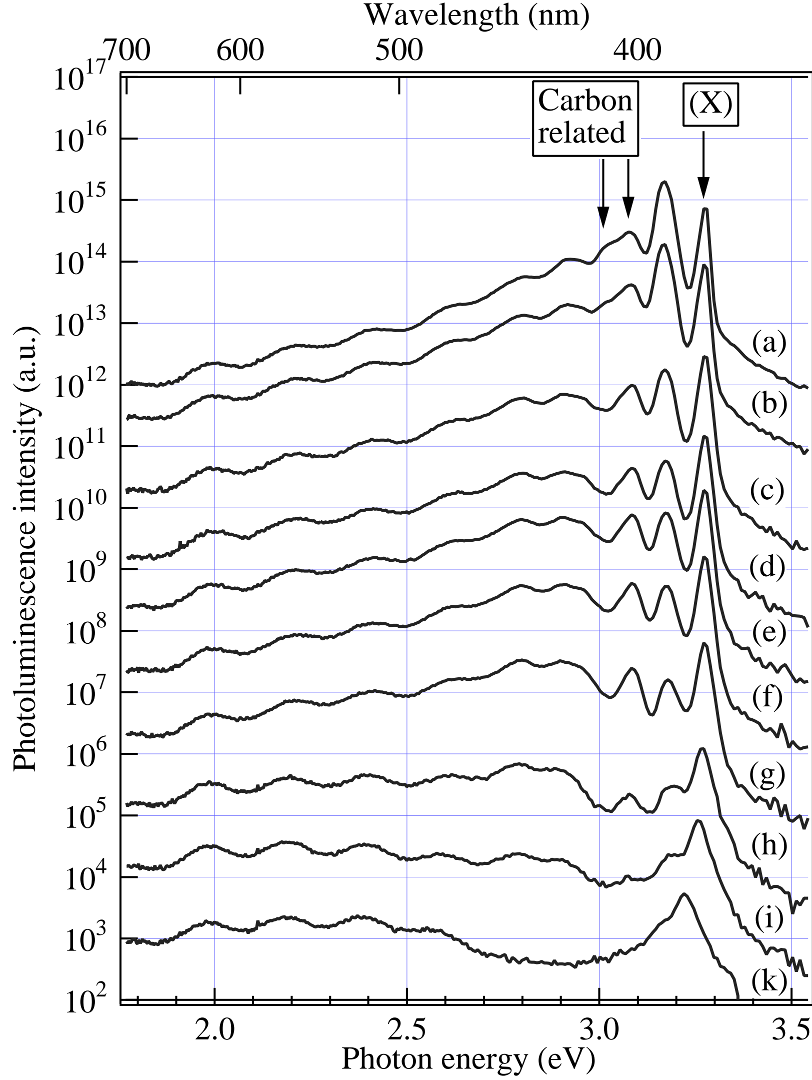

Figure 3.15: Photoluminescence spectra taken at different temperatures: (a) 2K, (b) 25K, (c) 40K, (d) 60K, (e) 80K, (f) 100K, (g) 120K, (h) 160K, (i) 200K, (k)=300K.

In contrast to the observations reported by Ogino *et al.* and Zhang *et al.*, the orange luminescence of the c–GaN:C samples could not be shown to observe a temperature-induced shift of the peak energy [96, 133]. This may be attributed to the rather broad character of this luminescence band, which is additionally convolved with thin film interference fringes. Because of this increased complexity, especially the possible involvement of several deep defects, it is hardly possible to infer an activation energy E_a. Fitting the temperature–dependent orange luminescence intensity using the relation

$$I(T) = \frac{I(0)}{1 + c \cdot \exp(-\frac{E_a}{k_B \cdot T})} \tag{3.10}$$

yields an activation energy $E_a \approx 25 - 30meV$. This is again in agreement with the

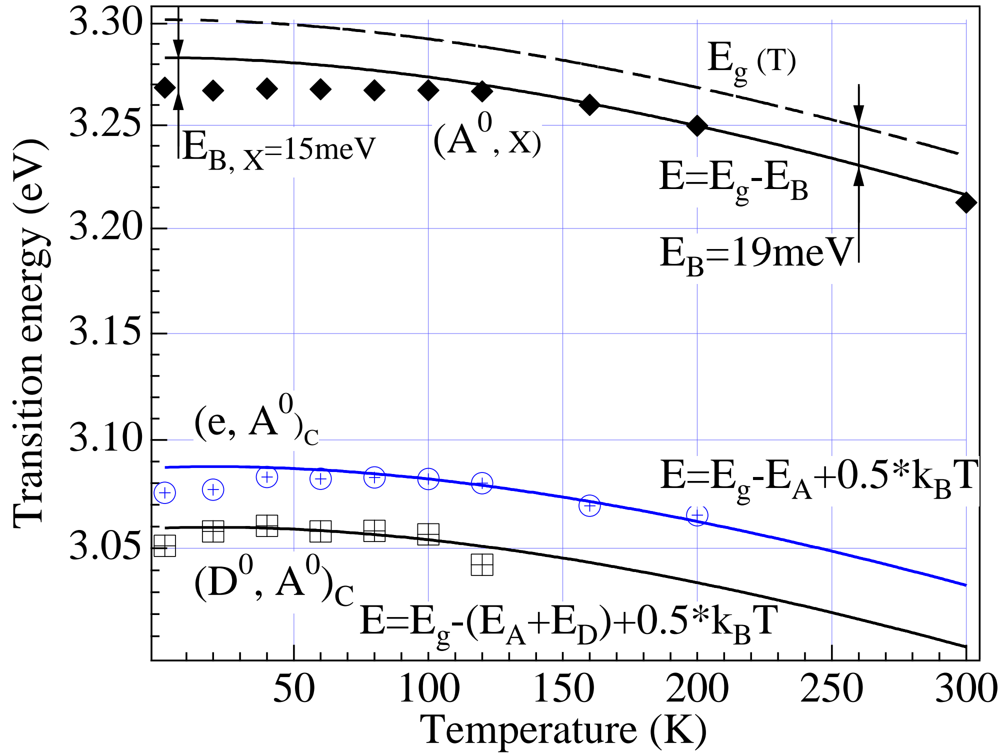

Figure 3.16: Observed temperature shift of near band edge PL transitions (circles: excitonic transition; squares: C–related band–acceptor transition, $(e, A^0)_C$; diamonds: C–related donor–acceptor transition, $(D^0, A^0)_C$).

ubiquitous shallow donor mentioned before, making the deep defect an acceptor. This is however quite possible; it mainly requires the shallowest of the several Carbon complexes predicted by Wright to be an acceptor [103]. Indeed, the C_I–V_{Ga} is calculated to be an acceptor with a transition around 2eV, and favoured by p–type growth conditions. Glaser *et al.* identify a deep Carbon related defect as an acceptor as well [134].

Excitation Dependent Measurements

Excitation–dependent PL measurements make the distinction between different kinds of recombination centers possible [135]. Diagram 3.17 shows the variation of the integrated intensity of the various PL transition lines as a function of the excitation power density at $T = 2K$. The laser intensity was attenuated by means of UV neutral density filters introduced into the laser beam. It can clearly be seen that the near band edge luminescence, i.e. exciton, DAP and Carbon related, follows the same power law $I \propto L^{1.2}$, which would be expected for delocalized states involved in near gap transitions. In contrast, the orange luminescence around 2eV obeys $I \propto L^{0.9}$. This points to a strong localization of the corresponding recombination center.

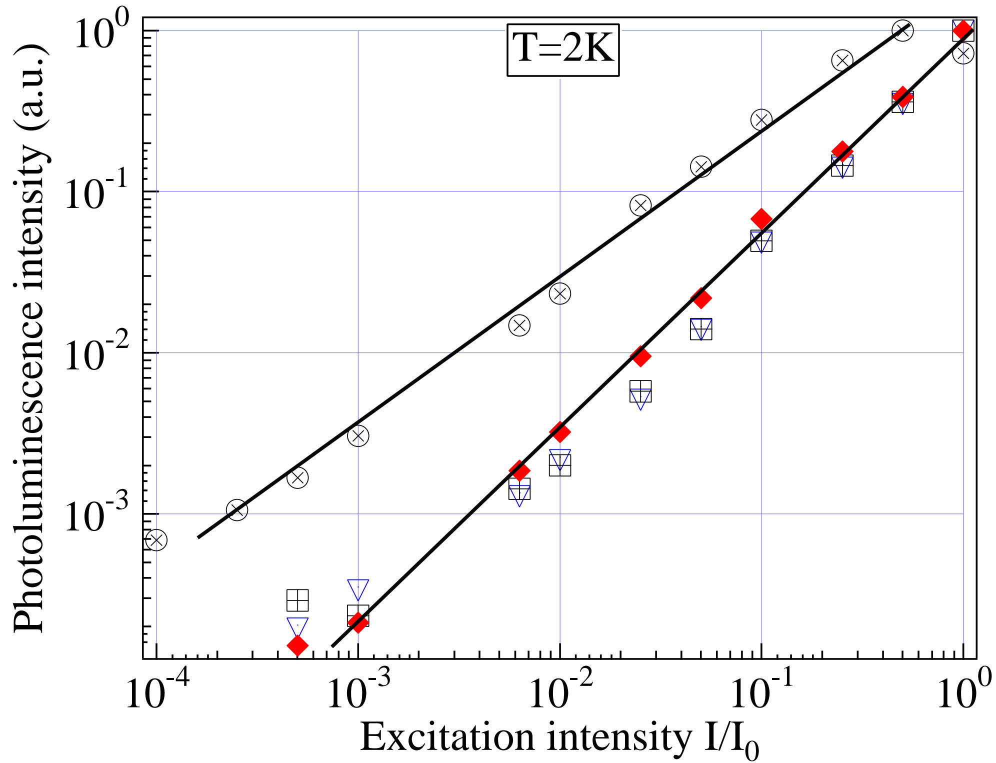

Figure 3.17: PL intensity of c–GaN:C as function of excitation intensity. Diamonds, squares and triangles mark near band edge luminescence, dots orange luminescence.

3.3.3 Electrical Properties

Flux Dependencies

Only electrical measurements are actual proof of carbon acting as an acceptor at all, a fact which was merely implicitly assumed in the preceding paragraphs. Graph 3.18 demonstrates the variation of GaN room temperature hole concentrations, determined by means of Hall effect measurements, as a function of Carbon flux. The data in figure 3.18 are organized as follows:

- diamonds correspond to values measured with “standard” samples of 1μm thickness with uniform doping, directly grown on semi–insulating GaAs substrates
- triangles correspond to Hall values measured with samples which were grown on top of a GaN template of known thickness and known electrical and optical properties

These data seem to point towards an increase in hole concentration due to an increase in acceptor concentration, followed by a steep decline in free carrier concentration.

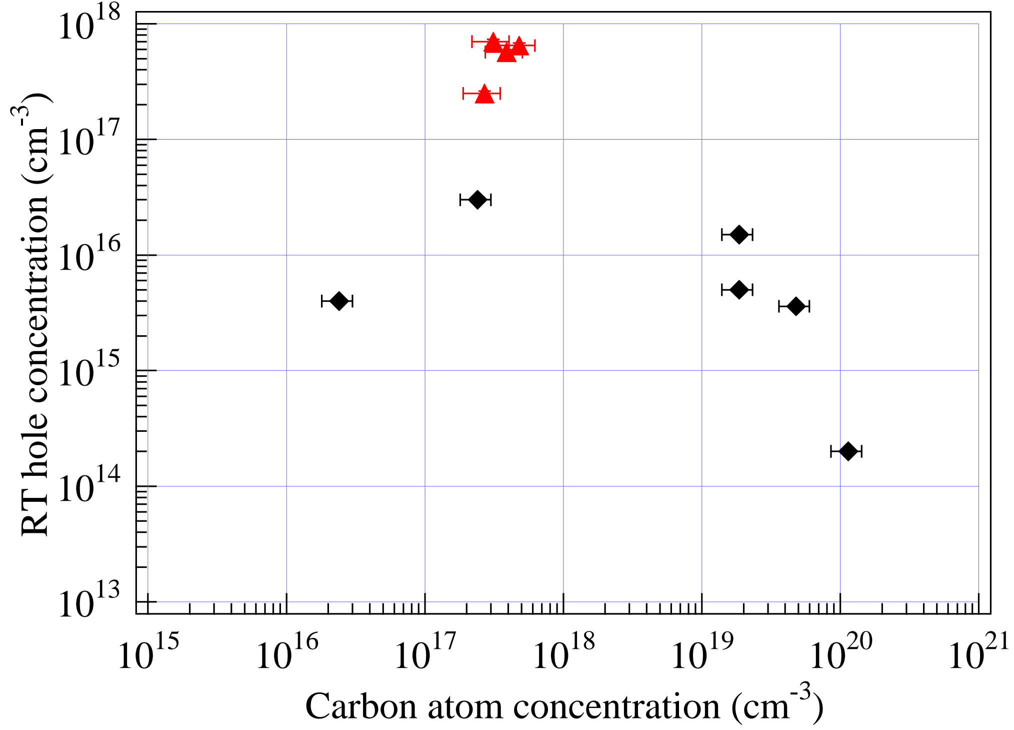

Figure 3.18: Room temperature Hall data over Carbon flux.

Rearranging equation (3.6),

$$N_C^{GaN} = \frac{F_C}{F_{Ga}} \cdot N_{Ga}^{GaN}. \tag{3.11}$$

Therefore the rising slope of hole concentrations *vs.* Carbon flux makes complete sense. The fact that there is an apparent maximum in RT hole concentration may be explained by drawing again from similar semiconductors, GaAs in this case. In this system self–compensation has been reported for high Carbon concentrations [118], caused by Carbon complexes in the form of split–interstitials [120].

Wright published calculations concerning different Carbon defects in hexagonal phase material [103]. He concluded that C_N acts as a shallow acceptor, C_{Ga} as a deep donor. Interstitial Carbon was predicted to be a quadruple donor in p–type material and a deep acceptor in n–type GaN with a formation energy lower than that of C_N, while a complex C_I—C_N would form a donor with multiplicity 3. Although these results were calculated only for h–GaN, it should be possible to transfer them to a first approximation to c–GaN, for reasons outlined above. Kaufmann *et al.* considered a model to describe the self–compensation upon Magnesium doping of h–GaN [89].

The hole concentration of a lightly compensated semiconductor can be described by [58, 59]

$$p = -\frac{N_D + K}{2} + \sqrt{\left(\frac{N_D + K}{2}\right)^2 + K \cdot (N_A - N_D)}, \tag{3.12}$$

where N_A and N_D denote acceptor and donor concentration, respectively. K is defined as

$$K = \frac{1}{\beta} \cdot N_V \cdot \exp\left(-\frac{E_A}{k_B \cdot T}\right). \qquad (3.13)$$

β, E_A, k_B, T, and N_V carry their usual meaning (cf. page 25). Obviously, the relation (3.12) with a constant number of monovalent donors cannot give a satisfying fit to the data shown above (cf. fig. 3.18).
Earlier it was noted that in addition to a shallow acceptor Carbon might also form Carbon–Carbon complexes or interstitials. Interstitial Carbon was predicted to be a multiple donor, with multiplicity m=4, while the complex C_I—C_N formed a triple donor, m=3. The formation energy of the former $E_f = 1.76eV + q \cdot E_F$, and of the latter $E_f = 2.65eV + q \cdot E_F$ [103].
Because of the charge $q = 4$ in the case of the Carbon interstitial the self–compensation ratio

$$r_{C_I} = \frac{4 \cdot N_D}{N_A - N_D}, \qquad (3.14)$$

while the dicarbon self–compensation ratio

$$r_{C_I - C_N} = \frac{3 \cdot N_D}{N_A - 2 \cdot N_D}. \qquad (3.15)$$

With the definition of a self–compensation coefficient

$$c = \frac{N_D}{N_A} \qquad (3.16)$$

$r_{C_I} = 4 \cdot \frac{c}{1-c}$ and $r_{C_I - C_N} = 3 \cdot \frac{c}{1 - 2 \cdot c}$. Complete compensation in both cases is given by $r = 1$ and $c = 1/5$, respectively. With those definitions, $N_D = q \cdot c \cdot N_A$ and equation (3.12) can be rewritten as

$$p = -\frac{q \cdot c \cdot N_A + K}{2} + \sqrt{\left(\frac{q \cdot c \cdot N_A + K}{2}\right)^2 + K \cdot N_A \cdot (1 - q \cdot c)}. \qquad (3.17)$$

The compensating donors are probably formed during growth at elevated temperatures, $T \approx 1000K$, and their concentration will likely not change dramatically during the rapid cool down to ambient temperature. Therefore the number of donors is given by

$$N_D = \frac{N_{sites}}{2} \cdot \exp\left(\frac{S}{k_B}\right) \cdot \exp\left(-\frac{E_f}{k_B \cdot T}\right), \qquad (3.18)$$

where the number of available sites is given by N_{sites}, and S and E_f describe the defect formation enthalpy and energy, respectively. As mentioned above, E_f satisfies a general form $E_f = E^0 + q \cdot E_F$, with donor charge q and Fermi level E_F. Thus

$$N_D = A_q \cdot \exp\left(-\frac{q \cdot E_F}{k_B \cdot T}\right) \qquad (3.19)$$

where

$$A_q = \frac{N_{sites}}{2} \cdot \exp\left(\frac{S}{k_B}\right) \cdot \exp\left(-\frac{E^0}{k_B \cdot T}\right). \tag{3.20}$$

The position of the Fermi level can be calculated as

$$\begin{aligned} E_F = &-k_B \cdot T \cdot \ln(2 \cdot \beta \cdot (N_A - N_D) \cdot (\beta \cdot N_V + N_D \cdot \exp(\epsilon_A) \\ &+ \sqrt{(\beta \cdot N_V + N_D \cdot \exp(\epsilon_A))^2 + 4 \cdot \beta \cdot N_V \cdot (N_A - N_D) \cdot \exp(\epsilon_A)})^{-1}). \end{aligned} \tag{3.21}$$

using the convention $\epsilon_A = E_A/(k_B T)$.

With $\alpha = 4 \cdot \beta \cdot \exp(\epsilon_A)$ and assuming only a negligible residual donor concentration, i.e. , $N_D = 0$, this expression can be greatly simplified to

$$E_F = k_B \cdot T \cdot \ln\left(\frac{N_V}{2 \cdot N_A} \cdot \left[1 + \sqrt{1 + \alpha \cdot \frac{N_A}{N_V}}\right]\right). \tag{3.22}$$

Inserting eq. (3.22) in eq. (3.19) one gets the following expression:

$$N_{C_I} = A_q \left(\frac{N_V}{2 \cdot N_A}\right)^{-q} \cdot \left[1 + \sqrt{1 + \alpha \cdot \frac{N_A}{N_V}}\right]^{-q} \tag{3.23}$$

and eventually

$$c = \frac{2 \cdot A_q}{N_V} \cdot \left(\frac{2 \cdot N_A}{N_V}\right)^{q-1} \cdot \left[1 + \sqrt{1 + \alpha \cdot \frac{N_A}{N_V}}\right]^{-q}. \tag{3.24}$$

As already mentioned above, the case of complete compensation is defined as $r = 1$, i.e., $c = 1/5$. This can be used in order to normalize the expression (3.24) by setting $N_A = N_{comp}$, finally yielding

$$c = \frac{1}{5} \cdot \left(\frac{N_A}{N_{comp}}\right)^{q-1} \cdot \left[\frac{1 + \sqrt{1 + \alpha \cdot \frac{N_{comp}}{N_V}}}{1 + \sqrt{1 + \alpha \cdot \frac{N_A}{N_V}}}\right]^q. \tag{3.25}$$

This is a general expression for both kinds of compensating donors discussed here. When inserting equation (3.25) in eq. (3.17), care has to be taken that the compensation coefficients c are actually calculated for growth temperatures, yet equation (3.17) needs to be calculated for room temperatures. In the same vein, $q = 4$ for Carbon interstitials and $q = 3$ for $C_I - C_N$ complexes.

The respective results can be seen in figure 3.19. The through lines correspond to the Carbon interstitial as the compensating species ($q = 4$), while the dashed lines result from fitting with the dicarbon complex, $q = 3$. The top two lines are fit results with hole masses held at $m_h^* = 0.75 m_e$. Both models require acceptor activation energies on the order of $E_A = 180 meV$. In this case, the upper dashed line yields a better fit, with a density of compensating donors of $N_{comp} = 5.2 \cdot 10^{19} cm^{-3}$. In contrast, for the

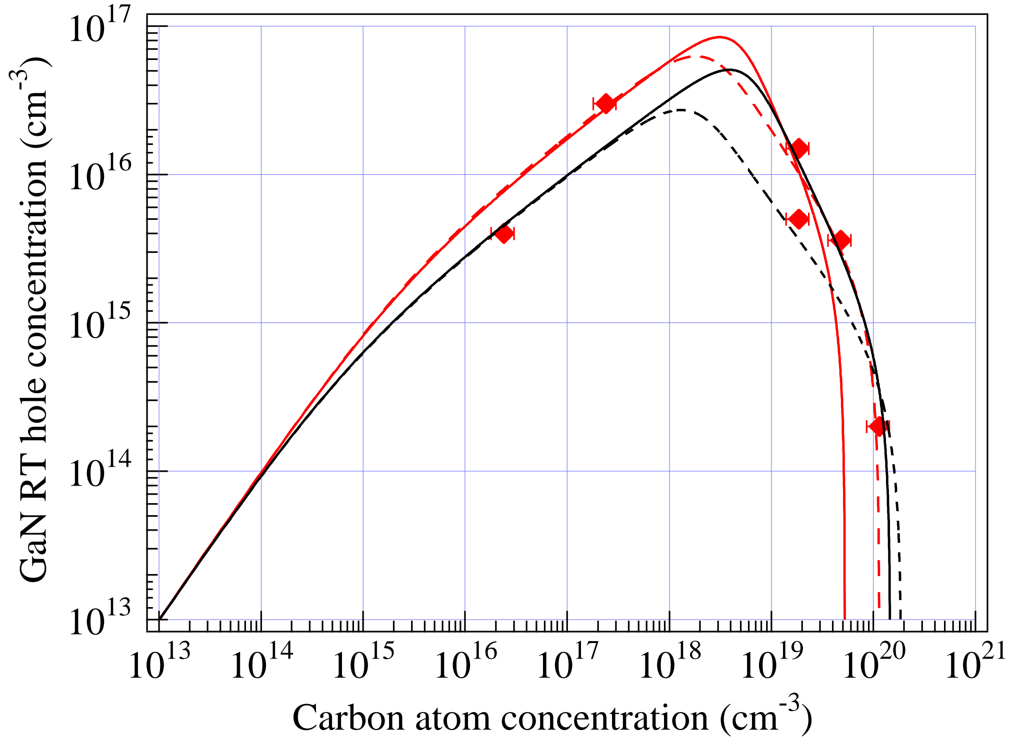

Figure 3.19: Room temperature Hall data over Carbon flux compared with model data. Full lines denote fits modelling the $C_{\mathbf{I}}$, dashed lines the $C_{\mathbf{I}}$–$C_{\mathbf{N}}$ as compensating complex. The models differ further in the activation energies and hole masses, as described in the text.

C_I model $N_{comp} = 4.4 \cdot 10^{19} cm^{-3}$.
Relying on the data from temperature–dependent PL and Hall measurements as shown in tables 3.1 and 3.2 however, i.e. using $E_A = 215meV$ and of $m_h^* = 0.8m_e$ [132], the bottom two curves show an excellent agreement between experimental data and the Carbon interstitial model, with a compensating density of $N_{comp} = 1.2 \cdot 10^{20} cm^{-3}$. Here the C_I–C_N complex falls flat with lower compensation densities of $N_{comp} = 8 \cdot 10^{19} cm^{-3}$.

Obviously these results so far are not fully conclusive. In particular it seems remarkable that for lower hole masses (top curves) the dicarbon complex fits the experimental results better than the Carbon interstitial, while for higher effective hole masses the C_I impurity offers a better model. Therefore an independent determination of the hole mass appears necessary, considering the sensitivity of the model results. Alternatively, a larger number of experimental data epecially at Carbon concentrations around $N_C \approx 10^{17} cm^{-3}$ might serve this purpose.

Further discussion of the Carbon flux dependent RT Hall data shall be deferred to a later section.

Temperature Dependent Hall Measurements

Measuring the Hall coefficient at variable temperatures of course is another way to determine the thermal activation energy of the Carbon acceptor. Figure 3.20 shows an Arrhenius plot of the Hall coefficient of a moderately C–doped c–GaN sample. For higher temperatures, $T = 400–220K$, the sample exhibits clear p–type conductivity and a freezing–out of the carriers. The slope of the Hall coefficient can be used to fit the general eq. (3.12), yielding the values of table 3.2. At low temperatures however the the sign of the Hall coefficient reverses, indicating the change of the carrier type to n–type. This agrees with the assumption of a shallow residual donor.

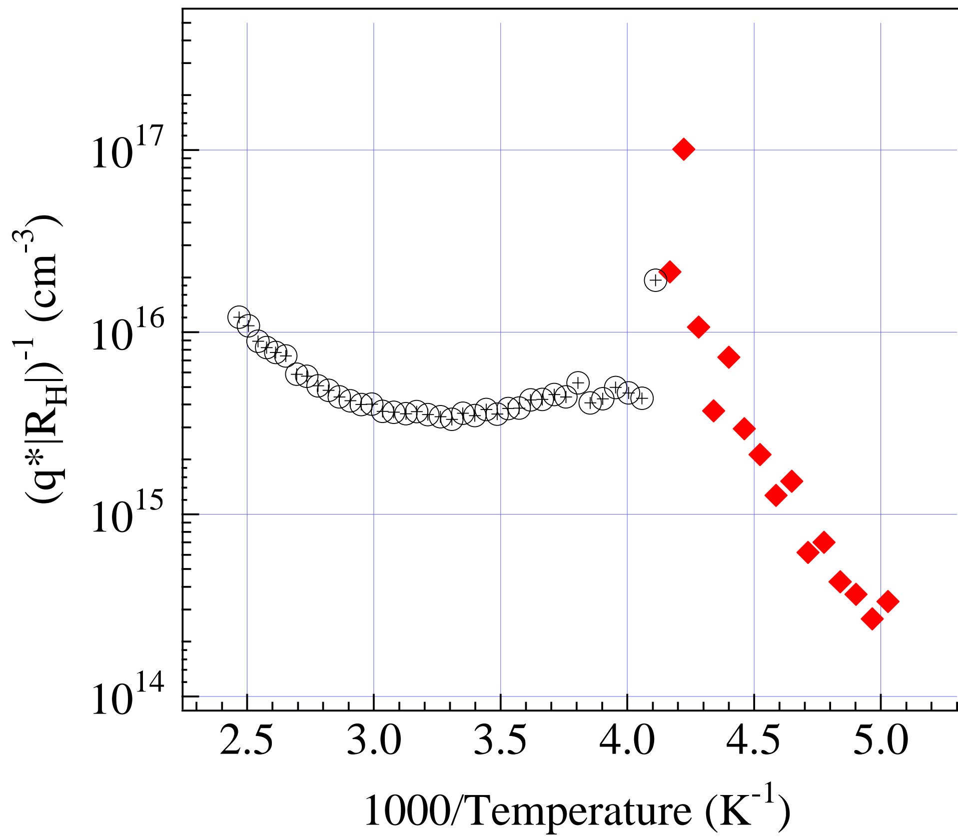

Figure 3.20: Arrhenius plot of the Hall coefficient as function of temperature.

E_A (C_N)	$205meV$
N_A (C_N)	$7.5 \cdot 10^{17} cm^{-3}$
N_D	$4.5 \cdot 10^{17} cm^{-3}$

Table 3.2: Summary of electrical data for the Carbon acceptor in c–GaN.

3.4 Discussion

Successful incorporation of Carbon in cubic Gallium Nitride could be demonstrated with the help of SIMS measurements, in a quantity that agrees with separate calibration runs [124]. Moreover, Carbon acts benignly during MBE growth, it does not induce excessive surface roughness or decrease c–GaN bulk structural order, which should show up through X–ray measurements.

As has been shown above, the incorporation of Carbon into c–GaN leads to two different aspects which can be observed in photoluminescence.
First, a shallow defect is introduced, the optical footprint of which increases proportionally to the Carbon flux during growth. This defect can be described with an activation energy $E_A = 215meV$. The defect line actually consists of two distinct transitions, separated by 28meV. The lower of the two cannot be observed at temperatures above $T = 120K$. This is typical for donor–acceptor pair transitions, where the shallower of both defects thermalizes into the corresponding band. Since the 28meV agree with a shallow donor found in earlier cubic Gallium Nitride samples, this would make the shallow defect a donor.
Second, Carbon incorporation introduces one or more deep defects which cause optical transitions at energies of about 2eV. This optical transition is predominant in samples with very high Carbon fluxes and eventually quenches the near band edge luminescence. These transitions may possibly be composed of several lines that could not be distinguished in this work. Several authors report deep luminescence connected with Carbon–related deep defects as well [96, 133, 134, 136].

However, the two mechanisms — formation of a shallow acceptor and of a deep defect — are not obviously connected with each other. This can be inferred from a comparison of figures 3.14 and 3.13: the Carbon–related transition at $3.08eV$ still gains intensity relative to the other near band edge emission lines (fig. 3.14), while the overall intensity of the near edge optical transitions decreases due to the increasing influence of the alternative recombination path connected with the deep defect.

Hall effect measurements exhibit the same phenomenology. With increasing Carbon concentration the hole concentration increases. The acceptor introduced by Carbon doping is characterized by a thermal activation energy of $E_A = 205meV$. At high Carbon fluxes, however, this acceptor is strongly compensated. Literature suggests several possible compensating defects, all due to Carbon incorporation [103]. A model calculation tentatively points towards Carbon interstitials being the deep donor in question, as this defect acts as a quadruple donor — where multiple donors are necessary to achieve near complete compensation —, and has a low formation energy in p–type GaN. The Carbon concentration necessary to achieve compensation is $N_{comp} = 1.2 \cdot 10^{20} cm^{-3}$.

A comparison of PL and Hall results allows one to finally conlude that the defects observed through optical and electrical measurements are identical, i.e.

- the shallow defect observed in PL is identical to the acceptor determined through electrical measurements, its activation energy being $E_A = 205 - 215meV$,
- the deep defect causing orange luminescence is related to a Carbon interstitial, acting as a multiple–valent deep defect.

Therefore, both hole concentration and photoluminescence intensity follow the model given by equations (3.17) and (3.25).

The validity of these conclusions is strongly supported by diagram 3.21. The line corresponds to eq. (3.17) using the appropriate Carbon interstitial self–compensation coefficient c, $m_h^* = 0.8m_e$ $E_A = 215meV$, and $N_{comp} = 1.2 \cdot 10^{20}cm^{-3}$. Clearly this model explains the observations satisfactorily.

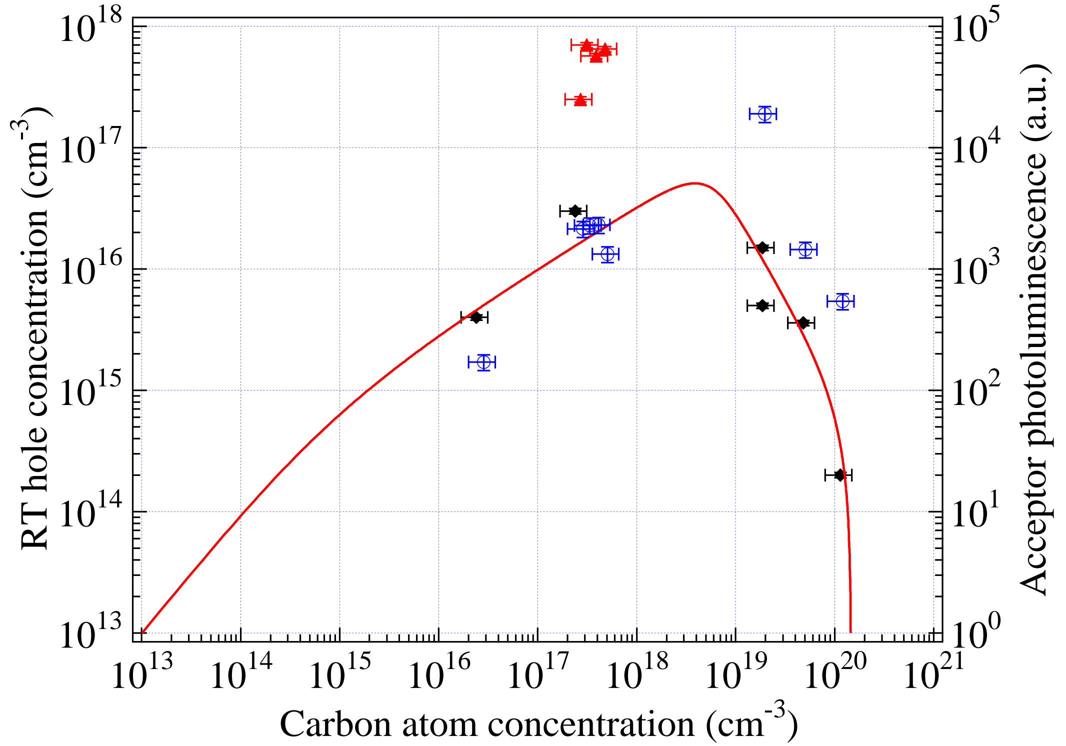

Figure 3.21: Room temperature hole concentrations (diamonds, left ordinate) and 2K near edge photoluminescence intensity (open circles, right ordinate) as a function of Carbon flux.

Most remarkably, the Carbon doping demonstrated here does not suffer from the drawback usually reported with respect to Mg–doping of hexagonal phase GaN: low hole mobilities. Usually, hole mobilities in h–GaN:Mg are of the order $\approx 10cm^2/(Vs)$, whereas the samples grown in the course of this work exhibited mobilities around $200cm^2/(Vs)$. In this regard it is important to note that only the product of carrier concentration and mobility is of importance to actual devices.

The only remaining problem is the measurement of very high room temperature hole concentrations for a set of four samples, shown as triangles in figures 3.18 and 3.21. However similar observations have indeed been reported in the available literature [137, 138]. It was reported that the addition of small quantities of the donor dopants Oxygen or Silicon will decrease the total energy of the GaN crystal, thus allowing higher doping efficiencies through effectively decreasing the acceptor activation energy.

The samples in question were the only samples grown on an underlying GaN template

wafer. This undoped GaN quasi–substrate was well characterized optically and electrically before it was re–introduced in the MBE system for regrowth of GaN:C. Obviously there is a chance that the atmospheric oxide was not completely removed, and Oxygen was carried with the GaN growth front, in this way achieving the co–doping.

In conclusion, the doping of c–GaN with Carbon was demonstrated. High hole concentrations of $N_A = 7 \cdot 10^{17} cm^{-3}$ could be achieved, at high carrier mobilities of $\mu = 200 cm^2/(Vs)$. The carbon acceptor possesses an activation energy $E_A = 215 meV$. At high Carbon concentrations however self–compensation sets in by means of a Carbon interstitial.

Chapter 4

AlN and AlGaN based Structures

4.1 Cubic AlN

The mastery of cubic Aluminum Nitride is not a matter of course, as is evident from the broad range of experimental values e.g. for band gap energy and lattice constant listed in table 4.1. Nakadaira *et al.* extrapolated the cubic AlN band gap as $E_g = 5.05eV$ from $Al_xGa_{1-x}N$ PL peak energies [139]. Sherwin *et al.* estimated the lattice constant $a_0 = \sqrt{3}/2c = 4.38$Åfrom wurtzite phase material data [141], while Okumura *et al.* calculated $a_0 = 4.3996$Å using the h–AlN bond length of 1.9051Å [74].

E_g (eV)	5.9	4.79		5.0	5.34
a_0 (Å)	4.4	4.4	4.373		
references	[74]	[140]	[142]	[143]	[144]

Table 4.1: Summary of published experimental values of c–AlN lattice constant and band gap energy.

Cubic Aluminum Nitride and Aluminum Gallium Nitride samples were grown in the scope of this work. The growth process was conducted on cubic GaN template layers and on GaAs substrates. The Aluminum flux was determined by observing GaAs and AlGaAs RHEED oscillations [64].

4.1.1 Growth of c–AlN

The growth process of cubic AlN was conducted at the usual c–GaN growth temperature of $T_{sub} = 720°C$ [62, 82, 90]. The Aluminum sticking coefficient was determined to be twice as high as the Gallium sticking coefficient at the same temperature.

In order to grow c–AlN layers on GaAs substrates, it appears highly advisable to start with a low–temperature buffer layer, similarly to the procedure for Gallium Nitride (see references above and section 2.3). At the nucleation temperature of $T_{sub} = 600°C$ the metal sticking coefficients are unity, therefore the Al flux was chosen equal to that of Gallium under the same conditions. Likewise, the Nitrogen BEP and nucleation time were not varied from the GaN case. This nucleation procedure was followed by

the growth of an c–AlN epilayer at $T_{sub} = 720°C$. The growth stoichiometry was adjusted by means of controlling the transition between the c(2x2) and (2x2) surface reconstruction. Picture 4.1 demonstrates the quality of the AlN growth process by means of a streaky RHEED pattern, recorded after two hours of c–AlN growth at $T_{sub} = 720°C$.

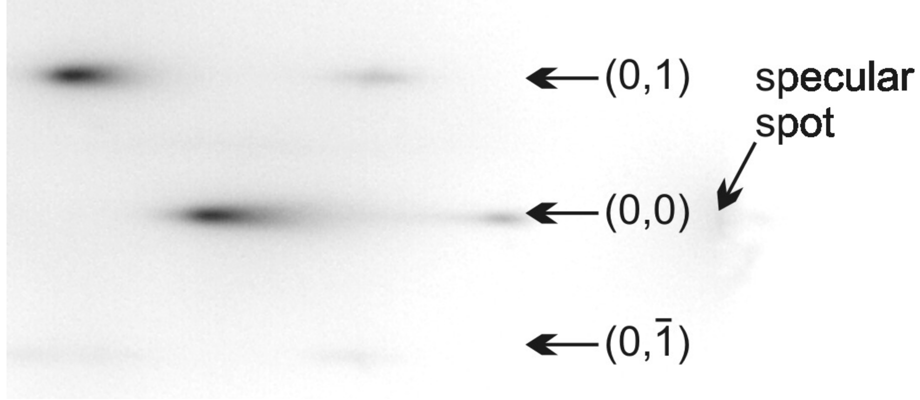

Figure 4.1: RHEED image of an AlN sample in [$\bar{\mathbf{1}}\mathbf{10}$] azimuth.

4.1.2 Structural Properties of c–AlN

A reciprocal space map around the ($\bar{1}\bar{1}3$) reflexes of cubic Aluminum Nitride ($q_{||} = -2.029Å^{-1}$, $q_{\perp} = 4.304Å^{-1}$) and Gallium Nitride ($q_{||} = -1.966Å^{-1}$, $q_{\perp} = 4.17Å^{-1}$) is shown in figure 4.2. This particular c–AlN film, with a thickness of 350nm, was grown on top of a 550nm thick c–GaN epilayer. The position of the c–AlN reflex in reciprocal space is certain proof that the Aluminum Nitride is completely relaxed.

4.1.3 Further Characterization

It is worthwhile noting that the c–AlN samples discussed here — both grown on c–GaN template layers and directly nucleated on GaAs substrate — exhibit p–type conductivity. In the case of growth on GaN films it may be argued that this is a result of a two–layer conduction mechanism comparable for example to the one discussed in reference [60], where both c–GaN and c–AlN layer conductivities are measured (in van der Pauw geometry!). However, this can positively be excluded for the direct growth on semi–insulating GaAs(001) substrate. Interestingly, the hole mobility values are very high and comparable to their GaN counterparts, as can be seen in table (4.2).

growth mode	carrier concentration	carrier mobility
direct AlN nucleation on GaAs	$p = 5.2 \cdot 10^{17} cm^{-3}$	$197 cm^2 (Vs)^{-1}$
on c–GaN template layer	$p = 7 \cdot 10^{15} cm^{-3}$	$177 cm^2 (Vs)^{-1}$

Table 4.2: Summary of electrical data for cubic AlN.

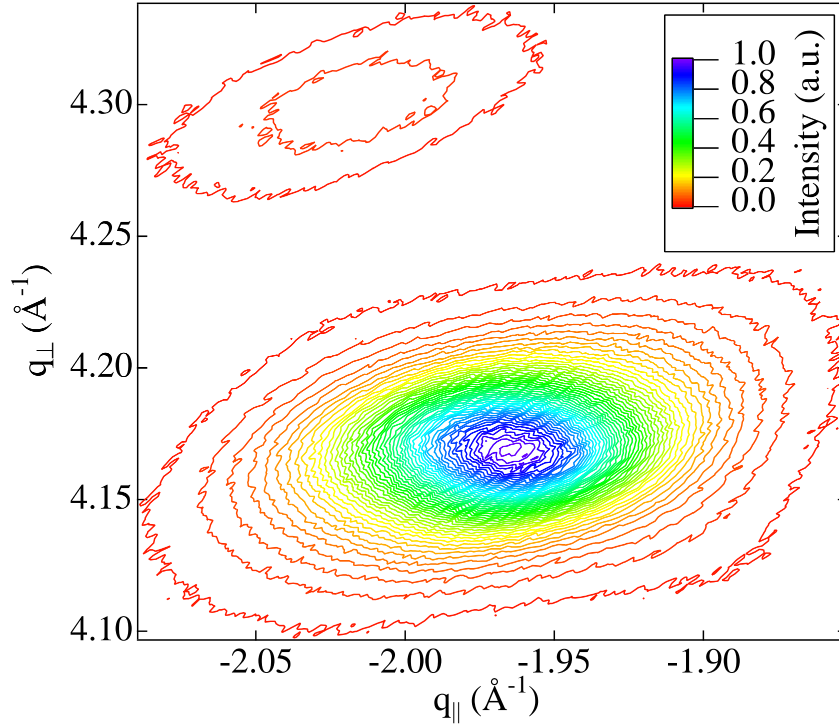

Figure 4.2: Reciprocal space map of $(\bar{1}\bar{1}3)$ reflex of cubic AlN, together with $(\bar{1}\bar{1}3)$ c–GaN reflex.

4.2 GaN/AlGaN Quantum Structures

In order to elucidate the properties of cubic GaN/$Al_xGa_{1-x}N$ quantum wells, several samples were grown with varying QW number, barrier Aluminum mole fraction x, and well thickness L_z. The general layout of the samples in question is shown in figure 4.3. For all samples the same template was used, consisting of a 2 inch GaAs(001) wafer with 300nm GaN coverage. On top of the GaN film 350nm $Al_xGa_{1-x}N$ was grown. This thickness effectively ensured the complete relaxation of the $Al_xGa_{1-x}N$ layer. This was followed by the deposition of five or twenty quantum wells. Finally, a 70nm $Al_xGa_{1-x}N$ cladding layer completed the structures. Throughout one sample, the Aluminum content x was kept constant. For all structures discussed here, the growth temperature was kept as $T_{sub} = 720°C$, which has been reported as the ideal temperature for GaN growth [62, 82, 90]. The growth of the quantum wells and barriers was accomplished by means of computer controlled MBE source shutter sequences, which enabled a timing with high accuracy and reproducibility.

The very streaky RHEED pattern in image 4.4 which was taken immediately after finishing the $Al_xGa_{1-x}N$ cladding layer makes it clear that the growth proceeded in a well–controlled stoichiometric fashion, as the half–order streaks of a (2x2) surface reconstruction are prominent. Neither spots due to hexagonal inclusions nor facetting because of increased surface roughness can be detected [62].

Diagram 4.5 details the transmission spectrum of a sample with a structure shown

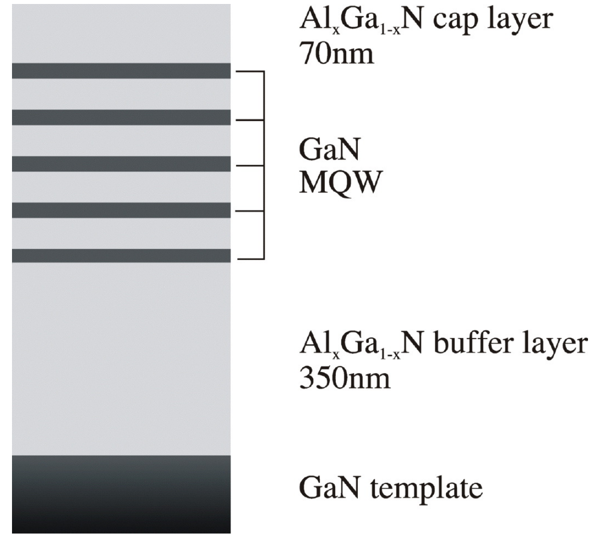

Figure 4.3: General layout of GaN/$Al_xGa_{1-x}N$ multi quantum well samples.

in fig. 4.3. The dominant absorption features are the absorption from the c–GaN buffer layer and the c-$Al_xGa_{1-x}N$ buffer layer, respectively. Their energetic positions agree well with the theoretical values of Rubio *et al.* (see diagram 2.1). Additionally, the transmitted intensity is at lower energies modulated by Fabry–Perot layer interference fringes.

The growth of epitaxial layers with lattice constants different from those of the substrate introduces strain which increases the epilayer energy. This process of course is proportional to the film thickness. This misfit strain energy can be relieved through the formation of dislocations, i.e. lattice faults which promote the transition to the layer's own lattice constant [145]. The layer thickness at which this process starts, the critical thickness, can be calculated by balancing the forces connected with the abovementioned mechanisms and finding the minimum with respect to the strain. The critical thickness is usually calculated following the method outlined by Matthews *et al.* assuming strain relief exclusively by edge dislocations [146]:

$$h_c = \frac{b}{2 \cdot \pi \cdot f} \cdot \frac{1 - \nu \cdot \cos^2 \alpha}{(1 + \nu) \cdot \cos \lambda} \cdot \left[\ln \left(\frac{h_c}{b} \right) + 1 \right]. \tag{4.1}$$

Here, b is the burgers vector associated with the dislocations which release the strain, and the Poisson ratio $\nu = \dfrac{c_{12}}{c_{12} + c_{11}}$. The angle α is spanned between the dislocation line and its Burgers vector, while λ is the angle between the dislocation slip direction and the epilayer plane perpendicular to both slip plane and interface. The misfit f between substrate and epitaxial layer is defined as before in equation (2.24).

Sherwin *et al.* demonstrated that in the case of cubic phase III–Nitrides with $\lambda = \alpha = 60°$ this expression reduces to

$$h_c = \frac{a_0}{\pi \cdot f \cdot \sqrt{2}} \cdot \frac{1 - \frac{\nu}{4}}{1 + \nu} \cdot \left[\ln \left(\frac{\sqrt{2} \cdot h_c}{a_0} \right) + \theta \right], \tag{4.2}$$

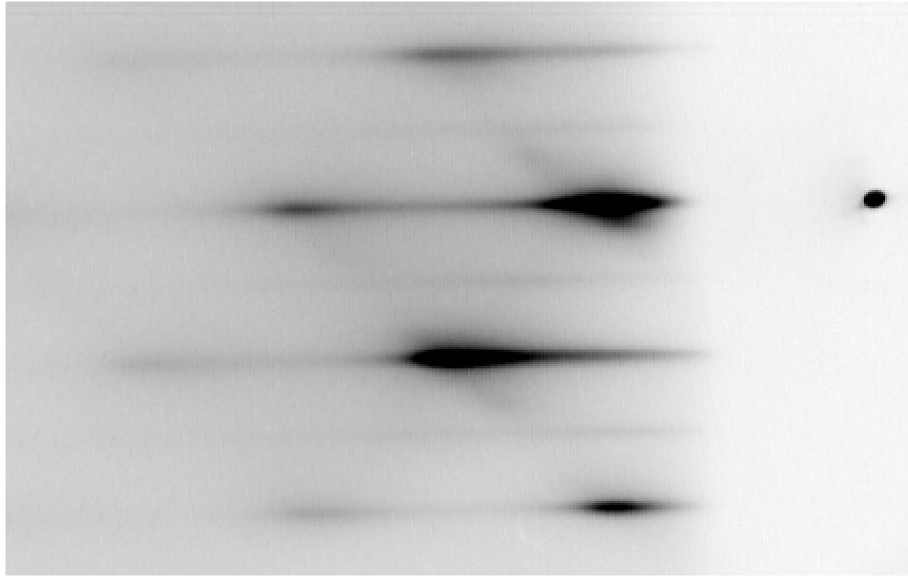

Figure 4.4: RHEED image of GaN/$Al_xGa_{1-x}N$ MQW sample in [$\bar{1}$10] azimuth, recorded after growth stop of $Al_xGa_{1-x}N$ cladding layer.

where a_0 is the substrate lattice constant, and θ represents the dislocation core energy parameter, which usually is assumed $\theta \approx 1$ [141].

On the basis of these considerations the critical layer thickness of $Al_xGa_{1-x}N$ layers on a GaN quasi–substrate, and that of GaN layers on $Al_xGa_{1-x}N$ films was calculated as a function of Aluminum mole fraction. The results are shown as diamonds — for the former case — and circles in diagram 4.6. The right ordinate displays the lattice misfit between c–GaN substrate and $Al_xGa_{1-x}N$ epilayer, where the lattice constant and the elastic properties of the ternary compound were supposed to vary linearly between the constituents (Vegard's law [57]). Likewise the elastic constants were interpolated linearly between the respective values of c–GaN and c–AlN.

Clearly the two critical thicknesses are nearly identical, which is no surprise considering the agreement in elastic constants (cf. tables 2.1 and 2.2) and the force symmetry. With respect to the similar elastic properties it is indeed suggestive that the respective substrate itself is compliant, i.e., yields to the strain exerted by the epilayer. That would naturally cause both functions on the left side of diagram 4.6 to coincide.

It appears particularly noteworthy GaN quantum wells of thicknesses not exceeding 10nm are obviously still strained for Aluminum fractions $x \leq 0.24$. This is an important result for the analysis of the QW luminescence in the following.

4.2.1 Modelling Quantum Structures

Experimentally it is observed that the transition energy of e.g. GaN/$Al_xGa_{1-x}N$ quantum structures depends both on the well thickness L_z and the $Al_xGa_{1-x}N$ barrier Aluminum content x. An example of this is presented in a later figureThese experimental findings may be analyzed using effective mass theory in analogy to the well–known quantum–mechanical problem of a finite well, where the most notable difference lies

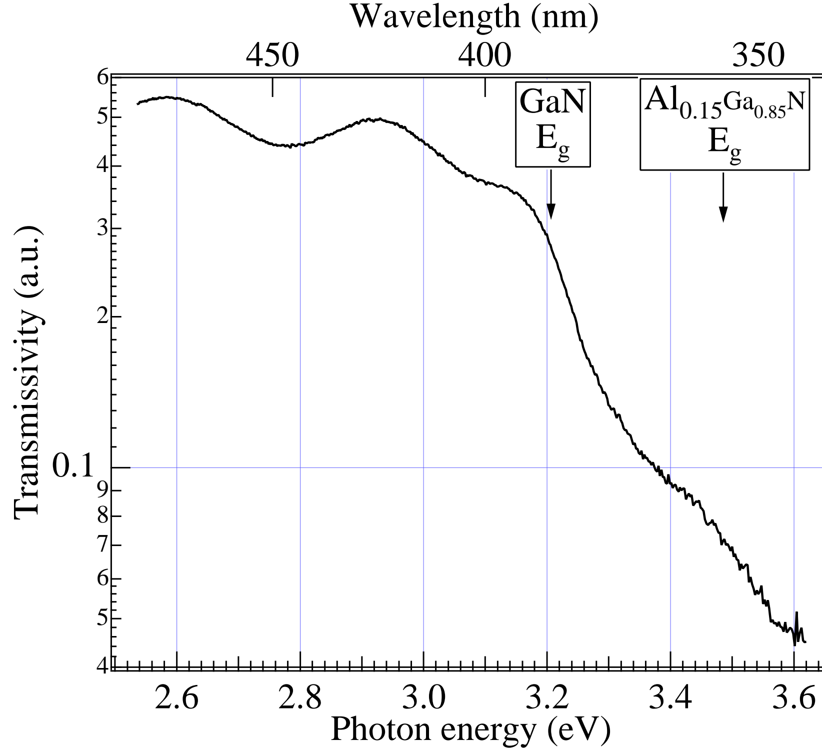

Figure 4.5: Transmission spectrum of a c–$Al_xGa_{1-x}N$ structure on c-GaN.

in the fact that in a semiconductor this problem has to be solved for all bands. A schematic representation of the situation is provided below:

Firstly, the different energy gaps of GaN and $Al_xGa_{1-x}N$ lead to a well of finite depth. However, for valence and conduction bands the band offset is different. Here the conduction band offset ΔE_C is assumed to be 60% of the total gap difference:

$$\Delta E_C = 0.6 \cdot (E_g^{barrier} - E_g^{well}). \tag{4.3}$$

Therefore the valence band offset

$$\Delta E_V = 0.4 \cdot (E_g^{barrier} - E_g^{well}). \tag{4.4}$$

Secondly, the QW valence and conduction bands experience a shift in their respective energetic positions due to the strain exerted by the pseudomorph growth process. Additionally, this strain lifts the energy level degeneracy of the heavy and light hole bands. For the involved bands of interest, the amount of the resulting energy shift is given by

$$E_C^{shift} = 2 \cdot a_C \cdot f \cdot (1 - \frac{C_{12}}{C_{11}}), \tag{4.5}$$

$$E_{V,hh}^{shift} = 2 \cdot a_V \cdot f \cdot (1 - \frac{C_{12}}{C_{11}}) + b \cdot f \cdot (1 + 2 \cdot \frac{C_{12}}{C_{11}}), \tag{4.6}$$

$$E_{V,lh}^{shift} = 2 \cdot a_V \cdot f \cdot (1 - \frac{C_{12}}{C_{11}}) - b \cdot f \cdot (1 + 2 \cdot \frac{C_{12}}{C_{11}}). \tag{4.7}$$

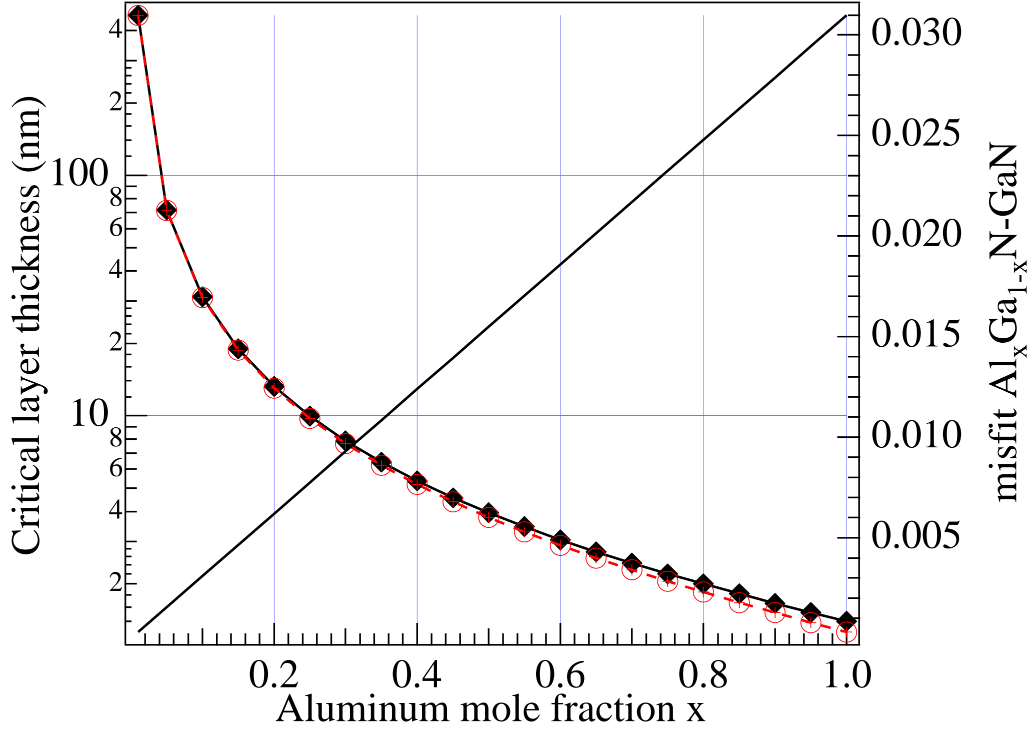

Figure 4.6: Critical thickness of $Al_xGa_{1-x}N$/GaN (diamonds) and GaN/$Al_xGa_{1-x}N$ layers (circles) as a function of Aluminum mole fraction x (left). The misfit between $Al_xGa_{1-x}N$ and GaN is shown on the right.

Here, $a_C = -2.8eV$, $a_V = 3.63eV$ and $b = -2.67eV$ are the GaN conduction and valence band deformation potentials [19, 147]. With these energies it is possible to determine the quantum well depth as

$$V_e = \Delta E_C - E_C^{shift}, \tag{4.8}$$
$$V_{hh} = \Delta E_V + E_{V,hh}^{shift}, \tag{4.9}$$
$$V_{lh} = \Delta E_V + E_{V,lh}^{shift}. \tag{4.10}$$

Now it is, in a third step, necessary to solve the Schrödinger equation for the respective potential wells V_e, V_{hh}, and V_{lh} in order to determine the respective QW states. Defining the resulting well energy ground states ($n = 1$) as E_e, E_{hh}, and E_{lh} accordingly, the exciton quantum well transitions can finally be calculated as

$$E_{hh,X} = E_g^{well} + E_e + E_{hh} - E_X, \tag{4.11}$$
$$E_{lh,X} = E_g^{well} + E_e + E_{lh} - E_X. \tag{4.12}$$

The remaining problem concerns the unknown exciton binding energy, which is influnced by the QW width. However, as the variations in exciton binding energy are on the same order as the variations in transition energy caused by uncertainties in the Aluminum mole fraction, this influence has been neglected in the present treatise, and the exciton binding energy was assumed constant [148, 149, 150].

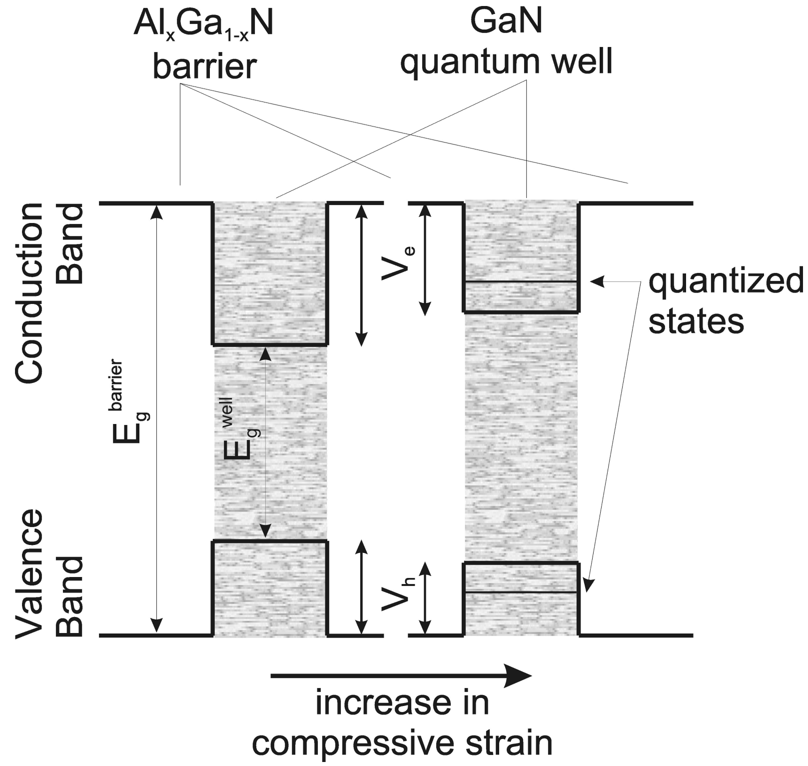

Figure 4.7: Schematic of the energetic positions in a $GaN/Al_xGa_{1-x}N$ QW system.

Moreover, the strained layer quantum well model discussed above was modified in order to account for the gradual release of strain in the well. Therefore the misfit f in equations (4.5)–(4.7) was replaced by an adjusted misfit $F = f \cdot g$, where g corrects for the strain reduction in layers of thickness $h > h_c$. As it has been demonstrated e.g. in reference [151], the epilayer lattice constants will gradually relax. This can be modelled in the following way:

$$g(h) = \begin{cases} 1 & ; \quad h < h_c \\ 2 - e \cdot \exp\left(\dfrac{-h_c}{h}\right) & ; \quad h_c \leq h \leq 3 \cdot h_c \\ 0 & ; \quad h > 3 \cdot h_c \end{cases} \qquad (4.13)$$

4.2.2 Structural Properties

X–ray

Asymmetric X–ray measurements — which provide access to both reciprocal lattice vectors — demonstrate the complete relaxation of the QW $Al_xGa_{1-x}N$ barriers, as can be seen for example in the RSM in graphs 4.8 and 4.9, where both GaN and $Al_{0.08}Ga_{0.92}N$ buffer layer reflexes are seen to occupy their respective reciprocal lattice positions.

The GaN quantum wells, which would be pseudomorphically strained to the respective $Al_xGa_{1-x}N$ barriers and therefore occupy a position with the same lateral

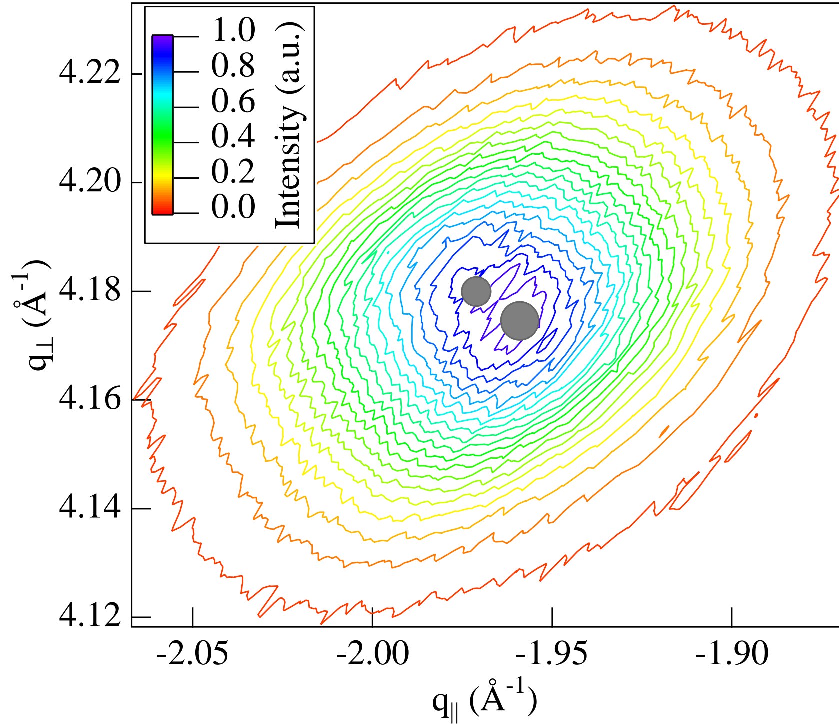

Figure 4.8: Reciprocal space map of the $(\bar{1}\bar{1}3)$ reflex of a GaN/$Al_{0.08}Ga_{0.92}N$ multi quantum well sample.

reciprocal space vector as the $Al_xGa_{1-x}N$ barrier, cannot be resolved because of their small total sample volume and hence extremely low X–ray intensity.

A high–resolution XRD $\omega - 2\theta$ scan of the (002) reflex of a multi quantum well structure is shown as the top line in figure 4.10. Clearly recognizeable are the Bragg peaks of the cubic Gallium Nitride template layer and the $Al_{0.24}Ga_{0.76}N$ buffer. Under the relatively broad reflexes — due to the dislocation density on the order of $10^{10}cm^{-2}$ — one can see additional peaks that can be attributed to higher–order MQW superlattice peaks. The bottom curve is a fit to the experimental data using a dynamic scattering model of Brandt *et al.* [152]. The simulation shown here yields a well width $L_z = 5nm$ and a corresponding barrier width of 10nm, in excellent agreement with the targeted growth values (estimated by *ex situ* growth rate measurements). The line in between is the product of a convolution of the dynamic model (bottom line) with the instrument response, resulting in a general broadening of the simulated SL structure peaks and in a perfect fit [153]. For a better comparison, experimental data and fit curves are normalized.

Neither reciprocal space maps nor $\omega - 2\theta$ scans over various reflexes — for the sake of clarity not shown here — detected peaks which could possibly be ascribed to hexagonal phase material.

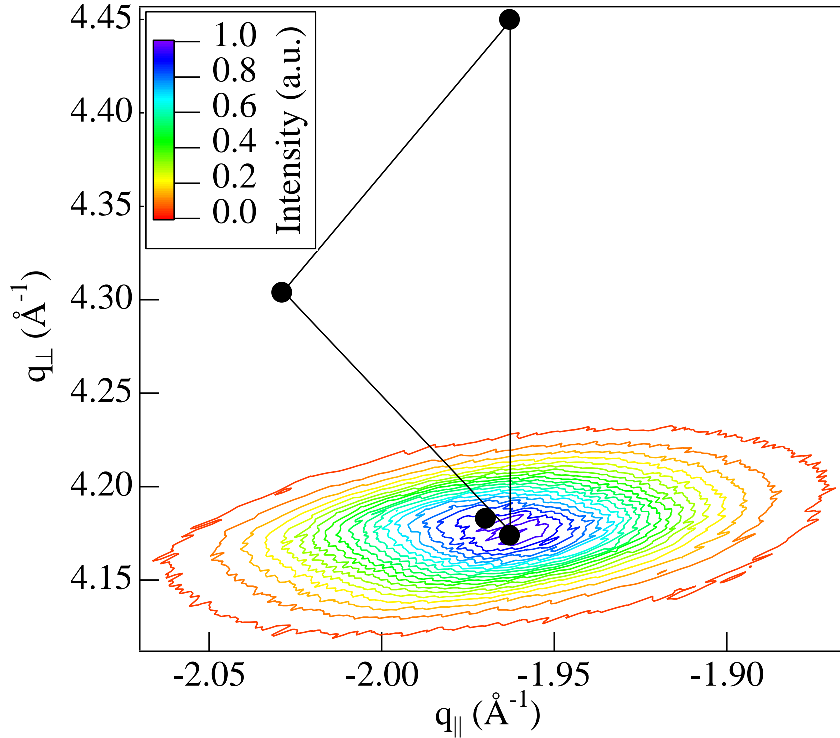

Figure 4.9: RSM of the $(\bar{1}\bar{1}3)$ reflex of a GaN/$Al_{0.08}Ga_{0.92}N$ MQW sample — see preceding figure — in conjunction with the predicted positions of the totally relaxed cubic AlN and the pseudomorphically strained c–AlN in reciprocal space.

Transmission Electron Microscopy

TEM as a method for direct electronic imaging of samples with truly atomic resolution allows the ultimate proof of the existence of quantum wells. The TEM images shown here were taken at Electron Microscopy Lab at Karlsruhe University by V. Potin in the group of Prof. D. Gerthsen.

Figure 4.11 showcases the chemical contrast due to the different atom scattering constants of Aluminum and Gallium. The fivefold GaN quantum well is clearly recognizable between the $Al_xGa_{1-x}N$ barrier and buffer layer.

However, the figure 4.11 also shows a large number of threading dislocations, approximately $1 \cdot 10^{11} cm^{-2}$. In order to achieve lasing action the dislocation density needs to be reduced drastically. It is in this regard very interesting to observe that the dislocations imaged here exhibit a high degree of bunching, i.e., one can distinguish regions with extremely high fault density, and regions that are nearly defect free. Further inspection of the TEM image shows that some of the dislocations are bent at the interfaces between quantum well and barrier. This opens up new paths towards the reduction of dislocation densities: the growth of GaN/$Al_xGa_{1-x}N$ superlattices with 20–50 periods that bend a sufficient number of dislocations off the growth direction. In fact, this method is well–known for the growth of GaAs–based semiconductor devices [10].

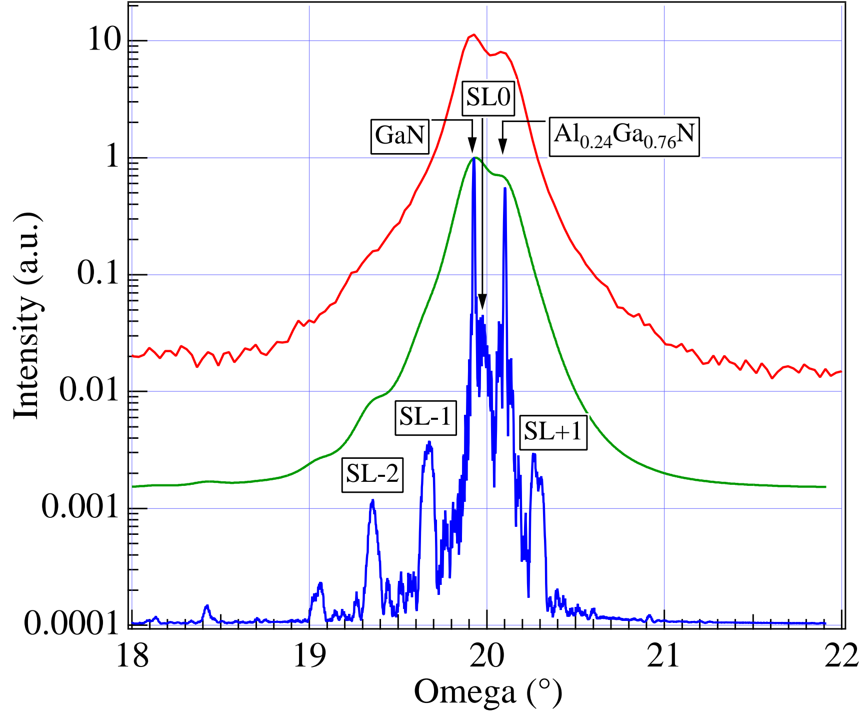

Figure 4.10: High–resolution $\omega - 2\theta$ scan of (002) GaN/$Al_{0.24}Ga_{0.76}N$ MQW reflex.

Moreover, image 4.11 demonstrates that the dislocation density in growth direction is overall decreasing.

The truly atomic resolution of the TEM images is demonstrated with figure 4.12 which is an enlargement of figure 4.13. It therefore allows an analysis of well and barrier widths by counting the individual atom rows.

The atomic reolution image shows clearly the interface sharpness between the QWs and the barriers.

The comparison of the nominal well widths of 2.5nm and 5nm, respectively, with the critical thicknesses in graph 4.6 tells that the GaN quantum wells should be pseudomorphically strained to the $Al_xGa_{1-x}N$ barriers. This consideration allows the calibration of the well thickness using the TEM images by applying the relation

$$L_z = n_{Monolayer} \cdot \frac{a_\perp}{2}, \tag{4.14}$$

where $a_\perp$ denotes the vertical lattice constant of GaN.

For cubic epilayers grown on lattice mismatched cubic substrates in <001> growth direction the strain is biaxial, i.e. $\sigma_{xx} = \sigma_{yy} \neq 0$, whereas the other components of the strain tensor are zero. Therefore the non–symmetric components of the stress tensor are zero, and $\epsilon_{||} = \epsilon_{xx} = \epsilon_{yy} \neq \epsilon_{zz} = \epsilon_\perp$. Letting a_0 be the lattice constant of the unstrained film and $a_\perp$ and $a_{||}$ the modified lattice constants in growth direction and

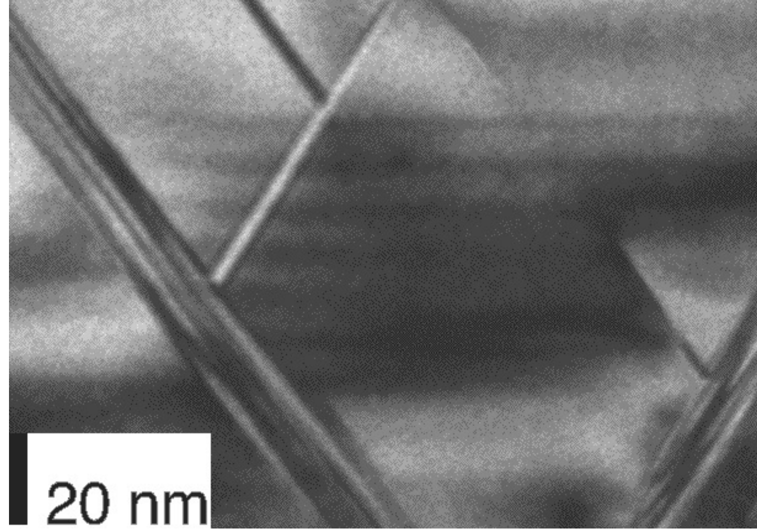

Figure 4.11: TEM image of fivefold GaN quantum well with $Al_{0.24}Ga_{0.76}N$ barrier.

parallel to the interface, respectively, the stresses are given by [154]

$$\epsilon_{||} = \frac{a_{||} - a_0}{a_0}, \quad (4.15)$$

$$\epsilon_{\perp} = \frac{a_{\perp} - a_0}{a_0}. \quad (4.16)$$

For cubic symmetry both are related as

$$\epsilon_{\perp} = -\frac{2 \cdot C_{12}}{C_{11}} \cdot \epsilon_{||}. \quad (4.17)$$

Thus it is possible to calculate $a_{\perp}$ of the GaN QW and eventually the total well width from the known lattice constant of the unstrained $Al_xGa_{1-x}N$ barrier:

$$a_{\perp} = \frac{2 \cdot C_{12}}{C_{11}} \cdot [a_0 - a_{||}] + a_0. \quad (4.18)$$

The result of those calculations is shown in graph 4.14. It becomes impressively clear that the quantum well thicknesses L_z and barrier widths both fluctuate on average by two monolayers at the most, i.e. only 10%. The deviation which can be observed for the barrier can be explained by poor statistics. Therefore every interface can be considered as having only one monolayer roughness. This is an extraordinary and surprising result, taking into account the relatively low intensity of superlattice peaks measured using X–ray diffraction. On the other hand this remarkable interface smoothness may well be the cause of the high QW luminescence intensity, which will be dealt with in the following chapter 4.2.3.

The fluctuation of QW and barrier width over growth time is demonstrated in figure 4.15. Each point corresponds to the average of several independent measurements. The thickness variation is comparatively small, as well as the change during the growth process, i.e., during the progression from well no. 1 to well number 4.

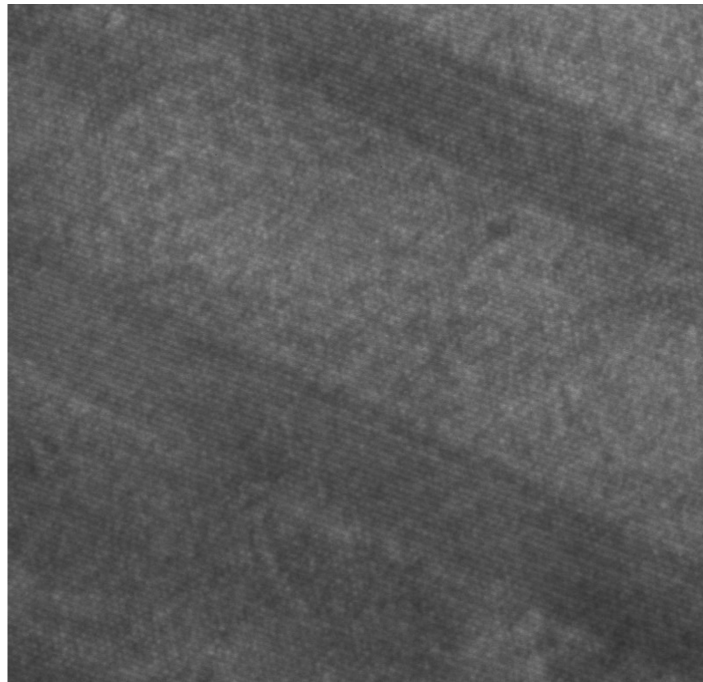

Figure 4.12: TEM image of GaN MQWs with atomic resolution.

At the same time, it is remarkable that the measured well widths are smaller than their nominal values. Those were calculated from the growth rates of the respective preceding samples. This difference can easily be explained by the chosen growth mode: The $Al_xGa_{1-x}N$ buffer layer and barriers were grown stoichiometrically. Therefore, the GaN wells were grown simply by shuttering the Aluminum beam to off. This of course leads to a correspondingly decreased metal flux, resulting in the above–mentioned thinner GaN wells [153].

Table 4.3 summarizes the TEM data:

	nominal width	experimental width	difference
well	5.0nm	3.9nm	-22%
barrier	10.0nm	8.7nm	-13%

Table 4.3: Summary of TEM data for 5nm/10nm GaN/$Al_{0.24}Ga_{0.76}N$ multi quantum well structure

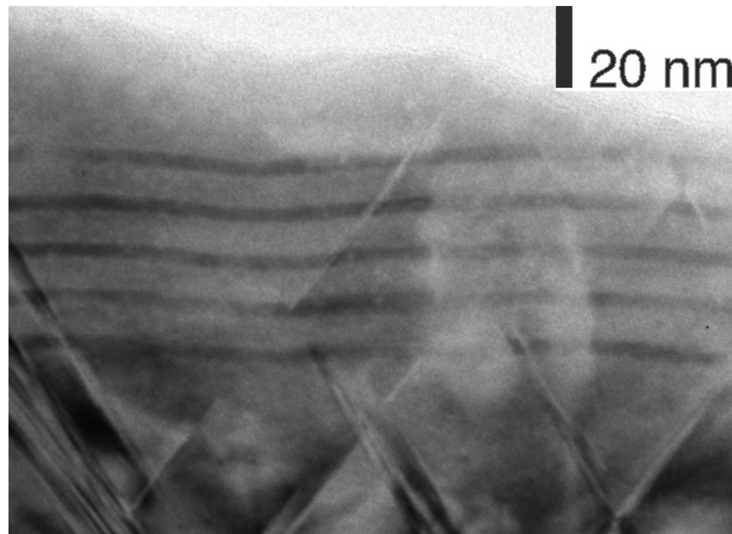

Figure 4.13: TEM image of a GaN multi quantum well.

AFM

The influence of Aluminum incorporation on the surface quality has been investigated. Figure 4.16 shows AFM images of a multi quantum well sample with $x = 0.08$ at different lateral scales. The $(100\mu\text{m})^2$ image is the first derivative of the actual height contour (with respect to the scan direction). This increases the contrast between the different surface features. The smaller scale images ($(10\mu\text{m})^2$ and $(5\mu\text{m})^2$, the latter in 3D view) emphasize that the Aluminum percentage does not influence the overall cubic Gallium Nitride structure (see for example reference [62]).

4.2.3 Luminescence

Figure 4.17 shows typical room temperature Cathodoluminescence spectra of a multi quantum well structure, where the typical layout is detailed in figure 4.3, as a series of spectra recorded at different electron beam energies. As discussed earlier in chapter 2.2.1, the differences in the spectra are caused by differences in excitation probing depth.

In order to clarify the assignment of the CL transitions, it was found that the series of apparent peaks in the range 2.4eV–3.2eV are due to Fabry–Perot thin film interference fringes. This is based upon additional PL measurements, where those peaks shifted energetically with a variation of the luminescence collecting angle away from the surface normal. This shift, as can readily be seen from equation (2.10), is caused by increasing angle α and thus the effective film thickness. Therefore, all peaks at energies below 3.2eV will be neglected in the following discussion.

Two transitions are found to be dominant. The energetically highest transition, labelled '$Al_{0.24}Ga_{0.76}N$ bulk', is attributed to the emission of the $Al_{0.24}Ga_{0.76}N$ buffer and cladding layers, the second peak as the GaN quantum well luminescence. Figure 4.18 pictures the ratio of both luminescence intensities as a function of electron beam accel-

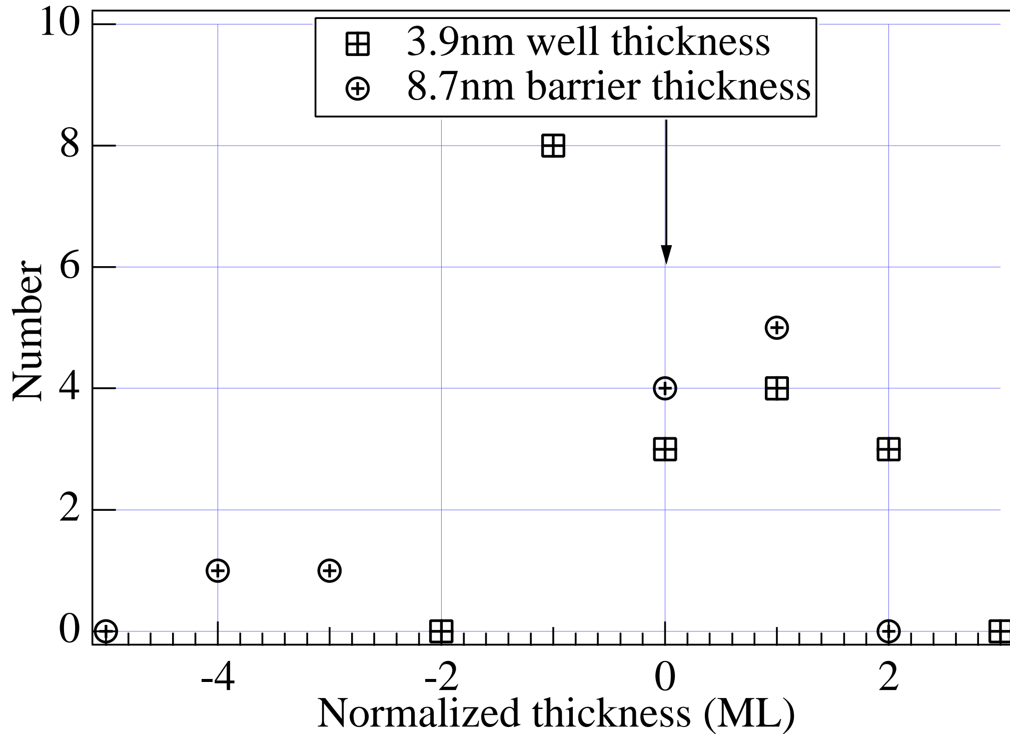

Figure 4.14: Fluctuation of QW and barrier thickness for one sample.

eration voltage, and thus different probing depth. For high beam energies most of the luminescence is excited in the bottom $Al_{0.24}Ga_{0.76}N$ buffer layer, with the result of the bulk '$Al_{0.24}Ga_{0.76}N$' transition being the highest in intensity. With decreasing electron beam penetration depth the intensity of this energetically highest transition decreases to a greater extent than the second transition, which becomes the strongest transition for penetration depths around 300nm. At this depth, hardly any $Al_{0.24}Ga_{0.76}N$ buffer layer luminescence would be excited, but the QW luminescence might be expected to dominate the spectrum. At extremely shallow excitation depths however, this should change once more, leaving only the cladding layer to luminesce.
This scenario can indeed be observed, as figures 4.17 and 4.18 demonstrate.

Furthermore, two multi quantum well structures are compared in figure 4.19. The first sample contains 20 quantum wells, whereas the second sample (shown as the lower curve) possesses only five QWs. All other parameters, such as barrier height and thickness, QW width and buffer layer thickness were kept constant.

Therefore the difference in the spectra is caused by the different number of GaN quantum wells contained in the samples. However the extremely high quantum well luminescence intensity of the 20 MQW sample has to be explained not only in terms of the total QW excitation volume (increased by a factor of three) and the electron capture process therein but also in terms of absorption of higher–energy $Al_{0.24}Ga_{0.76}N$ bulk luminescence and subsequent re–emission in the GaN QWs.

The intensity ratio of GaN quantum well emission and $Al_xGa_{1-x}N$ bulk luminescence of diagram 4.19 has been modelled along the arguments of reference [53]. Here,

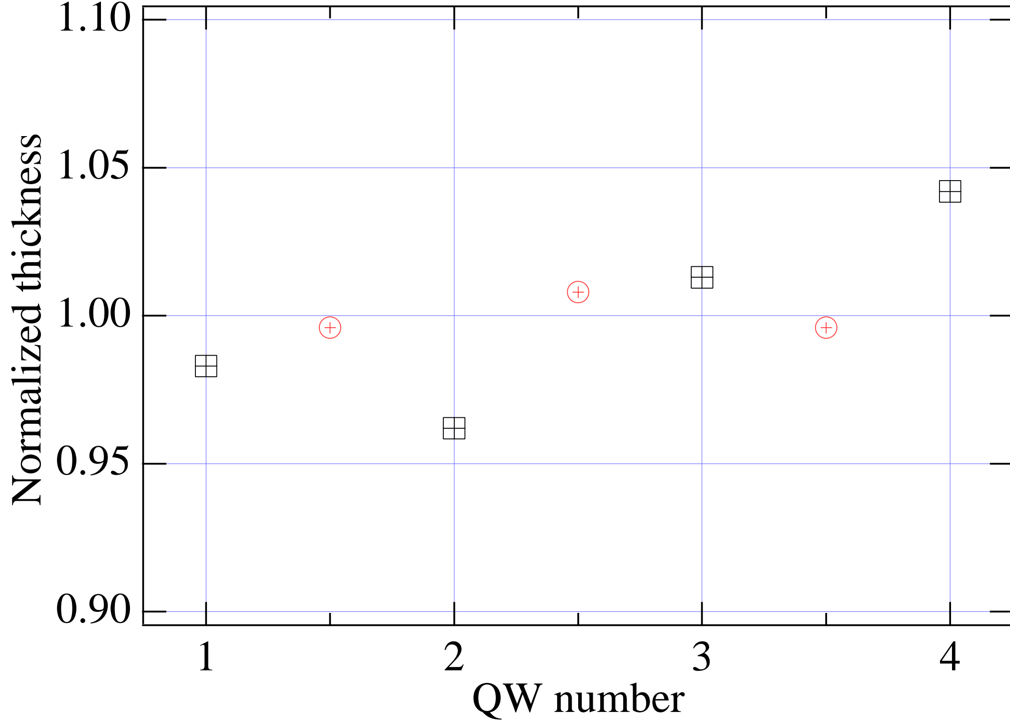

Figure 4.15: Variation of QW (squares) and barrier (circles) thickness in growth direction.

the $Al_xGa_{1-x}N$ bulk intensity is composed of the contribution $I_{cladding}$ of the top cladding layer, and the $Al_xGa_{1-x}N$ buffer layer (I_{buffer}). Each intensity fraction at depth z_0 is considered to suffer from re–absorption in parts of the sample with depths $z < z_0$. In contrast, the QW luminescence I_{MQW} is assumed not to be subjected to re–absorption, because of the substantially lower gap energy. The part of the $Al_xGa_{1-x}N$ buffer intensity which is absorbed in the MQW region is supposed to be re–emitted as QW luminescence as well. Given these considerations the individual contributions can be written as

$$\begin{aligned} I_{buffer} &= e^{-(\alpha_{GaN}\cdot d_{QW}+\alpha_{AlGaN}\cdot d_{barrier}+\alpha_{AlGaN}\cdot d_{cladding})} \\ &\times \int_{\frac{d_{MQW}+d_{cladding}}{R_e}}^{1} dt\cdot E(t)\cdot g(t,x)\cdot e^{-\alpha\cdot(t-\frac{d_{MQW}-d_{cladding}}{R_e})} \end{aligned} \tag{4.19}$$

$$I_{cladding} = \int_0^{\frac{d_{cladding}}{R_e}} dt\cdot E(t)\cdot g(t,x)\cdot e^{-\alpha\cdot(t-\frac{d_{MQW}-d_{cladding}}{R_e})}, \tag{4.20}$$

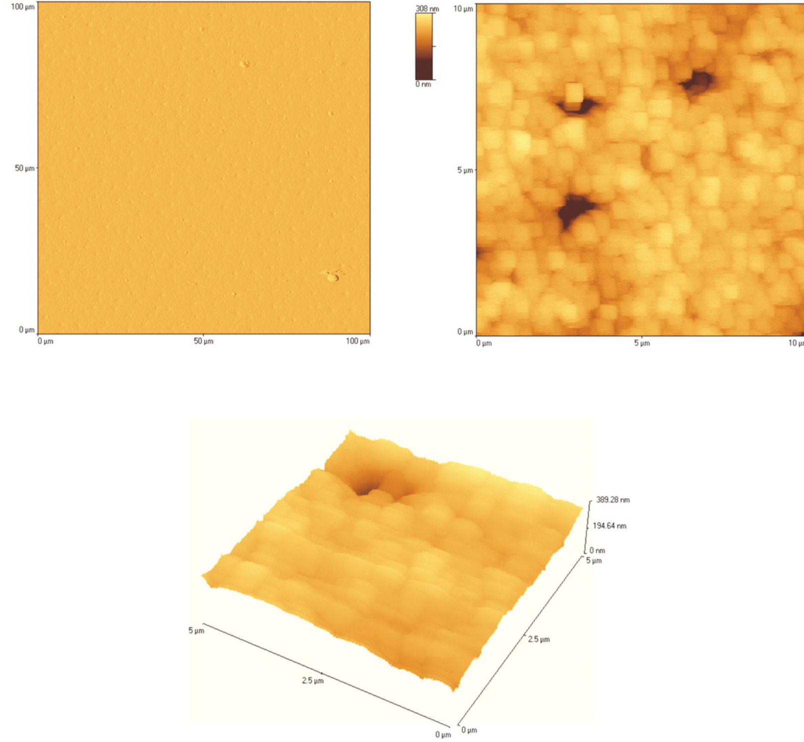

Figure 4.16: AFM images of GaN/$Al_{0.08}Ga_{0.92}N$ MQW sample, at different lateral scales of $(100\mu m)^2$, $(10\mu m)^2$, and $(5\mu m)^2$ (threedimensional image), respectively.

$$\begin{aligned} I_{MQW} &= [1 - e^{-(\alpha_{GaN} \cdot d_{QW} + \alpha_{AlGaN} \cdot d_{barrier})}] \\ &\quad \times \int_{\frac{d_{MQW}+d_{cladding}}{R_e}}^{1} dt \cdot E(t) \cdot g(t,x) \cdot e^{-\alpha \cdot (t - \frac{d_{MQW} - d_{cladding}}{R_e})} \\ &\quad + \int_{\frac{d_{cladding}}{R_e}}^{\frac{d_{MQW}+d_{cladding}}{R_e}} dt \cdot E(t) \cdot g(t,x). \end{aligned} \tag{4.21}$$

Here the excitation depth is normalized as $t = z/R_e$. According to reference [155] the electron flux density $E(t)$ can be expressed as a function of depth:

$$E(t) = 0.6 + 6.21 \cdot t - 12.4 \cdot t^2 + 5.69 \cdot t^3. \tag{4.22}$$

Further it is necessary to calculate the number of electron–hole pairs generated by the impinging high energy electrons. The generation rate is given as [53, 155]

$$g(t,x) = \frac{E_b(t)}{3.2 \cdot E_g(x)} \cdot \left(1 - \frac{Z(x)}{100}\right). \tag{4.23}$$

The dependence of atom number $Z(x)$ from the Aluminum mole fraction x is given in equation (2.14). Likewise the band gap energy was assumed to vary linearly in agreement with diagram 2.1. The electron beam energy varies as

$$E_b(t) = E_0 \cdot (1 - t \cdot E(t)). \tag{4.24}$$

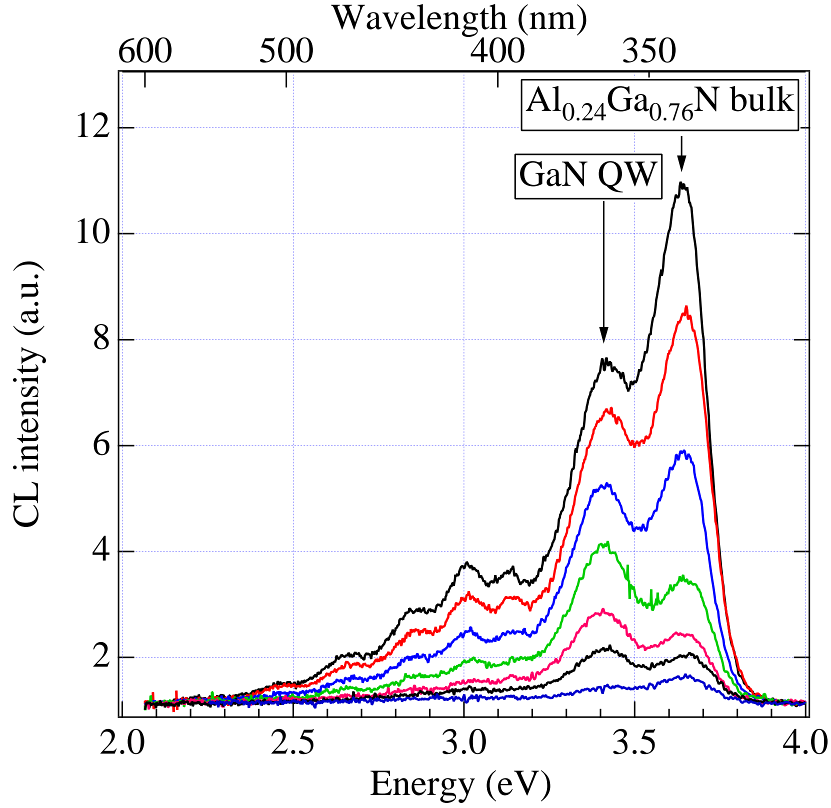

Figure 4.17: Room temperature CL spectra of 2.5nm GaN well/5nm $Al_{0.24}Ga_{0.76}N$ barrier 5 QW sample, taken with electron beam voltages (top to bottom) 10kV, 9kV, 8kV, 6kV, 5kV, 4kV, 3kV.

The remaining open question lies in the determination of the $Al_xGa_{1-x}N$ absorption coefficient α_{AlGaN}. The simulation process yielded however meaningful results only for $\alpha_{AlGaN} = \alpha_{GaN}$, where the absorption coefficient of cubic Gallium Nitride was taken from the literature [50] and assumed constant for all individual bands.

In order to compare the above model with the experiment (for example the results of figure 4.19), the cathodoluminescence spectra were fitted separately, and the respective band areas interpreted as intensities. The QW:$Al_xGa_{1-x}N$ intensity ratios are listed in table 4.4.

sample structure	experimental	model
5xMQW 2.5nm/5nm	3.2	3.2
20xMQW 2.5nm/5nm	14	6.1
5xMQW 5nm/10nm	3.7	5.4
20xMQW 5nm/10nm	6.4	15.2

Table 4.4: Results for spectral intensities of GaN/$Al_{0.24}Ga_{0.76}N$ multi quantum well samples, at room temperature.

Most remarkably, the model fits the intensity ratios for low well numbers extremely

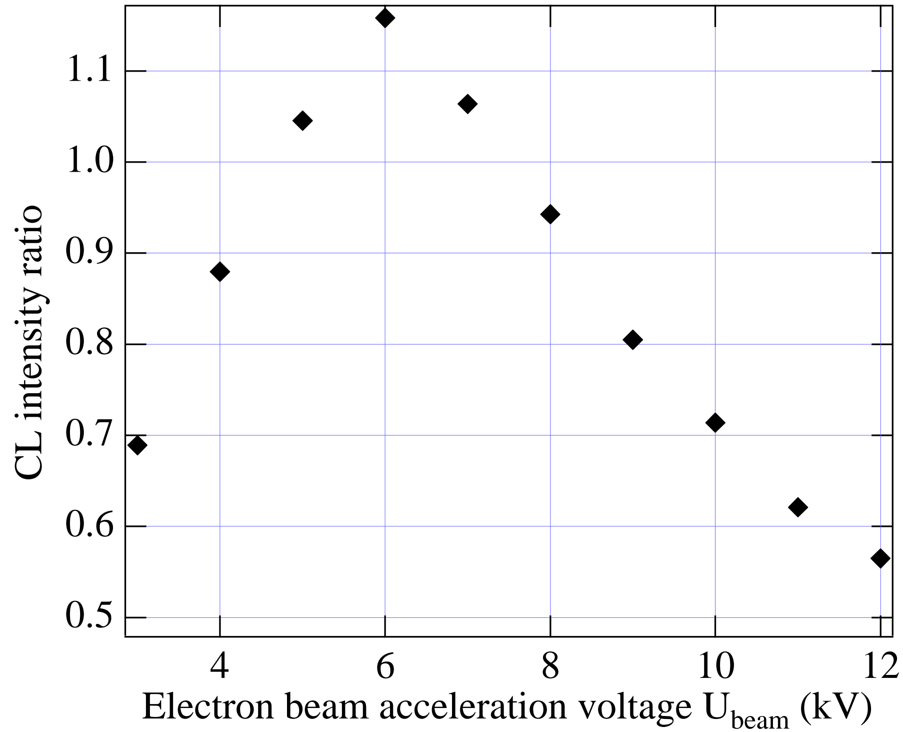

Figure 4.18: Ratio of GaN quantum well luminescence intensity to $Al_{0.24}Ga_{0.76}N$ bulk luminescence as a function of electron penetration depth.

well. The increase in QW luminescence for high QW numbers is in one case over–, in the other case underestimated. The reasons for this behaviour are not clear yet, however different influences have not been accounted for. To name but a few, there are absorption processes through non–radiatively decaying defects, or differences between assumed c–GaN absorption and the real c–GaN QW absorption because of changes in the well density of states compared with bulk material.

A summary of the effects of varying the well width L_z and the barrier Aluminum content x on the room temperature Cathodoluminescence spectra is shown by means of three typical spectra in figure 4.20, with constant CL excitation conditions. The curved line 'c–GaN QW emission' shows the shift of the QW emission as a function of well width and barrier height, as predicted by the simulations in chapter 4.2.1. Thus the assignment of the peaks in figure 4.17 is confirmed.

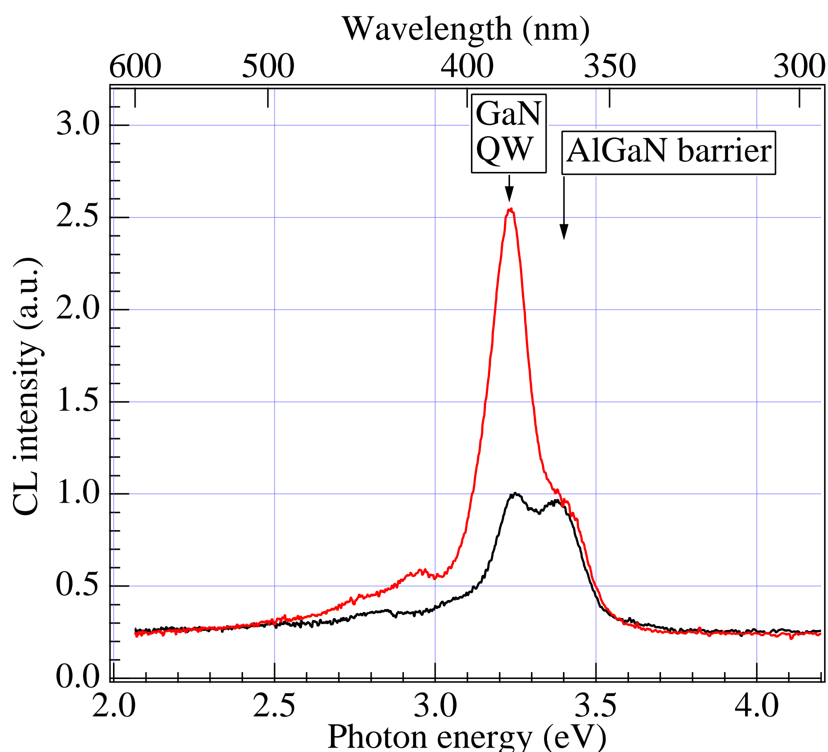

Figure 4.19: Room temperature CL spectra of GaN/$Al_xGa_{1-x}N$ MQW samples; upper curve of a 20x multi quantum well, lower curve of a five well structure.

4.3 Discussion

The conventional c–GaN growth process as reported e.g. in references [82, 62, 63], was applied to the growth of c–AlN films and strained GaN/$Al_xGa_{1-x}N$ quantum wells.

In the case of bulk cubic Aluminum Nitride, unfortunately no luminescence could be excited. Incidentally, most of the experimental data summarized in table (4.1) are results of absorption measurements. Both observations may well be explained by the fact that c–AlN is predicted to be an indirect semiconductor [17, 21, 40].

The cubic phase purity of the Aluminum Nitride films and strained GaN/$Al_xGa_{1-x}N$ quantum wells is obvious from the RSMs and $\omega - 2\theta$ scan. The TEM results make it possible to infer the high degree of well and barrier thickness reproduceability shown in figure 4.15. Clearly, the individual thicknesses do not vary much in growth direction; the deviations are merely the monolayer fluctuations discussed earlier. The atomically sharp interfaces (see for example TEM image 4.12) cause a high luminescence intensity, as evidenced in figure 4.17. This is however seemingly contradictory to the only weak X–ray superlattice peaks as shown in fig. 4.10. A closer inspection of the GaN quantum wells reveals a rather 'wavy' structure of the QWs and barriers at larger scales (see images 4.11 and 4.13). Yet the thicknesses remain constant. A closer look shows that indeed the growth front itself seems warped, since the single atom rows of fig. 4.12 themselves lie on straight lines, and the chemical contrast suggests a change of the lines from $Al_xGa_{1-x}N$ to GaN and vice versa. It may be speculated here that this

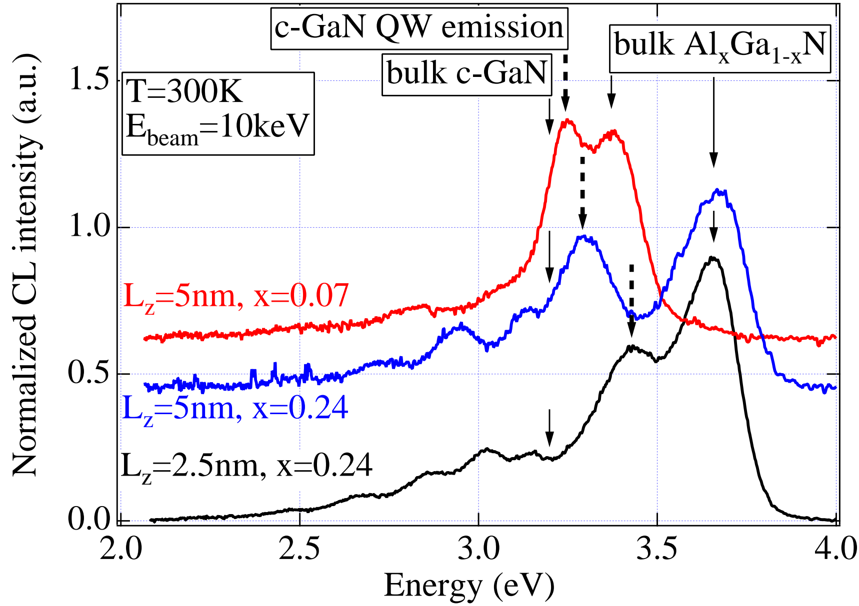

Figure 4.20: Variation of GaN quantum well luminescence peak energy with well width and barrier Aluminum mole fraction.

is due to the influence of non–ideal conditions, i.e. a three–dimensional surface during the start of the regular c–GaN epilayer which simply propagates through the whole film.

These observations suggest a solution for the abovementioned discrepancy between X–ray and CL measurements: the quantum wells are actually defect free and homogeneous on lateral scales exceeding the exciton Bohr radius, leading to a high quantum efficiency. On larger scales though the QWs bend, destroying the long–range coherency necessary for measurable X–ray intensities.

Furthermore the TEM investigation of the MQW samples showed that the interfaces between wells and barriers bend dislocation lines. This potentially opens up a way to an effective reduction of the dislocation density by growing GaN/Al$_x$Ga$_{1-x}$N or GaN/AlN superlattices.

The transition energies of GaN/Al$_x$Ga$_{1-x}$N quantum wells were simulated using effective mass theory, as laid out in chapter 4.2.1. The results are shown in figure 4.21 as lines for Aluminum mole fractions of $x = 0.48$, $x = 0.25$ and $x = 0.08$, respectively, from top to bottom.

For better comparison, CL room temperature transition energies of samples with corresponding x are also shown in the diagram. The well widths are the actual L_z values from TEM measurements and therefore differ from their nominal values. The good agreement between model and experimental data is clear, especially considering the aforementioned uncertainty in elastic data for c–AlN. However, with increasing barrier Aluminum content, a steady difference between the simulated values (cf. equation (4.11)) and the experimental results can be noticed. A similar observation was reported by Caetano *et al.*, who considered the effects of a gradual transition from well to barrier

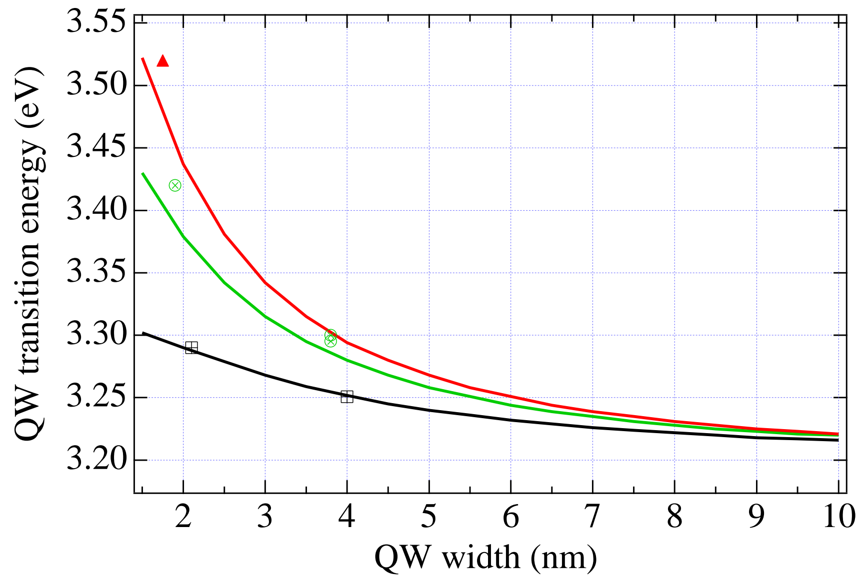

Figure 4.21: Model calculations for strained c–GaN quantum wells of widths L_z with $Al_xGa_{1-x}N$ barriers of Aluminum mole fraction x, compared with CL peak energies.

instead of the usually assumed step–like interface [150]. It is noted that both carrier ground states and exciton binding energy increase for an increasing ratio of interface width to well width. This effect may easily be accounted for when considering the fact that with increasing interface width the effective well width decreases. Since the strength of this effect obviously depends strongly on the barrier Aluminum content and well width, it is especially noticeable for high Al mole fractions and small widths, in agreement with the findings presented here.

Chapter 5

Conclusions

In the course of the work for this Ph.D. thesis, cubic phase GaN, AlN, and $Al_xGa_{1-x}N$ films were grown on GaAs substrates supplied by *Freiberger Compound Materials* in a Riber 32 MBE system. Active Nitrogen was supplied using high–purity Nitrogen, an in–line gas purifier and an inductively coupled radio frequency (rf) plasma source HD25 of *Oxford Applied Research.* Typical growth rates at a substrate temperature $T_S = 720°C$ were $90nm/h$. Care was taken in order to ensure stoichiometric growth conditions. Using low–temperature photoluminescence, the overall volume concentration of hexagonal phase material was estimated to be less than one percent. X–ray measurements verified this. These samples exhibited p–type conductivity at hole concentrations $p \approx 10^{16}cm^{-3}$ and mobilities $\mu \approx 200cm^2/Vs$.

The focus of this work was divided between two rather different fields:

- the exploration of the properties of Carbon in cubic Gallium Nitride,
- extension of the range of cubic Nitrides to cubic Aluminum Nitride and the respective ternary compounds and subsequent application to quantum well structures, while keeping the growth temperature constant.

As a zeroeth order prerequisite, the nucleation procedure of c–GaN growth on Gallium Arsenide substrate wafers was revised. Layers of cubic Gallium Nitride of comparable thickness were grown under identical conditions except for the nucleation process. The quality of the epilayers was judged by the X–ray rocking curve FWHM and the photoluminescence FWHM. Rocking curve half–widths of 20 arc min demonstrate that a carefully chosen and optimized nucleation process obviates the necessity for technologically more complex procedures, such as nucleation on prepatterned GaAs substrates. Optimum nucleation requires a Nitrogen:Gallium ratio of 2:1.

Firstly, the properties of Carbon in c–GaN and its possible suitability as an alternative acceptor were investigated. Elemental Carbon was produced by means of two different sources, a graphite filament cell and an electron beam evaporation cell. The former was a completely new development in the frame of this thesis, while the latter underwent modifications in order to be commissioned. Both sources were calibrated externally by growing GaAs:C films and evaluating the acceptor concentrations via Hall measurements. Maximum Carbon atom fluxes of $F_C = 1 \cdot 10^{12}cm^{-2}s^{-1}$ could be

achieved. The validity of these calibrations was verified by SIMS measurements of the Carbon concentration in GaN:C samples.

The Carbon incorporation was investigated optically as a function of Carbon flux. Low–temperature measurements showed the emergence of a near band edge transition and, for high Carbon concentrations, a deep luminescence around 2eV. This deep luminescence quenches the near band edge luminescence. Variable–temperature PL proved the Carbon related near band edge PL peak to actually consist of two separate transition lines separated by 28meV. The different thermalization of those lines led to the assignment of a band–acceptor and donor–acceptor transition line, respectively. The acceptor binding energy could be determined as 215meV.

Electrical characterization of the GaN:C films showed an inital increase in room temperature hole concentration, followed by a steep decline. This behaviour is known as Magnesium self–compensation effect in hexagonal GaN. An appropriate model was used to simulate the conditions in c–GaN. The most likely candidate for Carbon self–compensation is the Carbon interstitial, a deep quadruple donor with optical transitions around 2eV. VT Hall measurements showed an activation energy of the acceptor of 205meV, in good agreement with the PL result.

Secondly, cubic Aluminum Nitride and $Al_xGa_{1-x}N$ films were grown successfully, keeping the same growth temperature as for GaN growth. The c–AlN could be grown either on c–GaN template layers or via direct AlN nucleation on the GaAs substrate. X–ray measurements demonstrated the phase purity and complete relaxation of the c–AlN films. Similar to the c–GaN epilayers, the c–AlN exhibited p–type conductivity at high mobilities up to $\mu = 200cm^2(Vs)^{-1}$. The phase purity could be demonstrated by means of *in situ* RHEED measurements and *ex situ* X–ray diffraction measurements. Strained c–GaN quantum wells in $Al_xGa_{1-x}N$ barriers, with $0.05 < x < 0.48$, were investigated. RT cathodoluminescence proved the existence of quantized states. Depth–resolved CL showed an intensity maximum which coincided with the MQW region. X–ray reciprocal space maps showed the relaxation of the $Al_xGa_{1-x}N$ barriers. Superlattice peaks of the GaN MQWs could be fitted to $\omega - 2\theta$ scans. TEM images of multi quantum well samples showed atomically sharp interfaces as the reason for high CL intensities. However, over larger scales the QWs are bent; which is probably caused by growth front inhomogeneities from the GaN nucleation. By means of counting the atom layers, the actual QW and barrier thicknesses could be determined. Furthermore, the dislocation density was reduced by the insertion of GaN quantum wells by bending dislocations at the interfaces. The CL emission was fitted using an effective mass model, providing a good agreement with room temperature CL transition energies.

These results give reason to expect that extending future research efforts into the following might be promising:

- Investigation of co–doping Carbon e.g. with Oxygen, in order to increase the RT hole concentration. Possibly the Oxygen might need to be activated using a plasma source.
- Investigation on the dependence of Carbon doping on the growth stoichiometry. This effect has been predicted theoretically, and in MBE growth it is possible to reproducibly vary the surface stoichiometry during growth [62, 156, 157].
- Investigation of increasing the Carbon doping efficiency by means of growing AlN/GaN or $Al_xGa_{1-x}N$/GaN superlattices. This may also improve the contact scheme.
- Investigation of a reduction of the dislocation density through the utilization of AlN or $Al_xGa_{1-x}N$ buffer layers or SLs, respectively.

The orange luminescence observed for medium to high Carbon doping levels may open up the possibility to cover the whole visible spectral range with one material system, based on Gallium Nitride:

- red and yellow by means of artificially inducing deep centers
- yellow and green with $In_xGa_{1-x}N$ compounds, possibly Zn doped
- blue using $In_xGa_{1-x}N$/GaN structures.

Bibliography

[1] H.P. Maruska, D.A. Stevenson, J.I. Pankove, Appl. Phys. Lett. **22** (1972) 303.

[2] S. Nakamura, G. Fasol, *The Blue Laser Diode.* Springer, Berlin Heidelberg 1997.

[3] H. Morkoç, S. Strite, G.B. Gao, M.F. Lin, B. Sverdlov, M. Burns, J. Appl. Phys. **76** (1994) 1363.

[4] S.C. Jain, M. Willander, J. Narayan, R. van Overstraeten, J. Appl. Phys. **87** (2000) 965.

[5] H. Okumura, H. Hamaguchi, K. Ohta, G. Feuillet, K. Balakrishnan, Y. Ishida, S. Chichibu, H. Nakanishi, T. Nagatomo, S. Yoshida, Mater. Sci. Forum **264–268** (1998) 1167.

[6] F. Mireles, S. Ulloa, Phys. Rev. B **58** (1998) 3879.

[7] O. Ambacher, J. Phys. D: Appl. Phys. **31** (1998) 2653.

[8] M. Diagne, Y. He, H. Zhou, E. Makarona, A.V. Nurmikko, J. Han, K.E. Waldrip, J.J. Figiel, T. Takeuchi, M. Krames, Appl. Phys. Lett. **79** (2001) 3720.

[9] E.F. Schubert, W. Grieshaber, I.D. Goepfert, Appl. Phys. Lett. **69** (1996) 3737.

[10] N. el–Masry, J.C.L. Tarn, T.P. Humphreys, N. Hamaguchi, N.H. Karam, S.M. Bedair, Appl. Phys. Lett. **51** (1987) 1608.

[11] H.S. Kim, J.Y. Lin, H.X. Jiang, W.W. Chow, A. Botchkarev, H. Morkoç, Appl. Phys. Lett. **73** (1998) 3426.

[12] F. Bernardini, V. Fiorentini, Phys. Rev. B **57** (1998) R8427.

[13] J.W. Orton, C.T. Foxon, Rep. Prog. Phys. **61** (1998) 1.

[14] B.J. Min, C.T. Chan, K.M. Ho, Phys. Rev. B **45** (1992) 1159.

[15] C.Y. Yeh, Z.W. Lu, S. Froyen, A. Zunger, Phys. Rev. B **46** (1992) 10086.

[16] A. Muñoz, K. Kunc, Phys. Rev. B **44** (1991) 10372.

[17] E.A. Albanesi, W.R.L. Lambrecht, B. Segall, Phys. Rev. B **48** (1993) 17841.

[18] N.E. Christensen, I. Gorczyca, Phys. Rev. B **50** (1994) 4397.

[19] K. Kim, W.R.L. Lambrecht, B. Segall, Phys. Rev. B **53** (1996) 16310.

[20] K. Kim, W.R.L. Lambrecht, B. Segall, Phys. Rev. B **50** (1994) 1502.

[21] A. Rubio, J.L. Corkill, M.L. Cohen, E.L. Shirley, S.G. Louie, Phys. Rev. B **48** (1993) 11810.

[22] K. Shimada, T. Sota, K. Suzuki, J. Appl. Phys. **84** (1998) 4951.

[23] C. Stampfl, C.G. van de Walle, Phys. Rev. B **59** (1999) 5521.

[24] D.N. Talwar, D. Sofranko, C. Mooney, S. Tallo, Mater. Sci. Engin. **B90** (2002) 269.

[25] A. Rubio, J.L. Corkill, M.L. Cohen, Phys. Rev. B **49** (1994) 1952.

[26] D. Vogel, P. Krüger, J. Pollmann, Phys. Rev. B **55** (1997) 12836.

[27] A.F. Wright, J. Appl. Phys. **82** (1997) 2833.

[28] M. Palummo, C.M. Bertoni, L. Reining, F. Finocchi, Physica B **185** (1993) 404.

[29] J.C. Phillips, Rev. Mod. Phys. **42** (1978) 317.

[30] J.C. Phillips, *Bonds and Bands in Semiconductors.* Academic, New York 1973.

[31] J.A. van Vechten, Phys. Rev. **182** (1969) 891.

[32] K. Karch, F. Bechstedt, Phys. Rev. B **56** (1997) 7404.

[33] P.E. van Camp, V.E. van Doren, J.T. Devreese, Solid State Comm. **81** (1992) 23.

[34] I. Gorczyca, N.E. Christensen, Physica B **185** (1993) 410.

[35] A. Muñoz, K. Kunc, Physica B **185** (1993) 422.

[36] L. Hedin, Phys. Rev. **139** (1965) A796.

[37] M.S. Hybertsen, S.G. Louie, Phys. Rev. Lett. **55** (1985) 1418.

[38] M.S. Hybertsen, S.G. Louie, Phys. Rev. B **34** (1986) 5390.

[39] F. Bechstedt, J. Furthmüller, J. Cryst. Growth **246** (2002) 315.

[40] J.A. van Vechten, T.K. Bergstresser, Phys. Rev. B **1** (1970) 3351.

[41] L. Pavesi, M. Guzzi, J. Appl. Phys. **75** (1994) 4779.

[42] P.Y. Yu, M. Cardona, *Fundamentals of Semiconductors.* Springer, Berlin Heidelberg 1996.

[43] C.F. Klingshirn, *Semiconductor Optics.* Springer, Berlin Heidelberg 1995.

[44] R. Haynes, Phys. Rev. Lett. **4** (1960) 361.

[45] C. Merz, M. Kunzer, U. Kaufmann, I. Akasaki, H. Amano, Semicond. Sci. Technol. **11** (1996) 712.

[46] A. Tabata, R. Enderlein, J.R. Leite, S.W. da Silva, J.C. Galzerani, D. Schikora, M. Kloidt, K. Lischka, J. Appl. Phys. **79** (1996) 4137.

[47] U. Schramm, *Photolumineszenz von II–VI Halbleitern und Heterostrukturen.* Diploma thesis, Paderborn University, 1995.

[48] U. Köhler, *Oberflächentopographie und Reflexionseigenschaften von Epitaxieschichten.* Diploma thesis, Paderborn University, 1997.

[49] E. Grimsehl, *Lehrbuch der Physik.* Teubner, Leipzig 1988.

[50] U. Köhler, D.J. As, B. Schöttker, T. Frey, K. Lischka, J. Scheiner, S. Shokhovets, R. Goldhahn, J. Appl. Phys. **85** (1999) 404.

[51] R. Goldhahn, J. Scheiner, S. Shokhovets, T. Frey, U. Köhler, D.J. As, K. Lischka, phys. stat. sol. (b) **216** (1999) 259.

[52] R. Goldhahn, J. Scheiner, S. Shokhovets, T. Frey, U. Köhler, D.J. As, K. Lischka, Appl. Phys. Lett. **76** (2000) 291.

[53] C. Wang, *Cathodoluminescence characterization of large band gap semiconductors.* Ph.D. thesis, Cuvillier, Göttingen 1999.

[54] K. Kanaya, S. Okayama, J. Phys. D **5** (1972) 43.

[55] C. Wang, D.J. As, D. Schikora, K. Lischka, Semicond. Sci. Technol. **14** (1999) 161.

[56] A. Richter, *Photolumineszenz– und Elektrolumineszenzuntersuchungen an c–GaN.* Diploma thesis, Paderborn University, 1999.

[57] L. Vegard, Z. Physik **5** (1921) 17.

[58] E.F. Schubert, *Doping in III–V Semiconductors.* University Press, Cambridge 1993.

[59] J.S. Blakemore, *Semiconductor Statistics.* Dover, New York 1962.

[60] J. Busch, *Herstellung und Charakterisierung von p– und n–dotierten GaN–Epitaxieschichten.* Diploma thesis, Paderborn University, 1999.

[61] B.E. Warren, *X–ray diffraction.* Dover, New York 1968.

[62] B. Schöttker, *Molecular Beam Epitaxy and characterization of doped and undoped cubic GaN layers.* Ph.D. thesis, Shaker, Aachen 1999.

[63] T. Frey, *Cubic III–Nitride Quantum Structures Grown by Molecular Beam Epitaxy.* Ph.D. thesis, Paderborn 2000.

[64] M.A. Herman, H. Sitter, *Molecular Beam Epitaxy: fundamentals and current status.* Springer, Berlin 1989.

[65] P.A. Redhead, J.P. Holson, E.V. Kornelsen, *The Physical Basis of Ultrahigh Vacuum.* Chapman and Hall, London 1968.

[66] A. Roth, *Vacuum Technology.* North–Holland, Amsterdam 1976.

[67] P.K. Larsen, P.J. Dobson (eds.) *Reflection High–Energy Electron Diffraction and Reflection Electron Imaging of Surfaces. NATO ASI Series B: Physics.*, Plenum Press, New York 1988.

[68] W. Braun, *Applied RHEED.* Springer, Berlin Heidelberg 1999.

[69] S. Peters, T. Schmidtling, T. Trepk, U.W. Pohl, J.–T. Zettler, W. Richter, J. Appl. Phys. **88** (2000) 4085.

[70] Y.M. Houng, M.R.T. Tan, B.W. Liang, S.Y. Wang, D.E. Mars, J. Vac. Sci. Technol. **B12** (1994) 1221.

[71] A. Stafford, S.J.C. Irvine, Z. Bougrina, K. Jacobs, I. Moerman, E.J. Thrush, L. Considine, J. Cryst. Growth **221** (2000) 142.

[72] H.P.D. Schenk, P. de Mierry, P. Vennégues, O. Tottereau, M. Laügt, M. Vaille, E. Feltin, E. Beaumont, P. gibert, S. Fernández, F. Calle, Appl. Phys. Lett. **80** (2002) 174.

[73] M.A. Vidal, G. Ramírez-Flores, H. Navarro-Contreras, A. Lastras-Martínez, R.C. Powell, J. E. Greene, Appl. Phys. Lett. **68** (1996) 441.

[74] H. Okumura, H. Hamaguchi, T. Koizumi, K. Balakrishnan, Y. Ishida, M. Arita, S. Chichibu, H. Nakanishi, T. Nagatomo, S. Yoshida, J. Cryst. Growth **189/190** (1998) 390.

[75] B. Daudin G. Feuillet, J. Hübner, Y. Samson, F. Widmann, A. Philippe, C. Bru-Chevallier, G. Guillot, E. Bustarret, G. Bentoumi, A. Deneuville, J. Appl. Phys. **84** (1998) 2295.

[76] D.J. As, T. Frey, D. Schikora, K. Lischka, V. Cimalla, J. Pezoldt, R. Goldhahn, S. Kaiser, W. Gebhardt, Appl. Phys. Lett. **76** (2000) 1686.

[77] H. Yang, A. Trampert, O. Brandt, B. Jenichen, K.H. Ploog, J. Appl. Phys. **83** (1998) 3800.

[78] K.H. Ploog, O. Brandt, H. Yang, B. Yang, A. Trampert, J. Vac. Sci. Technol. **B16** (1998) 2229.

[79] K.–H. Hellwege (ed.), *Landolt–Börnstein. Numerical Data and Functional Relationships in Science and Technology. New Series Group III Vol. 17b*, Springer 1982.

[80] K.–H. Hellwege (ed.), *Landolt–Börnstein. Numerical Data and Functional Relationships in Science and Technology. New Series Group III Vol. 17a*, Springer 1960.

[81] A. Trampert, O. Brandt, H. Yang, K.H. Ploog, Appl. Phys. Lett. **70** (1997) 583.

[82] D. Schikora, M. Hankeln, D.J. As, K. Lischka, T. Litz, A. Waag, T. Buhrow, F. Henneberger, Phys. Rev. B **54** (1996) R8381.

[83] H. Chen, H.F. Liu, Z.Q. Li, S. Liu, Q. Huang, J.M. Zhou, Y.Q. Wang, J. Cryst. Growth **201/202** (1999) 336.

[84] O. Brandt, H. Yang, A. Trampert, M. Wassermeier, K.H. Ploog, Appl. Phys. Lett. **71** (1997) 473.

[85] L. Däweritz, Superlatt. Microstruct. **9** (1991) 141.

[86] M. Nagahara, S. Miyoshi, H. Yaguchi, K. Onabe, Y. Shiraki, R. Ito, Jpn. J. Appl. Phys. **33** (1994) 694.

[87] S. Sanorpim, J. Wu, K. Onabe, Y. Shiraki, J. Cryst. Growth **237–239** (2002) 1124.

[88] S. Fischer, C. Wetzel, E.E. Haller, B.K. Meyer, Appl. Phys. Lett. **73** (1995) 1835.

[89] U. Kaufmann, P. Schlotter, H. Obloh, K. Köhler, M. Maier, Phys. Rev. B **62** (2000) 10867.

[90] D. Schikora, D.J. As, K. Lischka, *The Molecular Beam Epitaxy of Cubic III–Nitrides.* in: *Vacuum Science and Technology.*, Trans World Research 2002.

[91] C.R. Abernathy, J.D. MacKenzie, S.J. Pearton, W.S. Hobson, Appl. Phys. Lett. **66** (1995) 1969.

[92] R. Armitage, Q. Yang, H. Feick, Y. Park, E.R. Weber, MRS Symp. Proc. **719** (2002) F1.2.

[93] S. Shimizu, S. Sonoda, Proc. Int. Workshop Nitride Semicond. IPAP Conf. Ser. I, 740.

[94] H. Tang, J.B. Webb, J.A. Bardwell, S. Raymond, J. Salzman, C. Uzan–Saguy, Appl. Phys. Lett. **78** (2001) 757.

[95] J.B. Webb, H. Tang, S. Rolfe, J.A. Bardwell, Appl. Phys. Lett. **75** (1999) 953.

[96] R. Zhang, T.F. Kuech, Appl. Phys. Lett. **72** (1998) 1611.

[97] U. Birkle, M. Fehrer, V. Kirchner, S. Einfeldt, D. Hommel, S. Strauf, P. Michler, J. Gutowski, MRS Internet J. Nitride Semicond. Res. 4S1, G5.6 (1999).

[98] B. Mensching, C. Liu, B. Rauschenbach, K. Kornitzer, W. Ritter, Mat. Sci. Eng. **B50** (1997) 105.

[99] M. Suzuki, T. Uenoyama, A. Yanase, Phys. Rev. B **52** (1995) 8132.

[100] J.F. Shou, Q.F. Li, C.Y. Yeoh, B.J. Min, M.F. Lin, Prog. Solid State **38** (1996) 94.

[101] P. Bogusławski, E.L. Briggs, J. Bernholc, Appl. Phys. Lett. **69** (1996) 233.

[102] P. Bogusławski, J. Bernholc, Phys. Rev. B **56** (1997) 9496.

[103] A.F. Wright, J. Appl. Phys. **92** (2002) 2575.

[104] P. Bogusławski, E.L. Briggs, J. Bernholc, Phys. Rev. B **51** (1995) 17255.

[105] C. Kittel, *Introduction to Solid State Physics.* 6th ed., Wiley, New York 1986.

[106] J. Bartels *et al.* (eds.), *Landolt–Börnstein. Zahlenwerte und Funktionen aus Naturwissenschaften und Technik. Vol. II/2a*, Springer 1960.

[107] R.J. Malik, R.N. Nottenberg, E.F. Schubert, J.F. Walker, R.W. Ryan, Appl. Phys. Lett. **53** (1988) 2661.

[108] W.E. Hoke, P.J. Lemonias, P.S. Lyman, H.T. Hendriks, D. Weir, J. Cryst. Growth **111** (1991) 269.

[109] H. Ito, T. Ishibashi, Jpn. J. Appl. Phys. **30** (1991) L944.

[110] T.H. Chiu, J.E. Cunningham, J.A. Ditzenberger, W.Y. Jan, J. Cryst. Growth **111** (1991) 274.

[111] H. Ito, O. Nakajima, T. Ishibashi, Appl. Phys. Lett. **62** (1993) 2099.

[112] B.R. Davidson, R.C. Newman, R.E. Pritchard, D.A. Robbie, M.J.L. Sangster, J. Wagner, A. Fischer, K. Ploog, Mat. Sci. Forum **143-147** (1994) 247.

[113] W.Y. Hwang, D.L. Miller, Y.K. Chen, D.A. Humphrey, J. Vac. Sci. Technol. **B12** (1994) 1193.

[114] P.J. Lemonias, W.E. Hoke, D.G. Weir, H.T. Hendriks, J. Vac. Sci. Technol. **B12** (1994) 1190.

[115] H.P. Lee, F.J. Szalkowski, D.L. Sato, X. Liu, E. Ranalli, J. Vac. Sci. Technol. **B12** (1994) 1163.

[116] J.M. van Hove, P.P. Chow, M.F. Rosamond, G.L. Carpenter, J. Vac. Sci. Technol. **B12** (1994) 1200.

[117] D.C. Look, *Electrical Characterization of GaAs Materials and Devices.* Wiley, New York 1988.

[118] B.H. Cheong, K.J. Chang, Phys. Rev. B **49** (1994) 17436.

[119] R. Jones, S. Öberg, Mat. Sci. Forum **143-147** (1994) 253.

[120] J. Wagner, R.C. Newman, B.R. Davidson, S.P. Westwater, T.J. Bullough, T.B. Joyce, C.D. Latham, R. Jones, S. Öberg, Phys. Rev. Lett. **78** (1996) 74.

[121] R.C. Newman, B.R. Davidson, J. Wagner, M.J.L. Sangster, R.S. Leigh, Phys. Rev. B **63** (2001) 205307.

[122] J. Mimila–Arroyo, S.W. Bland, Appl. Phys. Lett. **77** (2000) 1164.

[123] R. Swanepoel, J. Phys. E **16** (1983) 1214.

[124] U. Köhler, M. Lübbers, J. Mimkes, D.J. As, Physica B **308–310** (2001) 126.

[125] O. Brandt, H. Yang, J.R. Müllhäuser, A. Trampert, K.H. Ploog, Mater. Sci. Eng. **B43** (1997) 215.

[126] S.–C.Y. Tsen, D.J. Smith, K.T. Tsen, W. Kim, H. Morkoç, J. Appl. Phys. **82** (1997) 6008.

[127] Z. Liliental-Weber, M. Benamara, W. Swider, J. Washburn, I. Grzegory, S. Porowski, R.D. Dupuis, C.J. Eiting, Physica B **273-274** (1999) 124.

[128] D.J. As, U. Köhler, M. Lübbers, J. Mimkes, K. Lischka, phys. stat. sol. (a) **188** (2001) 699.

[129] D.J. As, U. Köhler, J. phys.: Cond. Matter **13** (2001) 8923.

[130] D.J. As, F. Schmilgus, C. Wang, B. Schöttker, D. Schikora, K. Lischka , Appl. Phys. Lett. **70** (1997) 1311.

[131] G. Ramírez-Flores, H. Navarro-Contreras, A. Lastras-Martínez, R. C. Powell, J. E. Greene, Phys. Rev. B **50** (1994) 8433.

[132] D.J. As, T. Simonsmeier, B. Schöttker, T. Frey, D. Schikora, W. Kriegseis, W. Burkhart, B.K. Meyer, Appl. Phys. Lett. **67** (1995) 1298.

[133] T. Ogino, M. Aoki, Jpn. J. Appl. Phys. **19** (1980) 2395.

[134] E.R. Glaser, T.A. Kennedy, K. Doverspike, L.P. Rowland, D.K. Gaskill, J.A. Freitas, Jr. , M. Asif Khan, D.T. Olson, J.N. Kuznia, D.K. Wickenden, Phys. Rev. B **51** (1995) 13326.

[135] T. Schmidt, K. Lischka, W. Zulehner, Phys. Rev. B **45** (1992) 8989.

[136] A.Y. Polyakov, M. Shin, J.A. Freitas, M. Skowronski, D.W. Greve, R.G. Wilson, J. Appl. Phys. **80** (1996) 6349.

[137] T. Yamamoto, H. Katayama–Yoshida, Jpn. J. Appl. Phys. **36** (1997) L180.

[138] G. Kipshidze, V. Kuryaktov, B. Borisov, Yu. Kudryavtsev, R. Asomoza, S. Nikishin, H. Temkin, Appl. Phys. Rev. **80** (2002) 2910.

[139] A. Nakadaira, H. Tanaka, Appl. Phys. Lett. **70** (1997) 2720.

[140] T. Koizumi, H. Okumura, K. Balakrishnan, H. Harima, T. Inoue, Y. Ishida, T. Nagatomo, S. Nakashima, S. Yoshida, J. Cryst. Growth **201/202** (1999) 341.

[141] M.E. Sherwin, T.J. Drummond, J. Appl. Phys. **69** (1991) 8423.

[142] M.P. Thompson, G.W. Auner, A.R. Drews, J. Electron. Mater. **28** (1999) L17.

[143] T. Suzuki, H. Yaguchi, H. Okumura, Y. Ishida, S. Yoshida, Jpn. J. Appl. Phys. **39** (2000) L497.

[144] M.P. Thompson, G.W. Auner, T.S. Zhelev, K.A. Jones, S.J. Simko, J.N. Hilfiker, J. Appl. Phys. **89** (2001) 3331.

[145] F.C. Frank, J.H. van der Merwe, Proc. Royal Soc. **A189** (1949) 205.

[146] J.W. Matthews, A.E. Blakeslee, J. Cryst. Growth **27** (1974) 118.

[147] S.H. Park, S.L. Chuang, J. Appl. Phys. **87** (2000) 353.

[148] H. Matthieu, P. Lefebvre, P. Christol, Phys. Rev. B **46** (1992) 4092.

[149] T.Y. Chung, K.J. Chang, Semicond. Sci. Technol. **13** (1998) 876.

[150] E.W.S Caetano, V.N. Freire, G.A. Farias, J. Cryst. Growth **246** (2002) 341.

[151] M. Lang, *Epitaxy of Sulfur related Inorganic and Inorganic/Organic Wide–Gap Semiconductor Heterostructures.* Ph.D. thesis, Linz 1994.

[152] O. Brandt, P. Waltereit, K.H. Ploog, J. Phys. D: Appl. Phys. **35** (2002) 577.

[153] U. Köhler, D.J. As, S. Potthast, A. Khartchenko, K. Lischka, O.C. Noriega, E.A. Meneses, A. Tabata, S.C.P. Rodrigues, L.M.R. Scolfaro, G.M. Sipahi, J.R. Leite, phys. stat. sol. (a) **192** (2002) 129.

[154] G. Bauer, W. Richter, *Optical Characterization of Epitaxial Semiconductor Layers.* Springer, Berlin Heidelberg 1996.

[155] T.E. Everhart, P.H. Hoff, J. Appl. Phys. **42** (1971) 5837.

[156] B. Schöttker, J. Kühler, D.J. As, D. Schikora, K. Lischka, Mater. Sci. Forum **264–268** (1998) 1173.

[157] C.H. Seager, A.F. Wright, J. Yu, W. Götz, J. Appl. Phys. **92** (2002) 6553.

Acknowledgements

This work would have been substantially harder without the help, support, contributions and encouragement of many people, none of whom I hope to forget to mention here.

Foremost my fiancée Sandra deserves heartfelt thanks for her patience with me and my frequent preoccupation with physics.

None of this interesting, fascinating but also demanding work, which by no means was limited to physics but entailed engineering as well, would have been possible without Professor K. Lischka and his support (and occasional admonishment). I am indebted to him and Dres. D.J. As and D. Schikora, not the least for sharing their own experiences, knowledge and readiness to engage in sometimes rather longish discussions.

The best Diplom student ever, S. Potthast, definitely deserves special mention. His way of posing challenging questions made things clearer to myself, which was nonplussed only by his readiness in sharing tasks and effort.

In very much the same vein I would like to name my fellow Ph.D. students M. Bartels, O. Husberg, A. Khartchenko, and A. Pawlis, who helped with discussing results, strategies, and were always lending a helping hand whenever needed.
They also contributed to the friendly atmosphere in the group — I will definitely miss the barbecues!

Of course I am also grateful for the (not only technical) help by the optoelectronics staff, I. Zimmermann, S. Igges and B. Volmer.

I would like to acknowledge the benefit of the collaboration and discussions with people of other groups, especially M. Lübbers in Paderborn for the Hall measurements, Prof. Gerthsen's TEM lab in Karlsruhe and Prof. Meyer's SIMS analytical group.

There are many friends scattered around whom I cannot all mention on this page, most notably at the Sondershäuser Verband and Paderborn's catholic student's community. It is good to know that you are there and ready to take my mind off work when necessary.

At last, but certainly not least I would like to thank my and my fiancée's parents for their endless patience, help and support.

"That's the result of all our Study in Scarlet; to get them a testimonial!"
A. Conan Doyle

Appendix A

Listing of samples

This appendix lists all samples grown during the work on this Ph.D. thesis. The columns serve as first guides to the intention of each sample and its basic structure and properties, respectively. Further details, such as cell temperatures or Nitrogen fluxes, as well as comments and spectra and images &c. recorded during growth, can be accessed by consulting the lab log under the appropriate date.

Nomenclature:
Every sample is identified in a unique way by its number. The letter code signifies, beginning left

(constituents)	G	Gallium
	A	Aluminum
	I	Indium
	N	Nitrogen (Nitride)
(dopants)	C	Carbon
	M	Magnesium
	S	Silicon
(experimentalists)	U	Ulrich Köhler
	S	Stefan Potthast

The sample thicknesses were calculated in the way outlined in chapter 2.2.1 on page 9 (and following) from reflection measurements. The growth time is the total time, taking growth interruptions into account.

sample number	date	description	thickness (nm)	growth time
GNU501	30.08.99	auf GNU499 (381 nm)	521 nm	5 h
GNU502	31.08.99	auf GNU499	645 nm	5 h
GNU503	01.09.99		795 nm	8 h
GNU504	02.09.99		835 nm	8 h
GNU507	11.09.99	Si=1050C	412 nmh	5 h
GNU510	29.10.99	auf GNU500 (750 nm)	626 nm	6 h
GNSU511	01.11.99	auf GNU500, Si=950C	834 nm	8 h
GNSU512	02.11.99	auf GNU500, Si=1050C	843 nm	8 h
GNMU513	08.11.99	Mg=200C	495 nm	5 h
GNMU514	12.11.99	Mg=250C	675 nm	7 h
GNMU515	14.11.99	Mg=350C	614 nm	7 h
GNPNU516	18.11.99	pn-Struktur, Si=1075C, Mg=350C	1434 nm	15.5 h
GNPINU517	22.11.99	pn-Struktur mit GaInN, sonst wie 516	1435 nm	15.5 h
GNU532	22.02.00	2 zus. Keimbildungen nach je 2h, undotiert	681 nm	8 h
GNU533	23.02.00		2108 nm	24 h
GNCU534	29.02.00	C=144W	715 nm	8 h
GNCU535	01.03.00	C=200W	728 nm	8 h
GNCU536	02.03.00	C=300W	488 nm	6 h
GNU537	06.03.00	4 zus. Keimbildungen nach je 1h, undotiert	815 nm	9 h
GNU538	07.03.00	2 zus. Keimbildungen nach je 1h, undotiert		6 h
GNU539	08.03.00	4 zus. Keimbildungen nach je 2h, undotiert	1147 nm	13 h
GNU540	11.04.00		437 nm	5 h
GNU541	12.04.00	und., Rechtecke (Mikr.), AFM Schraubenvers.	414 nm	5 h
GNU542	14.04.00	4 zus. Keimbildungen nach je 1h, undotiert	550 nm	4+3 h
GNMU543	18.04.00	Mg=400C, growth interruptions, 3-5s stoich.	382 nm	5 h
GNMU544	19.04.00	Mg=450C, 0s stoichiometry	452 nm	5 h
GNU545	10.05.00	undotiert	475 nm	5 h
GNU546	11.05.00	"undotiert, 3"" Wafer"	490 nm	7 h
GNU547	16.05.00	auf GNU542, undotiert, höhere growth rate	1721 nm	6 h
GNCU548	17.05.00	auf GNU542 (500nm), C=70W	1030 nm	6 h
GNCU549	18.05.00	auf GNU542, C=80W	934 nm	6 h
GNCU550	19.05.00	auf GNU542, C=90W	1035 nm	6 h
GNCU551	24.05.00	auf GNU542, C=60W	1080 nm	6 h
GaAsU552	25.05.00	undotiert	1000 nm	3,5 h
GaAsU553	25.05.00	C=70W	1000 nm	3,5 h
GaAsU554	26.05.00	C=90W	1000 nm	3,5 h
GaAsU555	30.05.00	C=150W	1000 nm	3,5 h
GNU556	31.05.00	undotiert, 1h@R=90nm/h, 5h höhere Rate	974 nm	6 h
GNSU557	02.06.00	Si=1075C, 1h@R=90nm/h, 5h höhere Rate	1025 nm	6 h
GIN558	07.06.00	auf GNU546(490nm), 1h GaN+1.45h InGaN		2 h
GIN559	08.06.00	auf GNU546, In=600C InGaN DHS 1h		
GIN560	08.06.00	auf GNU546, In=620C InGaN DHS 1h		
GNSU561	15.06.00	"2""Wafer n-typ, Si=1100C(interrupt), 1h+8h"	1465 nm	9 h
GNU562	20.06.00	auf GNU546(350nm), 1h@90nm/h +5h	1890 nm	6 h
GNU563	21.06.00	1h@90nm/h, 5:15h@höherer Rate	1635 nm	6,25 h
GINU564	26.06.00	Repro GINT436, In=620C InGaN DHS 1h		2,5 h
GaAsU565	27.06.00	C=250W	1000 nm	3,3 h
GaAsU566	27.06.00	C=400W	1000 nm	3,3 h

Table A.1: Sample listing no. 1.

sample number	date	description	thickness (nm)	growth time
GIN567	28.06.00	Repro GINT438, In=590C InGaN DHS 1h	356 nm	
GaAsU568	30.06.00	C=300W	1000 nm	3,25 h
GNCU569	03.07.00	C=350W	677 nm	7 h
GaAsU570	04.07.00	C=350W	1000 nm	3.13 h
GaAsU571	04.07.00	C=400W	1000 nm	3.13 h
GNCU572	05.07.00	C=400W	647 nm	7 h
GNU573	06.07.00	undotiert	659 nm	7 h
GNCU574	07.07.00	auf GNSU561a (1450nm), C=300W	2075 nm	7 h
GNCU575	09.07.00	C=300W	666 nm	7 h
GINCU576	10.07.00	C ca. 300W, In=620C, 2.5h InGaN	250 nm	4.5 h
GNU577	12.07.00	undotiert	659 nm	7 h
GIN578	24.07.00	(GNU546)2h InGaN In=620C Ga=770C TSreal=605C		2.5 h
GIN579	24.07.00	(GNU546)2h InGaN In=620C Ga=770C TSreal=595C		2.5 h
GIN580	25.07.00	(GNU546)2h InGaN In=620C Ga=770C TSreal=590C		2.5 h
GIN581	25.07.00	(GNU546)2h InGaN In=620C Ga=770C TSreal=585C		2.5 h
GIN582	26.07.00	(GNU546)2h InGaN In=620C Ga=770C TSreal=575C		2.5 h
GNU583	26.07.00	undotiert, 1h@90nm/h, 3h@180nm/h	711 nm	4 h
GNCU584	31.07.00	C=100W	1140 nm	12 h
GNCU585	01.08.00	C=150W	1121 nm	12 h
GNU586	09.08.00	undotiert (nach Kammeröffnung)	875 nm	12 h
GNCU587	10.08.00	C=50W	682 nm	12 h
GNCU588	11.08.00	C=150W, höhere Wachstumsrate!	1044 nm	7 h
GNCU589	14.08.00	C=200W, stöchiometrisch	920 nm	12 h
GNCU590	15.08.00	C=150W, Ga-reich (t¿5s)	914 nm	12 h
GNCU591	16.08.00	C=200W, höhere Wachstumsrate!	1123 nm	7 h
GNCU592	17.08.00	C=200W, Ga-reich	898 nm	12 h
GNU593	12.09.00	nach GNU538, ohne KB, Si=950C in 5h top layer	702 nm	7 h
GNU594	13.09.00	nach GNU537, ohne KB, Si=950C in 5h top layer	869 nm	9 h
GNU595	14.09.00	nach GNU532, ohne KB, Si=950C in 5h top layer	845 nm	9 h
GNU596	15.09.00	repro GNU593, undotiert	620 nm	7 h
GNU597	18.09.00	repro GNU537, Si=950C in top layer	840 nm	9 h
GNU598	19.09.00	repro GNU538, Si=950C in top layer	640 nm	7 h
GNU599	20.09.00	repro GNU532, Si=950C in top layer	819 nm	9 h
GNU600	21.09.00	repro GNU538	632 nm	7 h
GNU601	22.09.00	undotiert	447 nm	5 h
GNU602	25.09.00	undotiert, nach WE-Ausheizen Rezipient	460 nm	5 h
GNU603	26.09.00	undotiert	631 nm	5 h
GNU604	27.09.00	undotiert	458 nm	5 h
GNU605	28.09.00	undotiert	440 nm	5 h
GNU606	29.09.00	undotiert	457 nm	5 h
GNU607	04.10.00	undotiert, Ga-reich (tdes7s)	423 nm	5 h
GNSU608	05.10.00	Si=950C	420 nm	5 h
GNU609	09.10.00	”3”” Wafer undotiert, 1h+6h@180nm/h”	953 nm	7 h
GNCU610	10.10.00	C=50W	1047 nm	12 h
GNCU611	12.10.00	C=100W	1028 nm	12 h
GNU612	16.10.00	undotiert, nach belüfteter Kammer, 5h höhere Rgrowth	963 nm	6 h
GNU613	17.10.00	undotiert	433 nm	5 h
GNCU614	18.10.00	C=100W	1066 nm	12 h
GNCU615	20.10.00	C=150W	991 nm	12 h
GNCU616	22.10.00	C=200W	1044 nm	12 h

Table A.2: Sample listing no. 2.

sample number	date	description	thickness (nm)	growth time
GNCU617	23.10.00	C=250W	1050 nm	12 h
GNCU618	24.10.00	C=150W	1035 nm	12 h
GNCU619	26.10.00	C=300W	1023 nm	12 h
GNU620		undotiert; teils nach Kammeröffnung, 3h höhere Rgrowth	1200 nm	
GNU621	08.11.00	undotiert	525 nm	6 h
GNCU622	09.11.00	C=150W	1020 nm	12 h
GaAsU623	10.11.00	C=150W	1000 nm	3 h
GNCU624	13.11.00	C=400W	843 nm	12 h
GANU625	24.11.00	"1h GaN+3h AlGaN; Al=970C, TS=720C, stöchiom."	296 nm	4 h
GANU626	27.11.00	auf GNU546/1,0.3h+5h AlGaN,Al=980C,TS=720C	668 nm	5 h
GANU627	29.11.00	auf GNU542/1, Al=1010C, Ga=830C, TS=720C	870 nm	5 h
GANU628	06.12.00	1.5hGaN+7h, Al=975C, Ga=840C, TS=720C, stöch	612 nm	7 h
GANU629	07.12.00	auf GNU546/3, Al=1000C, Ga=830C, TS=720C	890 nm	7 h
GANU630	08.12.00	auf GNU542/2,5h AlN stöch., Al=1035C, TS=720C		5 h
GNU631	12.12.00	"2"" Wafer, undotiert"	325 nm	4 h
GANU632	12.12.00	auf GNU546/4,Al=1020C,Ga=865C,TS=750C	731 nm	7 h
GANU633	13.12.00	auf GNU542/3, Al=1090C,Ga=920C,TS=800C		7 h
GANU634	14.12.00	auf GNU631/3, AlN Al=1130C, TS=800C		7 h
GANU635	15.12.00	GNU631/4, 5xMQW 2.5nmGaN/5nmAlGaN, x=0.24	1099 nm	6.5 h
GANU636	18.12.00	GNU631/4, 5xMQW 5nmGaN/5nmAlGaN, x=0.22	799 nm	6.5 h
GANU637	19.12.00	GNU631/4, 5xMQW 5nmGaN/10nmAlGaN, x=0.25	860 nm	6.5 h
ANU638	09.01.01	AlN-Keimbildg. +-wachstum auf GaAs ohne GaN-Buffer	205 nm	4 h
GANU639	10.01.01	GNU631/7+1h GaN, Schicht abgeblttert		4 h
GANU640	16.01.01	6h GaN+KB auf GaAs	849 nm	7 h
GANU641	18.01.01	6h GaN+KB auf GaAs	934 nm	7 h
GANU642	22.01.01	6h GaN+KB auf GaAs	1156 nm	12 h
GANU643	23.01.01	6h GaN+KB auf GaAs	639 nm	4 h
GNU644	24.01.01	6h GaN+KB auf GaAs, Unterlage GANU640-43	461 nm	6 h
GNU645	25.01.01	"2"" Wafer"		3 h
GANU646	01.02.01	GaN-KB +15min Wachstum	236 nm	4 h
GANU647	12.02.01	auf GNU645/1, Al=910C, Ga=880C, TS=754C	783 nm	7 h
GNU648	13.02.01	"2"" Wafer"		1 h
GANU649	14.02.01	auf GNU648/1, 5xMQW 2.5nmGaN/5nmAlGaN	641 nm	6.5 h
GANU650	15.02.01	auf GNU648/2, 20xMQW 2.5nmGaN/5nmAlGaN	767 nm	8 h
GANU651	16.02.01	auf GNU648/3, 5xMQW 5nmGaN/5nmAlGaN	638 nm	6.5 h
GANU652	19.02.01	auf GNU648/4, 5xMQW 5nmGaN/10nmAlGaN	670 nm	7 h
GANU653	20.02.01	auf GNU648/5, 20xMQW 5nmGaN/10nmAlGaN	891 nm	10 h
GANU654	21.02.02	auf GNU648/6, SQW 7.5nm GaN	414 nm	4 h
GANU655	22.02.01	auf GNU648/7, 5xSQW 7.5nm/5nm/2.5nm GaN	653 nm	9 h
GANU656	23.02.01	auf GNU648/8, SL 5xQW 2.5nmGaN/1nmAlGaN	518 nm	7 h
GANU657	27.02.01	auf GNU648/9, 3 SQW 7.5nm/5nm/2.5nm GaN	678 nm	9 h
GNU658	05.03.01	auf GNU648/10, undotiert	661 nm	7 h
GANU659	06.03.01	auf GNU648/11, repro 657 mit 30nm barriere	560 nm	7 h
GNU660	07.03.01	auf GNU648/12, TSi=950C, TAl=960C, 5x5nm Buff	584 nm	7 h
GNU661	08.03.01	auf GNU648/13, repro 660 10nm Buffer spacer, AlGaN	606 nm	7 h
GNU662	09.03.01	auf GNU648/14, repro 661 mit AlN-Buffer	584 nm	7 h
GNU663	12.03.01	auf GNU648/15, repro 660 mit AlN buffer	603 nm	7 h
GNU664	13.03.01	auf GNU648/16, repro 660 25nm Buffer spacer, AlGaN		7 h
GNU665	14.03.01	auf GNU648/17, repro 660 5nm Buffer spacer, AlGaN		7 h
GaAsU666	09.04.01	nominell undotiert	1000 nm	3 h

Table A.3: Sample listing no. 3.

sample number	date	description	thickness (nm)	growth time
GaAsU667	10.04.01	C=50W	1000 nm	3 h
GaAsU668	10.04.01	C=100W	1000 nm	3 h
GNU704	23.07.01	neue Apertur, 130W/2.0%	763 nm	6 h
GNU705	24.07.01	auf GNU631/9 (330nm), 3h*125nm/h + 5h*147nm/h	1438 nm	8 h
KB706	25.07.01	ca. 6h GaAs growth, Stop @ Keimbildung (N2-Plasma)		
KB707	26.07.01	KB:3', Ga=820C, TS=600C, N2=130W/2W/2.0%		
KB708	26.07.01	KB:3', Ga=825C, TS=600C, N2=130W/2W/2.0%		
KB709	27.07.01	KB:4', Ga=825C, TS=600C, N2=130W/1W/2.0%		
KB710	27.07.01	KB:2', Ga=825C, TS=600C, N2=130W/1W/2.0%		
GNUS711	31.07.01	KB wie 710, Rampe 35K/' auf TS=720C	645 nm	5 h
GNUS712	01.08.01	KB wie 710, Rampe 40K/' auf TS=720C		4 h
GNUS713	13.08.01	KB: wie708, Rampe 40K/' auf TS=720C		5 h
GNUS714	14.08.01	KB: wie709, Rampe 40K/' auf TS=720C	577 nm	5 h
GNUS715	15.08.01	KB: wie709, t=5', Rampe 40K/' auf TS=720C	593 nm	5 h
GNUS716	16.08.01	KB: wie709, t=6', Rampe 40K/' auf TS=720C	568 nm	5 h
GNUS717	10.09.01	repro GNUS714	620 nm	5 h
GNUS718	11.09.01	KB:4', Ga=820C, TS=600C, Rampe 40K/' TS=720C	589 nm	5 h
GNUS719	12.09.01	KB:4', Ga=830C, TS=600C, Rampe 40K/' TS=720C	495 nm	5 h
GNUS720	13.09.01	KB:4', Ga=810C, TS=600C, Rampe 40K/' TS=720C	595 nm	5 h
GaAs721	17.09.01	Flußkalibrierung Ga-Quelle		
GNUS722	18.09.01	auf GaAs721, KB: wie 714, Rampe 10K/' auf TS=720C	620 nm	5 h
GNUS723	19.09.01	KB: wie722, Rampe 40K/' TS=720C+5' Latenz	603 nm	5 h
GNUS724	20.09.01	KB: wie714, Rampe 70K/' TS=720C+1' Latenz	625 nm	5 h
GNUS725	21.09.01	KB: wie714, Rampe 40K/' TS=720C+0' Latenz	594 nm	5 h
GNUS726	24.09.01	KB: wie 714, Rampe 40K/' TS=720C shutter offen	620 nm	5 h
GNUS727	25.09.01	KB: wie 714, Rampe 10K/' TS=720C shutter offen	630 nm	5 h
GNUS728	26.09.01	KB: TS=580C, TGa=825C, t=4', Rampe 717	580 nm	5 h
GNUS729	27.09.01	KB: TS=550C, TGa=825C, t=4', Rampe 717	589 nm	5 h
GNUS730	28.09.01	repro 717	608 nm	5 h
GNS731	01.10.01	repro 726, mit Ga-Rampe und As offen	614 nm	5 h
GNUS732	02.10.01	repro 722 mit t=3' KB	522 nm	5 h
GNUS733	04.10.01	repro 722 mit t=5' KB	620 nm	5 h
GNUS734	05.10.01	repro 718 mit Rampe 10K/'	638 nm	5 h
GNUS735	08.10.01	repro 719 mit Rampe 10K/'	594 nm	5 h
GNUS736	09.10.01	repro 732	556 nm	5 h
GNUS737	10.10.01	repro 734	550 nm	5 h
GNUS738	11.10.01	andere KB!!	616 nm	5 h
GNUS739	12.10.01	t=3h+2h, GaN-beschichtete Rückseite	605 nm	5 h
GNUS740	16.10.01	repro 731 ohne As	634 nm	5 h
GNUS741	17.10.01	repro 727 mit As	585 nm	5 h
GNUS742	18.10.01	repro 741	615 nm	5 h
GNU743	19.10.01	auf p-GaAs Substrat		8 h
GNUS744	22.10.01			2 h
GNUSS745	23.10.01	auf GNUS731	1745 nm	10 h
GNUSS746	24.10.01	auf GNUS733	1755 nm	10 h
GNUSS747	29.10.01	auf GNUS740	1723 nm	10 h
GNUSS748	30.10.01	auf GNUSS745	4552 nm	28 h
GNUSS749	05.11.01	auf GNUSS746	4677 nm	28 h
GNUS750	07.11.01	auf p-GaAs	812 nm	7 h
GaAsUS751	08.11.01	C=90W		

Table A.4: Sample listing no. 4.

sample number	date	description	thickness (nm)	growth time
GaAsUS752	08.11.01	C=120W		
GaAsUS753	08.11.01	C=150W		
GaAs754	09.11.01	C=270W		
GaAs755	12.11.01	undotiert		
GNSUS756	12.11.01	TSi=1000C	573 nm	7 h
GNCUS757	13.11.01	C=120W	1035 nm	9 h
GNSUS758	14.11.01	TSi=1000C	1065 nm	9 h
GNCUS759	15.11.01	C=90W		9 h
GNCUS760	16.11.01	C=300W		1 h
GNSU761	18.11.01	TSi=1025C	555 nm	5 h
GNSU762	20.11.01	TSi=1020C, auf p-GaAs (27446/211)	791 nm	7 h
GaAsS763		C=90W		
GaAsS764		C=180W		
SNUS765	03.12.01	TSi=1100C, N2 120W/1W/2.0%, TS=600C	350 nm	2 h
GaAs766	04.12.01	C=0W		
GaAs767	04.12.01	C=0W		
GaAs768	04.12.01	C=270W		
PNUS769	05.12.01	auf GNSU561d, p undotiert	1970 nm	5 h
GNUS770	06.12.01		557 nm	5 h
PNUS775	14.12.01	auf GNSU561g, 10' InGaN , p undotier		7 h
GNUS782	09.01.02	auf GNU648	536 nm	4 h
GNUS783	09.01.02		573 nm	5 h
GNUS784	10.01.02		547 nm	
GNUS785	11.01.02			

Table A.5: Sample listing no. 5.